



NAVAL POSTGRADUATE SCHOOL

MONTEREY, CALIFORNIA

DISSERTATION

**OPTIMAL CONTROL OF SHOCK WAVE ATTENUATION
IN SINGLE- AND TWO-PHASE FLOW WITH
APPLICATION TO IGNITION OVERPRESSURE IN
LAUNCH VEHICLES**

by

Nathan D. Moshman

December 2011

Dissertation Supervisor: Sivaguru S. Sritharan
Committee Chair/Co-Supervisor: Garth V. Hobson

Approved for public release; distribution is unlimited

THIS PAGE INTENTIONALLY LEFT BLANK

REPORT DOCUMENTATION PAGE

Form Approved
OMB No. 0704-0188

The public reporting burden for this collection of information is estimated to average 1 hour per response, including the time for reviewing instructions, searching existing data sources, gathering and maintaining the data needed, and completing and reviewing the collection of information. Send comments regarding this burden estimate or any other aspect of this collection of information, including suggestions for reducing this burden to Department of Defense, Washington Headquarters Services, Directorate for Information Operations and Reports (0704-0188), 1215 Jefferson Davis Highway, Suite 1204, Arlington, VA 22202-4302. Respondents should be aware that notwithstanding any other provision of law, no person shall be subject to any penalty for failing to comply with a collection of information if it does not display a currently valid OMB control number. **PLEASE DO NOT RETURN YOUR FORM TO THE ABOVE ADDRESS.**

1. REPORT DATE (DD-MM-YYYY) 16-12-2011			2. REPORT TYPE PhD Dissertation		3. DATES COVERED (From — To) Jan 2009–Dec 2011	
4. TITLE AND SUBTITLE Optimal Control of Shock Wave Attenuation in Single- and Two-Phase Flow with Application to Ignition Overpressure in Launch Vehicles					5a. CONTRACT NUMBER	
					5b. GRANT NUMBER	
					5c. PROGRAM ELEMENT NUMBER	
6. AUTHOR(S) Nathan D. Moshman					5d. PROJECT NUMBER	
					5e. TASK NUMBER	
					5f. WORK UNIT NUMBER	
7. PERFORMING ORGANIZATION NAME(S) AND ADDRESS(ES) Naval Postgraduate School Monterey, CA 93943					8. PERFORMING ORGANIZATION REPORT NUMBER	
9. SPONSORING / MONITORING AGENCY NAME(S) AND ADDRESS(ES) Department of the Navy					10. SPONSOR/MONITOR'S ACRONYM(S)	
					11. SPONSOR/MONITOR'S REPORT NUMBER(S)	
12. DISTRIBUTION / AVAILABILITY STATEMENT Approved for public release; distribution is unlimited						
13. SUPPLEMENTARY NOTES The views expressed in this thesis are those of the author and do not reflect the official policy or position of the Department of Defense or the U.S. Government. IRB Protocol Number: N/A						
14. ABSTRACT NASA and private launch providers have a need to understand and control ignition overpressure blast waves that are generated by a solid grain rocket during ignition. Research in accurate computational fluid dynamics prediction of the launch environment is underway. A clearer picture is emerging from empirical data which more precisely categorizes all the dissipative mechanisms present in droplet-shock interactions. In this dissertation, water droplets and their effects due to vaporization are represented as a control action and two new optimal control problems are formulated concerning unsteady shock wave attenuation. A single-phase control problem is formulated by representing the effect of droplet vaporization as an energy sink on the right hand side of the unsteady Euler Equations in one dimension. Results for the optimal distribution of equivalent mass of water vaporized for a given level of attenuation are presented. A two-phase control problem consists of solving for the initial optimal water droplet distribution. Results are presented for constrained and unconstrained water volume fraction distributions over increasing levels of attenuation. New adjoint-based algorithms were constructed which leave the final time free and satisfy all first order necessary conditions as well as avoid taking a variation at the shock front.						
15. SUBJECT TERMS						
16. SECURITY CLASSIFICATION OF:			17. LIMITATION OF ABSTRACT UU	18. NUMBER OF PAGES 143	19a. NAME OF RESPONSIBLE PERSON	
a. REPORT Unclassified	b. ABSTRACT Unclassified	c. THIS PAGE Unclassified			19b. TELEPHONE NUMBER (include area code)	

THIS PAGE INTENTIONALLY LEFT BLANK

Approved for public release; distribution is unlimited

**OPTIMAL CONTROL OF SHOCK WAVE ATTENUATION IN SINGLE- AND
TWO-PHASE FLOW WITH APPLICATION TO IGNITION OVERPRESSURE IN
LAUNCH VEHICLES**

Nathan D. Moshman

GS-9 Step 3

B.S., University of California, Santa Barbara, 2006

M.S., University of California, San Diego, 2008

Submitted in partial fulfillment of the
requirements for the degree of

DOCTOR OF PHILOSOPHY IN AEROSPACE ENGINEERING

from the

NAVAL POSTGRADUATE SCHOOL

December, 2011

Author:

Nathan D. Moshman

Approved by:

Dr. Sivaguru S. Sritharan
Dissertation Supervisor

Dr. Garth V. Hobson
Committee Chair/Co-Supervisor

Dr. Christopher M. Brophy
Committee Member

Dr. Francis X. Giraldo
Committee Member

Dr. Wei Kang
Committee Member

Dr. Bruce T. Vu
Committee Member

Approved by:

Dr. Knox T. Millsaps
Chair, Department of Mechanical and Aerospace Engineering

Approved by:

Dr. Leonard A. Ferrari
Provost

THIS PAGE INTENTIONALLY LEFT BLANK

ABSTRACT

NASA and private launch providers have a need to understand and control ignition overpressure blast waves that are generated by a solid grain rocket during ignition. Research in accurate computational fluid dynamics prediction of the launch environment is underway. A clearer picture is emerging from empirical data which more precisely categorizes all the dissipative mechanisms present in droplet-shock interactions. In this dissertation, water droplets and their effects due to vaporization are represented as a control action and two new optimal control problems are formulated concerning unsteady shock wave attenuation. A single-phase control problem is formulated by representing the effect of droplet vaporization as an energy sink on the right hand side of the unsteady Euler Equations in one dimension. Results for the optimal distribution of equivalent mass of water vaporized for a given level of attenuation are presented. A two-phase control problem consists of solving for the initial optimal water droplet distribution. Results are presented for constrained and unconstrained water volume fraction distributions over increasing levels of attenuation. New adjoint-based algorithms were constructed which leave the final time free and satisfy all first order necessary conditions as well as avoid taking a variation at the shock front.

THIS PAGE INTENTIONALLY LEFT BLANK

Table of Contents

1	Introduction	1
1.1	Ignition Overpressure	1
1.2	Experimental Results on Droplet-Shock Interactions	1
1.3	Recent Research on IOP Attenuation	2
1.4	New Contributions of Current Work	4
2	Mathematical Theory	7
2.1	Euler System in One Dimension	7
2.2	Two-Phase Flow Model.	16
2.3	Optimal Control of Systems of Partial Differential Equations	23
3	Numerical Methods	43
3.1	Computational Fluid Dynamics for Unsteady Compressible Flow	43
3.2	Method of Solution for Two-Phase, Gas-Liquid Coupling	51
3.3	Solution Procedure for Optimal Control System	56
4	Results and Discussion	69
4.1	IOP Simulations in 2D using FASTRAN	69
4.2	Single-Phase Control Calculation Results.	73
4.3	Two-Phase Calculation Results	80
4.4	Serial and Parallel Code Run-Time Optimization.	93
5	Conclusions	95
	List of References	97
	Appendices	105
A	Calculation of the elements of $\frac{\partial A_{ij}}{\partial U_k} \frac{\partial U_k}{\partial x}$ for the two-phase adjoint system	107
B	Calculation of the elements of $\frac{\partial S_i}{\partial U_j}$ for the two-phase adjoint system	111

C Time Derivatives and Discretization of Transversality Condition for Single- and Two-Phase Control Formulation	119
Initial Distribution List	123

List of Figures

Figure 1.1	Experimental data on IOP attenuation, Jourdan et al. [12]	3
Figure 1.2	Physical diagram of simulated interaction.	5
Figure 2.1	Instantaneous wave patterns of a Left and Right state and shock wave which obey the entropy condition of the Euler system in 1D	12
Figure 2.2	Solution regions of the shock tube problem and wave pattern at the initial instant the diaphragm bursts	14
Figure 3.1	Comparison of numerical solutions to the Riemann problem .4 ms after diaphragm burst in shock tube flow. The initial pressure ratio was 10:1 in each case with a discontinuity at $x = .5m$	45
Figure 3.2	Intermediate non-uniform grid, Kurgarov and Tadmor [67]	48
Figure 3.3	Block diagram of solution procedure for single-phase control calculation	64
Figure 3.4	Block diagram of solution procedure for two-phase control calculation	67
Figure 4.1	Simulated Shuttle IOP: Mach number at 1.2 ms	69
Figure 4.2	Simulated Shuttle IOP: Mach number at 4 ms	69
Figure 4.3	Simulated Shuttle IOP: Mach number at 10 ms	69
Figure 4.4	Simulated Shuttle IOP: pressure at 1.2 ms	70
Figure 4.5	Simulated Shuttle IOP: pressure at 4 ms	70
Figure 4.6	Simulated Shuttle IOP: pressure at 10 ms	70
Figure 4.7	Flow conditions over time for Monitor Point 1	71
Figure 4.8	Flow conditions over time for Monitor Point 2	72
Figure 4.9	Monitor Point 2, Pressure profile at final time, no control used.	73
Figure 4.10	Monitor Point 2, Optimal pressure profile at final time, target state $Q(x) \sim 85\% OP_0$	74

Figure 4.11	Monitor Point 2, Optimal distributed control, $Q(x) \sim 85\% OP_0$	74
Figure 4.12	Monitor Point 2, Optimal pressure at final time, $Q(x) \sim 70\% OP_0$. .	75
Figure 4.13	Monitor Point 2, Optimal distributed control, $Q(x) \sim 70\% OP_0$. . .	75
Figure 4.14	Monitor Point 2, Optimal pressure at final time, $Q(x) \sim 50\% OP_0$. .	76
Figure 4.15	Monitor Point 2, Optimal distributed control, $Q(x) \sim 50\% OP_0$. . .	76
Figure 4.16	Monitor Point 2, Cost functional (top) and final time (bottom) vs. iteration, $Q(x) \sim 50\% OP_0$	77
Figure 4.17	Monitor Point 2, $m_{H_2Ovape}(x)$, Energy equivalent distribution of water mass vaporized	78
Figure 4.18	Monitor Point 1, $m_{H_2Ovape}(x)$, Energy equivalent distribution of water mass vaporized	79
Figure 4.19	Optimal water volume fraction distributions $\alpha_l^*(x, 0)$, unconstrained at initial moment in time	81
Figure 4.20	Optimal final time pressure profiles resulting from initial data in Figure 4.19	82
Figure 4.21	Cost functional J in red and initial penalty I over iterations of solution procedure in Figure 3.4	83
Figure 4.22	Final time, in seconds, vs iteration number for the unconstrained case. The regions of greatest slope are after iterations where the target state has been changed. The slope tending toward zero means that the solution is converging.	84
Figure 4.23	Optimal initial water volume fraction distributions, $\alpha_l(x, 0) \leq .7$. . .	85
Figure 4.24	The optimal pressure profiles at the final time resulting from the control initial data in Figure 4.23	86
Figure 4.25	Optimal initial water volume fraction distributions, $\alpha_l(x, 0) \leq .5$. . .	87
Figure 4.26	Optimal final time pressure profiles resulting from initial data in Figure 4.25	88
Figure 4.27	Effect of variable droplet size	90
Figure 4.28	Effect of variable water vapor density due to gas pressure	91

Figure 4.29	Effect of maximum of Gaussian water volume fraction distribution on IOP strength after 1 ms.	92
Figure 4.30	Time duration for solving the 3-component adjoint system of the Euler equations over the time interval $[T^*, 0]$	93
Figure 4.31	Time duration for solving 7-component adjoint system of two-phase model over the time interval $[T^*, 0]$	94

THIS PAGE INTENTIONALLY LEFT BLANK

Nomenclature

<i>Symbol</i>	<i>Description</i>
α	Volume fraction of gas or liquid phase $\in (0, 1)$
A	Jacobian matrix
a, b	Weighting constants, wave speed
β	Empirical vaporization constant
c	Speed of sound
C_d	Drag coefficient
D_p	Droplet diameter
$D_{M \times M}$	Tridiagonal block finite difference matrix
ϵ	positive small constant
f	Functional of final time, function used in exact solution to the Riemann problem
F	Conservative flux vector
F_d	Drag force
γ	Ratio of specific heats
γ_l, π_l	Liquid constants in equation of state
Γ	Constant term in Riemann invariants
H	Hamiltonian, conservative source vector
J	Cost functional
I	Initial time penalty
\tilde{J}	Augmented cost functional
K	Final time penalty
L	Running cost functional (Lagrangian)
L_{hv}	Latent heat of vaporization of water at $100^\circ C$
λ	Characteristic speeds, heat transfer constant
Λ	Diagonal matrix of eigenvalues of Jacobian
M	Number of spatial grid points
MH	Source vector for mass and heat exchange
m_{H_2Ovape}	Energy equivalent vaporized water mass
\dot{m}	Rate of change of mass changing phase
μ	Dynamic compaction coefficient
N	Non-linear partial differential operator
N	Number of time steps
N_p	Number of droplets per cell
Nu	Nusselts number
OP_0	Absolute pressure just behind shock front of uncontrolled IOP blast wave
Ω	Total simulated spatial domain in 1D
Ω_s	Spatial domain behind shock where simulated pressure is above target level
$\partial\Omega$	Spatial domain boundary

P	Pressure
PR	Source vector for pressure relaxation
Pr	Prandtl number
Q	Target pressure at final time
Q_i	Rate of heat exchange between phases
R	Specific gas constant for air
$R(U)$	Right hand side matrix in adjoint calculation
Re	Reynolds number
ρ	Density
ρ_{H2Ov}	Density of water vapor at the saturation pressure of the surrounding gas
ρe	Internal energy
ρE	Total energy
ρu	Momentum
s	Entropy
S	Total non-conservative source vector
S_p	Total surface area of droplets
Δt	Size of time discretization
t	Time, independent variable
T, t^N	Final time, continuous and discrete
T	Temperature
u	Velocity
U	Conservative state vector
\tilde{U}	Primitive state vector
\hat{U}	Characteristic state vector
V	Adjoint vector
VR	Source Vector for velocity relaxation
x, x_j	1D spatial vector in Ω , continuous and discrete element
w	State vector on intermediate, non-uniform grid in second order Godunov method extension
Δx	Size of spatial discretization
z	Distributed control variable in single-phase control calculation
<i>Subscript</i>	
i	Spatial index, interface quantity
i, j, k	Variable number for state or adjoint vector
g	Gas
l	Liquid
R, L	Right, left state to a discontinuity
p	Particle (Droplet) of Water
<i>Superscript</i>	
l	Iteration of overall optimal control algorithm
n	Temporal index
$*$	Optimal quantity, exact solution to Riemann problem in star region
PR	Solution to ODE for pressure relaxation in two-phase model

VR	Solution to ODE for velocity relaxation in two-phase model
MH	Solution to ODE for mass and heat exchange in two-phase model
0	Initial guess, iterate or initial condition
$+, -$	Right, left state relative to a discontinuity

THIS PAGE INTENTIONALLY LEFT BLANK

Acknowledgements

I would like to thank the Naval Postgraduate School and Dr. S. Sritharan for allowing me the opportunity to earn my doctorate in aerospace engineering. I would like to thank each of my committee members for sharing their unique expertise and guidance throughout the dissertation process. A special thanks to my committee chair Dr. G. Hobson for his constant support and advice. Lastly, I'd like to thank my family for raising me to think for myself and to value a rewarding and meaningful career.

THIS PAGE INTENTIONALLY LEFT BLANK

CHAPTER 1:

Introduction

1.1 Ignition Overpressure

Ignition overpressure (IOP) is a phenomenon present at the start of an ignition sequence in launch vehicles using solid-grain propellants. When the grain is ignited the pressure inside the combustion chamber quickly rises several orders of magnitude. This drives hot combustion products toward the nozzle and out to the open atmosphere at supersonic speeds. An IOP wave is an unsteady shock wave which originates from the exit plane of the nozzle and propagates spherically outward near sonic conditions. From previous launch data [1]-[3] it is known that overpressures that the body of the rocket experiences are of the order 2:1, or about 15 psi. The region below the nozzle, such as the launch pad trench, will experience further compression due to displacement of gas along the blast wave's direction of propagation and overpressures can be as high as 10:1, or about 130 psi. The portions of the IOP wave that become incident on the rocket body or launch platform components must have an overpressure below a known threshold to avoid costly damage and enable a prolonged lifetime. This is the purpose of the water suppression system which is integrated into the launch platform. The current technique used by NASA and other launch providers is to spray water into the region around the nozzle before ignition. This forces the IOP wave to propagate through water before becoming incident on the rocket body or platform components. Through *several* dissipative mechanisms this causes a sufficient decrease to the pressure jump across the shock, preventing damage.

1.2 Experimental Results on Droplet-Shock Interactions

A survey of empirical data in the literature was carried out [4]-[21] to understand how droplets can be used as a control action in two-phase flow. With blast mitigation as the process of interest, an NRL report [7] isolated several desirable and undesirable effects. Drag on the droplets by the surrounding gas dissipates momentum. As droplets breakup, the gas does work against the surface tension which dissipates energy from the gas. Droplets absorb sensible, latent and radiative heat which further transfers energy from the gas. Since water vapor has a higher heat capacity than air, after water changes phase from liquid to gas the resulting gas mixture can

further absorb heat from the gas. An undesirable effect occurs when liquid turns to water vapor so rapidly that the gas mixture density increase dominates the effect on pressure according to the constitutive relation. The relative importance of each interaction mechanism isn't fully understood and will change depending on the flow regimes.

The flow regime of interest will have shocks present with pressure ratios (2:1-10:1) and temperatures up to several thousand Kelvin. Practical droplet sizes have a diameter D_p less than $500\mu m$. A shock incident on a cloud of water droplets will pass through them so quickly that the droplets will not appear to react until after the shock front is spatially isolated downstream. Droplets will start to get dragged along in the direction of the gas flow, breakup and vaporize. If droplets are large $D_p \geq 100\mu m$, then in the presence of strong shocks they catastrophically breakup into many small droplets $D_p \leq 25\mu m$. Droplet breakup ceases below a Weber number of 12, when inertial forces dominate over surface tension [5]-[8]. Shock attenuation will be greatest when the droplets can sink the most energy out of the gas in a given interval of space. This will cause the greatest decrease in pressure to the driving gas behind the shock. Pressure information will travel at the local sound speed toward the shock front and cause a decrease in pressure equal to the diminished driver gas pressure.

There are general trends in the data which help categorize the relative importance of all of the dissipative mechanisms present. First and foremost, droplet vaporization can extract orders of magnitude more energy from the gas as droplet breakup can. Secondly, the latent heat of vaporization is the most significant dissipative mechanism [8]. Lastly, it has been shown [12] that a non-dimensional droplet-flow parameter can predict overpressure attenuation level, shown in Figure 1.1. The horizontal axis is a non-dimensional flow parameter. The vertical axis is the decrease in overpressure for a shock interacting with droplets divided by the decrease in overpressure when no droplets are present, as measured at a fixed location downstream. Shock tube experiments were conducted which varied the droplet size and shock strength. The data suggests that maximizing the exposed surface area of the droplets will yield the greatest enhancement of IOP attenuation.

1.3 Recent Research on IOP Attenuation

For many years, the water injection strategy for handling the shuttle's IOP transient blast has been based on order-of-magnitude estimates relating the amount of energy dissipation required to the total amount of water used [22]. More than enough water was used and the results were

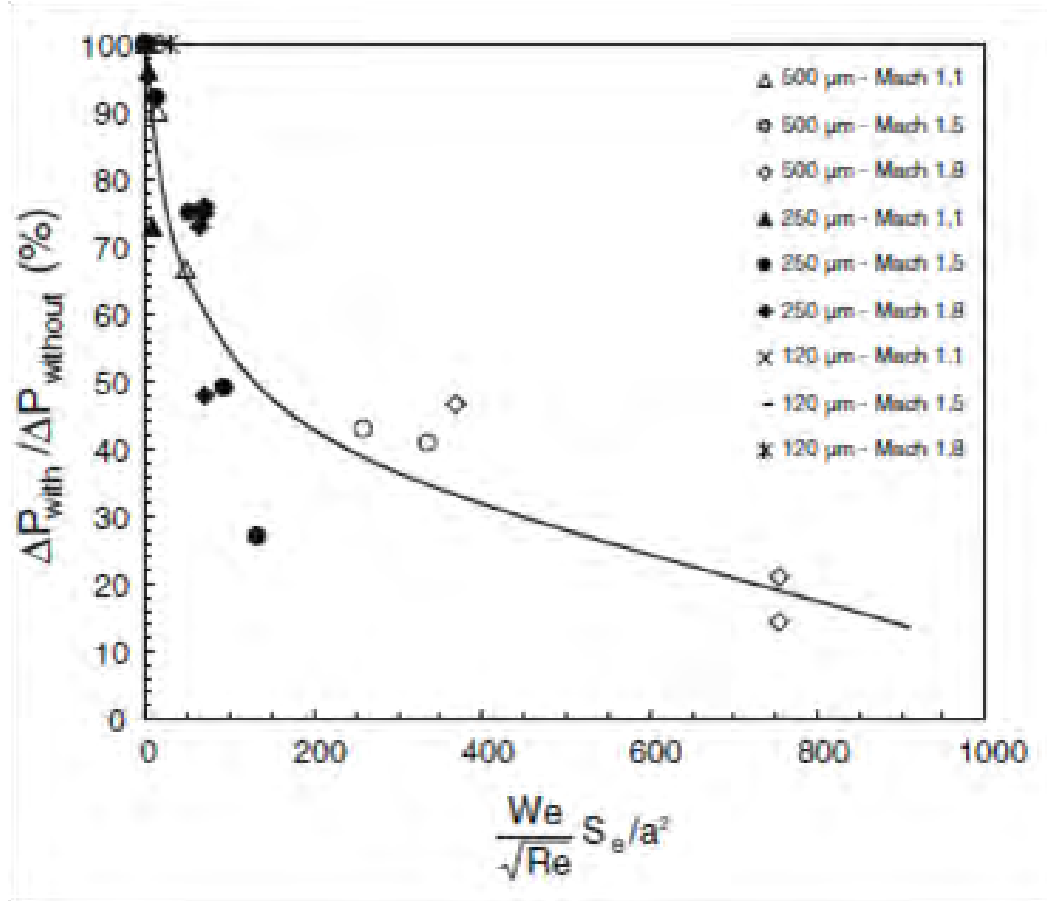


Figure 1.1: Experimental data on IOP attenuation, Jourdan et al. [12]

sufficient. For the heavy lift vehicles of the future, IOP blast waves will be more substantial and require a better understanding of how the water affects the IOP strength. More recently, CFD research is underway at NASA [23]-[26] and in the private sector to predict, with greater precision, the launch environment during ignition for various solid grain rockets [27, 28].

The first work [29] on optimizing one of these precise CFD simulations was a parametric study that looked at water arrangement in the nozzle region and how it affected the maximum IOP strength. At NASA Huntsville, Cannabal showed in his dissertation [29] and a later publication [30] that attenuation is very insensitive to droplet velocity and demonstrated the existence of an optimal water injection arrangement. Water cooling the plume near the nozzle has the greatest desirable effect of attenuating the transmitted IOP strength. However, an excessive amount of water near the nozzle causes obstruction to the blast wave and intensifies pressure. The results suggest an optimal arrangement of water exists but there are still an infinite number of possible

water distributions even in one dimension. Trial and error, or cost gradient methods based on a few discrete inputs are the only option and can yield only coarse notions about continuous optimal water distributions.

1.4 New Contributions of Current Work

The objective of this work is to develop a computational tool that can directly calculate a droplet optimal control for attenuating a range of blast waves to a desired minimal overpressure. As shown in Figure 1.2, the water droplets' control action will be the result of the initial distribution of the water volume fraction variable $\alpha_l(x, 0)$ and the initial droplet diameter. The optimal control $\alpha_l^*(x, 0)$ will be the distribution of water droplets which yields the greatest decrease to the jump in overpressure of the transmitted shock while not using any more water than necessary. Since the two-phase system and resulting control problem are quite complicated, first a single-phase control problem is formulated where the control action is a distributed energy sink behind the shock, a simplification for the way droplet vaporization, the dominant dissipative mechanism, affects the gas flow. A more sophisticated two-phase model [31] is presented and an analogous control problem is formulated in which the control takes the form of the free initial distribution of water and evolves dynamically according to the two-phase model. These control problems are new formulations and the algorithmic solutions developed in order to satisfy all necessary conditions have aspects new to computational results for unsteady shock wave attenuation. Given the mathematical framework presented in Chapter 2 and the numerical methods given in Chapter 3 of this dissertation, engineering results such as those presented in Chapter 4 can be obtained for a given incident blast wave boundary condition.

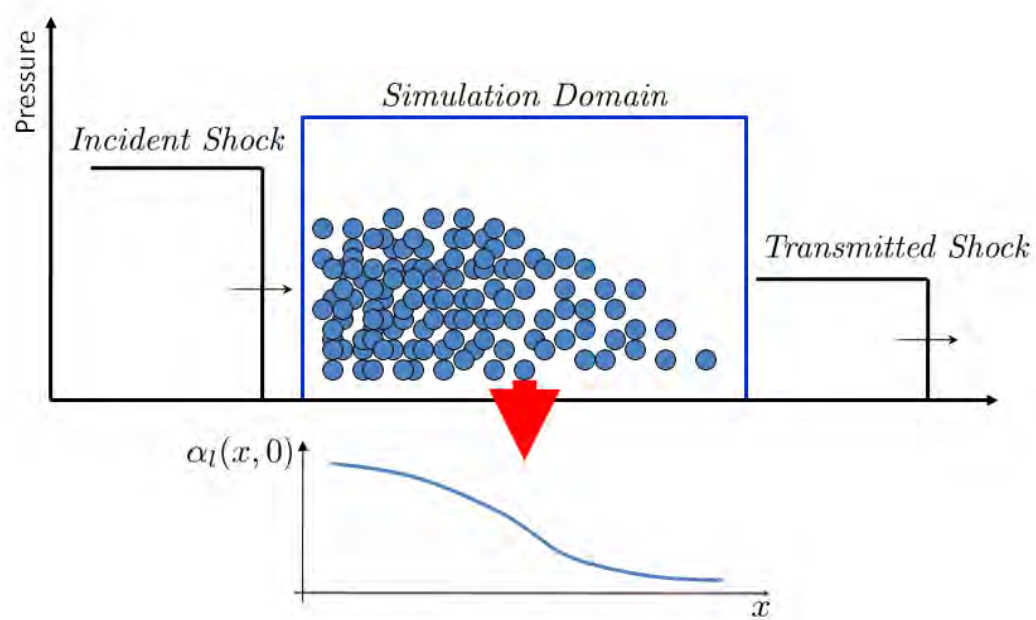


Figure 1.2: Physical diagram of simulated interaction.

THIS PAGE INTENTIONALLY LEFT BLANK

CHAPTER 2:

Mathematical Theory

2.1 Euler System in One Dimension

The mathematical theory of hyperbolic conservation laws has been well established in the 20th century [32]-[36]. In order for a PDE to be an accurate physical system the right conserved quantities must be identified and an entropy condition must exist. The conservation equations dictate that the rate of change of a conserved quantity within a fixed volume equal the flux of that quantity across the volume's surface. The entropy condition selects which conditions are physical when discontinuous solutions are present.

2.1.1 Conservation Equation

The time-dependent Euler Equations are a system of non-linear hyperbolic conservation laws that describe the dynamics of compressible fluids where the effects of viscosity, heat conduction and body forces are negligible. In one spatial dimension there are three conserved quantities: mass density ρ , linear momentum ρu and total energy ρE per unit volume.

$$\frac{\partial}{\partial t} U + \frac{\partial}{\partial x} F(U) = 0 \quad (2.1)$$

$$U = (\rho(x, t), \rho u(x, t), \rho E(x, t))^T \quad (2.2)$$

The state vector of conserved quantities U is a function of a time variable which exists in the interval $[0, T]$ and a single space variable x which exists in a one dimensional domain Ω . $F(U)$ is the non-linear flux of conserved quantities.

$$F(U) = \begin{pmatrix} \rho u \\ \rho u^2 + P \\ u(\rho E + P) \end{pmatrix} \quad (2.3)$$

For an ideal gas, the constitutive relation that relates pressure to internal energy is the ideal gas law.

$$P = \rho e (\gamma - 1) \quad (2.4)$$

The ratio of specific heat is defined $\gamma = \frac{C_p}{C_v}$ where C_p is the specific heat of the gas at constant pressure, divided by that at constant volume C_v . It will be convenient to have the relation between internal energy and temperature for a calorically perfect gas, $e = C_v T$. A final definition relating internal and total energy closes the system from which all thermodynamic quantities can be calculated.

$$\rho E = \rho e + \frac{\rho u^2}{2} \quad (2.5)$$

2.1.2 Quasilinear Form

Equation 2.1 can be written in quasi-linear form by creation of the Jacobian matrix $A = \frac{\partial F}{\partial U}$.

$$\frac{\partial U_i}{\partial t} + A_{ij}(U) \frac{\partial U_j}{\partial x} = 0 \quad (2.6)$$

The elements of the Jacobian matrix are given in Equation 2.7.

$$A(U) = \begin{pmatrix} 0 & 1 & 0 \\ \frac{(\rho u)^2}{\rho^2} \frac{\gamma - 3}{2} & -\frac{(\rho u)}{\rho} (\gamma - 3) & (\gamma - 1) \\ \frac{-\gamma (\rho u) (\rho E)}{\rho^2} + (\gamma - 1) \frac{(\rho u)^3}{\rho^3} & \frac{\gamma (\rho E)}{\rho} - \frac{3}{2} (\gamma - 1) \frac{(\rho u)^2}{\rho^2} & \frac{\gamma (\rho u)}{\rho} \end{pmatrix} \quad (2.7)$$

2.1.3 Primitive Form

The Euler system can be written in the primitive variable basis $\tilde{U} = (\rho, u, P)^T$ by left multiplying Equation 2.6 by $M^{-1} = \frac{\partial \tilde{U}}{\partial U}$ and inserting MM^{-1} between the Jacobian matrix A and the term $\frac{\partial U}{\partial x}$. u is the linear gas velocity and P is the gas pressure. Defining the matrix $\tilde{A} = M^{-1}AM$ gives the primitive form of the Euler system in Equation 2.8. Details of the transformation between bases for a single dimensional fluid flow are given in Merkle [39].

$$\frac{\partial \tilde{U}_i}{\partial t} + \tilde{A}_{ij}(\tilde{U}) \frac{\partial \tilde{U}_j}{\partial x} = 0 \quad (2.8)$$

The elements of \tilde{A} are given in Equation 2.9.

$$\tilde{A}(\tilde{U}) = \begin{pmatrix} u & \rho & 0 \\ 0 & u & 1/\rho \\ 0 & \gamma P & u \end{pmatrix} \quad (2.9)$$

2.1.4 Characteristic Form

It can be shown that \tilde{A} has eigenvalues $(u, u + c, u - c)$ where $c = \sqrt{\gamma RT}$ is the speed of sound in the gas. Any system is hyperbolic if the eigenvalues of the Jacobian matrix are real and distinct. Clearly this is true in the case of the Euler System in 1D. The specific gas constant of air is denoted as R and the gas temperature as T . When the corresponding left eigenvectors multiply dU the characteristics equations are obtained.

$$\begin{aligned} dP - \rho c du &= 0 \quad \text{along} \quad dx/dt = u - c \\ dP - c^2 d\rho &= 0 \quad \text{along} \quad dx/dt = u \\ dP + \rho c du &= 0 \quad \text{along} \quad dx/dt = u + c \end{aligned} \quad (2.10)$$

Solving the Riemann Problem for the unsteady Euler Equations amounts to constructing the rest of the flow field between these characteristic waves, either approximately or iteratively up

to arbitrary precision [40].

The method of characteristics takes advantage of the property that hyperbolic systems have distinct finite wave speeds. If an observer is traveling at a characteristic speed the observer will measure an invariant quantity of the flow. The 1D Euler system in characteristic form is given in Equation 2.11. It is obtained in a way analogous to the transformation between Equations 2.6 and 2.8. The matrix Λ is diagonal and its elements (eigenvalues) λ_i are the real and distinct wave speeds $(u, u + c, u - c)$.

$$\frac{\partial \hat{U}}{\partial t} + \Lambda \frac{\partial \hat{U}}{\partial x} = 0 \quad (2.11)$$

Traveling at the characteristic speeds, an observer would measure the Riemann invariants $\hat{U} = (S/R, \Gamma c + u, \Gamma c - u)^T$ as constant. S is the entropy, R is the specific gas constant, c is the speed of sound and $\Gamma = 2/(\gamma - 1)$. Traveling at the speed of a shock wave means that the shock will never traverse the observer and hence the observer will never see an increase in entropy. Indeed, the Riemann invariants are useful for analyzing isentropic portions of compressible flows such as rarefaction waves.

2.1.5 Well-Posedness

For hyperbolic conservation laws, a well-posed problem requires real and distinct eigenvalues of the system's Jacobian matrix [37]. This is equivalent to the existence of a symmetrizer matrix \tilde{S} that has real, positive definite elements and has the property that $\tilde{S}A$ is symmetric. It can be shown that the 1D Euler System has a symmetrizer matrix as long as density, or temperature remain positive [43]. This assumption is built in to the notions of either quantities therefore the system is always symmetrizable and hence the Riemann Problem for the Euler Equations is well-posed.

2.1.6 Entropy and Shocks

From the definition of entropy and the primitive form of the mass and momentum conservation equations it can be shown that entropy is constant along $dx/dt = u$. That is, regions of smooth flow are isentropic. The presence of a discontinuity in velocity necessitates that a shock wave has formed where the jump in flow quantities are determined uniquely by the Rankine-Hugoniot Jump Conditions. For a shock wave moving left to right, denote the state just behind the shock

U_L and the state immediately upstream of the shock U_R . The jump quantities, denoted with square brackets $[]$, are given in Equation 2.12.

$$\begin{aligned}\partial F(U) &\rightarrow [F(U)] = F(U_R) - F(U_L) \\ \partial(U) &\rightarrow [U] = U_R - U_L\end{aligned}\tag{2.12}$$

Rearranging Equation 2.12 gives the shock speed in terms of the jump across the shock. Equation 2.13 is the Rankine-Hugoniot jump conditions obtained without any specification to a fluid. This condition is a property of any shock wave in a hyperbolic system.

$$\frac{\partial x}{\partial t}|_{shock} = \left| \frac{[F(U)]}{[U]} \right| \tag{2.13}$$

Applying Equation 2.13 to the Euler Equations moving at the shock speed gives the jump in primitive variables in a coupled system of algebraic equations which can be solved iteratively as will be described in Chapter 3. In addition, an alternative numerical method of Godunov will be described which is conservative and, with a stability criteria, obeys Equation 2.13 without an iterative solver.

Since the eigenvalues are increasing functions of the state variables, the the flux is convex with respect to U . Lax [32],[33] showed that this requires characteristics on either side of a shock to run into that shock. For a system with a right moving shock the entropy condition is given in Equation 2.14 for k number of waves where $1 \leq k \leq n$, and n is the number of characteristic waves.

$$\begin{aligned}\lambda_{k-1}(U_L) &< \frac{\partial x}{\partial t}|_{shock} < \lambda_k(U_L) \\ \lambda_k(U_R) &< \frac{\partial x}{\partial t}|_{shock} < \lambda_{k+1}(U_R)\end{aligned}\tag{2.14}$$

Intuitively, this agrees with the physical notion that entropy only increases. For the 1D Euler system $n = 3$. Since a shock requires supersonic conditions the shock speed must be faster

than the fastest rate at which any information can travel in the ambient upstream Right state, so it must be true that $k = 3$. This means that the entropy condition also requires exactly one characteristic in the Left state behind the shock to be faster than the shock itself. The shock is driven by the upstream pressurized gas which must communicate its presence via the $u + c$ characteristic in the Left state. This is not hard to believe since the jump conditions show that static temperature increases across the shock which raises the speed of sound in the Left state. Figure 2.1 shows the instantaneous wave pattern of a shock wave formed from a discontinuous and stationary initial condition.

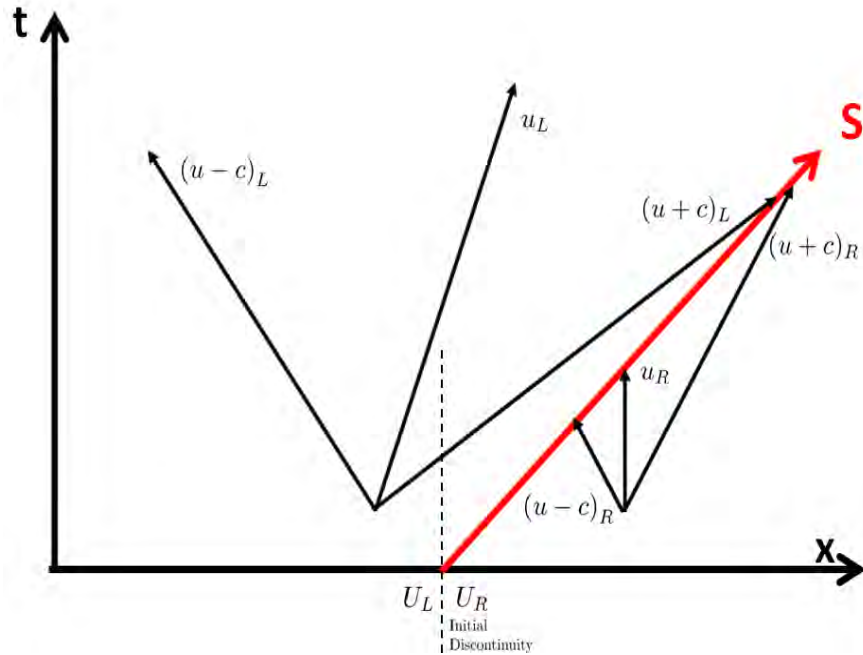


Figure 2.1: Instantaneous wave patterns of a Left and Right state and shock wave which obey the entropy condition of the Euler system in 1D

From the first law of thermodynamics the entropy between states 'L' and 'R' is given in Equation 2.15.

$$s_L - s_R = -R \cdot \ln \frac{P_{0L}}{P_{0R}} \quad (2.15)$$

P_{0L} and P_{0R} are the total pressures to the left and right of the shock respectively. From manip-

ulation of Rankine Hugoniot Jump conditions it can be shown that for supersonic flows there is necessarily a decrease in total pressure, verifying by Equation 2.15 that indeed, Lax's mathematic entropy condition on the Euler system in one spatial dimension yields the thermodynamic principle that entropy can only increase across a shock.

2.1.7 The Riemann Problem

The Riemann Problem is an initial value problem where the initial data has a discontinuity.

$$U(x, 0) = \begin{cases} U_L & x < 0 \\ U_R & x > 0 \end{cases} \quad (2.16)$$

For gas dynamics, the Riemann Problem is the general form of the shock tube problem [40]. Two stationary gases, one at significantly higher pressure and possibly temperature, are separated by a thin wall. As the thin wall ruptures, a shock wave propagates into the gas held at lower pressure while a rarefaction wave travels through the gas held at higher pressure. Initially a density discontinuity exists between the two gases and this contact surface propagates into the lower pressure gas at the speed determined by the jump in velocity at the shock. The shock travels at the speed of the gas behind it plus the speed of sound of the *low* pressure gas. The rarefaction wave travels in the opposite direction of the gas at a speed equal to the speed of the gas minus the speed of sound in the *high* pressure gas. The wave pattern of the shock tube problem at the instant the diaphragm bursts is shown in Figure 2.2.

It is worth pointing out that the fastest wave speed may be $u - c$ since the speed of sound may be much greater in the high pressure gas. In Chapter 3, the maximum wave speed will determine the maximum allowable timestep discretization and, therefore, computing expense.

By algebraic manipulation of the Rankine-Hugoniot Jump Condition and the isentropic equation of state for an ideal gas it can be proven [40] that solving the Riemann Problem for the Euler system amounts to finding the root p^* of Equation 2.17.

$$f(p^*, \tilde{U}_L, \tilde{U}_R) = f_L(p^*, \tilde{U}_L) + f_R(p^*, \tilde{U}_R) + [\tilde{U}] = 0 \quad (2.17)$$

The rest of the primitive variables u^*, ρ^* can be uniquely calculated from p^* and the correct

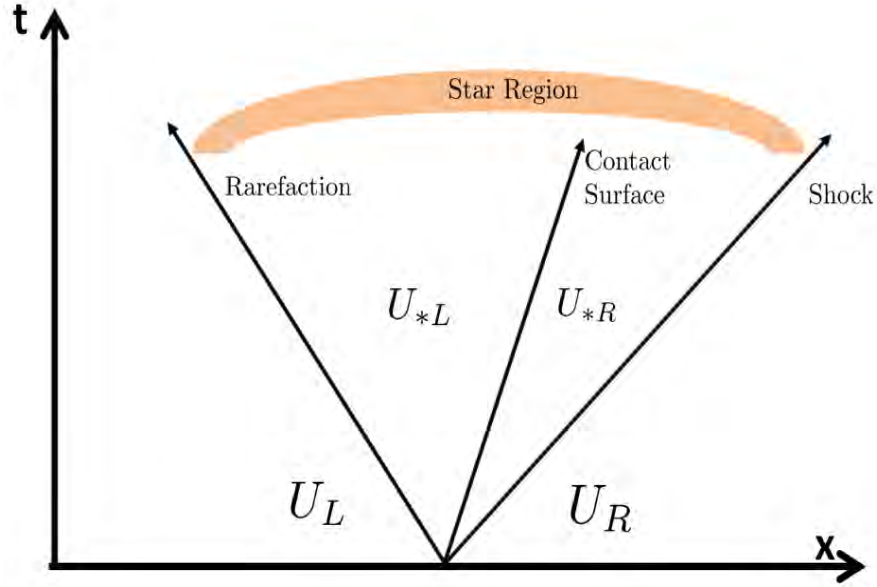


Figure 2.2: Solution regions of the shock tube problem and wave pattern at the initial instant the diaphragm bursts

definition of f_L and f_R . The present analysis will be restricted to a left moving rarefaction wave and a right moving shock wave. The isentropic relation between pressure and density holds across rarefaction waves. Solution to the flow in the U_{*L} region is derived from the constant U_L state. By combining the isentropic relation and the Riemann invariants f_L for a left moving rarefaction can be written in terms of the constant left state U_L and the free variable p^* in Equation 2.16. c_L is the speed of sound in the constant U_L state.

$$f_L(p, \tilde{U}_L) = \frac{2c_L}{\gamma - 1} \left(\left(\frac{p}{p_L} \right)^{\frac{\gamma-1}{2\gamma}} - 1 \right) \quad (2.18)$$

f_R in the U_{*R} region is determined by the constant U_R state and the Rankine-Hugoniot jump conditions. Applying Equation 2.13 to the 1D Euler Equations in a frame of reference moving along with the shock gives the jump conditions and, with some rearranging, yields f_R for a right moving shock wave.

$$f_R(p, \tilde{U}_R) = (p - p_R) \left(\frac{A_R}{p + B_R} \right)^{1/2} \quad (2.19)$$

The constants A_R and B_R are given in Equation 2.20. The flow can be uniquely determined at any time in the star region given a physical initial condition.

$$\begin{aligned} A_R &= \frac{2}{(\gamma + 1) \rho_R} \\ B_R &= \frac{(\gamma - 1)}{(\gamma + 1)} p_R \end{aligned} \quad (2.20)$$

The exact solution requires an iterative procedure at every sample point in space and at any desired moment in time. This is not practical for large domains or for the added complexity of another phase. The difficulty in accuracy of any approximate solution to the Riemann Problem comes from any discontinuities at shock fronts. Here finite difference methods fail and a finite volume method based on the integral form of the conservation equation, rewritten in Equation 2.21, is better suited.

$$\int_{x_1}^{x_2} U(x, t_2) dx = \int_{x_1}^{x_2} U(x, t_1) dx + \int_{t_1}^{t_2} F(U(x_1, t)) dt - \int_{t_1}^{t_2} F(U(x_2, t)) dt \quad (2.21)$$

No discretization or approximation has been made in Equation 2.21 and it is true for any general domain $[x_1, x_2] \times [t_1, t_2]$.

Numeric schemes based on primitive variables fail at shock waves. If the jump in quantities across the shock are wrong, the shock speed will be wrong and therefore, over time, the location will be wrong as well. Only schemes based on conservative variables have acceptable accuracy near shocks. A numeric method is conservative only if the approximate numerical flux is constructed in such a way that each quantity is conserved at every time step. In particular, Lax [36] showed that conservative methods that are also convergent will converge to the correct weak solution at shocks. With that in mind, Godunov's Method with a suitable choice of numerical flux will be described in Chapter 3 and used for all results shown in Chapter 4.

2.2 Two-Phase Flow Model

2.2.1 Assumptions

The vast majority of the two-phase flow model is based on the work of Saurel and Abgrall [31],[41]. It consists of six balance laws and a seventh non-conservative PDE for the volume fraction variable. The model was chosen because it maintains a hyperbolic structure and is applicable to physical phenomena of interest, water droplet-shock interactions. This is achieved by considering both phases or fluids as compressible, by assuming many droplets per cell and therefore homogenized interface conditions and by solving the same set of equations everywhere in space.

2.2.2 Balance Equations

The conservative vector of the flow is again denoted as U . The subscripts in Equation 2.22 denote gas or liquid.

$$U = (\alpha_g, \alpha_g \rho_g, \alpha_g \rho_g u_g, \alpha_g \rho_g E_g, \alpha_l \rho_l, \alpha_l \rho_l u_l, \alpha_l \rho_l E_l)^T \quad (2.22)$$

$$\frac{\partial \alpha_g}{\partial t} + V_i \frac{\partial \alpha_g}{\partial x} = 0 \quad (2.23)$$

$$\frac{\partial}{\partial t} \begin{pmatrix} \alpha_g \rho_g \\ \alpha_g \rho_g u_g \\ \alpha_g \rho_g E_g \\ \alpha_l \rho_l \\ \alpha_l \rho_l u_l \\ \alpha_l \rho_l E_l \end{pmatrix} + \frac{\partial}{\partial x} \begin{pmatrix} \alpha_g \rho_g u_g \\ \alpha_g \rho_g u_g^2 + \alpha_g P_g \\ u_g (\alpha_g \rho_g E_g + \alpha_g P_g) \\ \alpha_l \rho_l u_l \\ \alpha_l \rho_l u_l^2 + \alpha_l P_l \\ u_l (\alpha_l \rho_l E_l + \alpha_l P_l) \end{pmatrix} = \begin{pmatrix} 0 \\ P_i \\ P_i V_i \\ 0 \\ -P_i \\ -P_i V_i \end{pmatrix} \frac{\partial \alpha_g}{\partial x} + S(U) \quad (2.24)$$

The gas phase obeys the ideal gas equation of state while the stiffened gas equation of state is used for the liquid.

$$\rho_g e_g = \frac{P_g}{\gamma - 1} \quad (2.25)$$

$$\rho_l e_l = \frac{P_l + \pi_l \gamma_l}{\gamma_l - 1} \quad (2.26)$$

$\gamma = 1.4$ is the gas constant of air, $\gamma_l = 4.4$ is the analogous constant for water [31] and $\pi_l = 6 \cdot 10^8$ Pa is the stiffening constant that makes large changes in liquid pressure produce almost no changes in density. Equations 2.27 and 2.28 are closure relations for the internal energy ρe to the total energy ρE , per unit volume, for each phase.

$$\rho_g E_g = \rho_g e_g + \frac{1}{2} \rho_g u_g^2 \quad (2.27)$$

$$\rho_l E_l = \rho_l e_l + \frac{1}{2} \rho_l u_l^2 \quad (2.28)$$

2.2.3 Interface Quantities

The volume fraction will propagate at a mean inter-facial velocity which is a center-of-mass estimate given in Equation 2.29.

$$V_i = \frac{\alpha_g \rho_g u_g + \alpha_l \rho_l u_l}{\alpha_g \rho_g + \alpha_l \rho_l} \quad (2.29)$$

E_i and P_i are volume averages of total energy and pressure respectively at the interface shown in Equation 2.30.

$$\begin{aligned} E_i &= \alpha_g E_g + \alpha_l E_l \\ P_i &= \alpha_g P_g + \alpha_l P_l \end{aligned} \quad (2.30)$$

The sum of the volume fractions of each phase will always equal 1 for all $x \in \Omega$.

$$\alpha_g + \alpha_l = 1 \quad (2.31)$$

When either volume fraction tends toward zero, the 1D Euler system is recovered.

2.2.4 Primitive Form

As with the single-phase Euler system, the two-phase system can be written in non-conservative form. Again let \tilde{U} be the primitive vector.

$$\tilde{U} = (\alpha_g, \rho_g, u_g, P_g, \rho_l, u_l, P_l)^T \quad (2.32)$$

In this basis the Jacobian matrix for the system of Equations 2.23 and 2.24 is given in Equation 2.33.

$$\tilde{A}(\tilde{U}) = \begin{pmatrix} V_i & 0 & 0 & 0 & 0 & 0 & 0 \\ \frac{\rho_g}{\alpha_g}(V_i - u_g) & u_g & \rho_g & 0 & 0 & 0 & 0 \\ \frac{P_g - P_i}{\alpha_g \rho_g} & 0 & u_g & 1/\rho_g & 0 & 0 & 0 \\ \frac{\rho_g c_{gi}^2}{\alpha_g}(V_i - u_g) & 0 & \rho_g c_g^2 & u_g & 0 & 0 & 0 \\ \frac{\rho_l}{\alpha_l}(V_i - u_l) & 0 & 0 & 0 & u_l & \rho_l & 0 \\ \frac{P_l - P_i}{\alpha_g \rho_g} & 0 & 0 & 0 & 0 & u_l & 1/\rho_l \\ \frac{\rho_l c_{li}^2}{\alpha_l}(V_i - u_l) & 0 & 0 & 0 & 0 & \rho_l c_l^2 & u_l \end{pmatrix} \quad (2.33)$$

The source term $H(U)$ which multiplies $\frac{\partial \alpha_g}{\partial x}$ in Equation 2.24 has been coupled into the Jacobian matrix and the two-phase quasi-linear system now has the form shown in Equation 2.34.

$$\frac{\partial \tilde{U}_i}{\partial t} + \tilde{A}_{ij}(\tilde{U}) \frac{\partial \tilde{U}_j}{\partial x} = S_i(\tilde{U}) \quad (2.34)$$

With this fortunate manipulation, the seven eigenvalues can be found by diagonalizing $\tilde{A}(\tilde{U})$. The characteristic speeds are $(V_i, u_g, u_g - c_g, u_g + c_g, u_l, u_l - c_l, u_l + c_l)$, where c_l is the local speed of sound in the liquid phase. The velocity of the phase interface is the seventh characteristic wave speed of the system. All are distinct except locally where they are degenerately zero.

2.2.5 Phase Interactions

The source vector $S(U)$ is broken up into three separate interactions as defined in Equation 2.35.

$$S(U) = MH(U) + VR(U) + PR(U)$$

$$= \begin{pmatrix} 0 \\ \dot{m} \\ \dot{m}V_i \\ \dot{m}(L_{hv} + E_i) + Q_i \\ -\dot{m} \\ -\dot{m}V_i \\ -\dot{m}(L_{hv} + E_i) - Q_i \end{pmatrix} + \begin{pmatrix} 0 \\ 0 \\ F_d \\ F_dV_i \\ 0 \\ -F_d \\ -F_dV_i \end{pmatrix} + \begin{pmatrix} \mu(P_g - P_l) \\ 0 \\ 0 \\ -\mu P_i(P_g - P_l) \\ 0 \\ 0 \\ \mu P_i(P_g - P_l) \end{pmatrix} \quad (2.35)$$

The source vector for mass and heat exchange between the phases is denoted as $MH(U)$. The source terms for velocity and pressure equilibration are $VR(U)$ and $PR(U)$ respectively. As Saurel and Abgrall point out [31], an interface separating two phases must reach the same pressure through microscopic interactions. Indeed, without enforcing this condition, notions of thermodynamic properties such as temperature cannot be determined and numerical oscillations due to pressure differences will grow without significant artificial dissipation.

The equilibrium condition $P_g = P_l$ is chosen thereby neglecting the effect of surface tension. As stated in Chapter 1, the effect of droplet breakup is omitted in favor of vaporization since the latter can be shown to be much more significant of an energy sink to the gas. The microscopic pressure equilibration causes a volume and internal energy variation of each phase. Details of the solution procedure for the two-phase model are saved for Chapter 3. Isolating the ODE $\frac{\partial U}{\partial t} = PR(U)$ in Equation 2.35 yields conditions better suited to computation.

$$\frac{\partial \alpha_g}{\partial t} = \mu(P_g - P_l) \quad (2.36)$$

$$\frac{\partial \alpha_g \rho_g E_g}{\partial t} = \mu P_i(P_g - P_l) \quad (2.37)$$

$$\frac{\partial \alpha_g \rho_l E_l}{\partial t} = -\mu P_i(P_g - P_l) \quad (2.38)$$

Therefore, Equations 2.36-2.38 simplify to Equations 2.39 and 2.40

$$\frac{\partial \alpha_g \rho_g E_g}{\partial t} = P_i \frac{\partial \alpha_g}{\partial t} \quad (2.39)$$

$$\frac{\partial \alpha_g \rho_l E_l}{\partial t} = -P_i \frac{\partial \alpha_g}{\partial t} \quad (2.40)$$

In a closed system, this is just the first law of thermodynamics for an isentropic transformation. Time integration of both sides yields conditions given in Equations 2.41 and 2.42 whose solution will be discussed in Chapter 3.

$$(\alpha_g \rho_g E_g)^{PR} - (\alpha_g \rho_g E_g)^0 = \int_{\alpha_g^0}^{\alpha_g^{PR}} P_i d\alpha_g \quad (2.41)$$

$$(\alpha_l \rho_l E_l)^{PR} - (\alpha_l \rho_l E_l)^0 = - \int_{\alpha_g^0}^{\alpha_g^{PR}} P_i d\alpha_g \quad (2.42)$$

The superscript ^{PR} denotes the solution to the ODE for pressure relaxation while ⁰ denotes the starting value which comes from the solution to the balance PDE at the current time step. The drag force F_d exerted by the gas onto a spherical water droplet, which is responsible for the $VR(U)$ source term, is given by the empirical drag law in Equation 2.43

$$F_d = C_d \rho_g D_p^2 \alpha_l (u_g - u_l)^2 \quad (2.43)$$

where D_p is the diameter of the water droplet. This is a dynamic variable distributed in space with the assumption of locally mono-dispersed droplets. C_d is a constant drag coefficient.

The exchange of mass and heat between the phases will be due to vaporization of liquid water droplets by the surrounding gas. The rate of gaseous mass production in the form of water vapor from the liquid phase, \dot{m} , is defined in Equation 2.44.

$$\dot{m} = \rho_{H_2Ov} (P_g) \dot{\alpha}_l \quad (2.44)$$

The rate of change of the volume fraction of water within a fixed volume of space Δx^3 is related

to the diameter rate of change via Equation 2.45.

$$\dot{\alpha}_l = \frac{S_p}{\Delta x^3} \frac{\partial D_p}{\partial t} \quad (2.45)$$

S_p denotes the total surface area of droplets per a fixed volume defined in Equation 2.46.

$$S_p = 4\pi \left(\frac{D_p}{2} \right)^2 N_p \quad (2.46)$$

N_p is the number of droplets per the same fixed volume as is uniquely determined by the volume fraction of water α_l for mono-dispersed droplets.

$$N_p = \alpha_l \cdot \frac{\Delta x^3}{\frac{4}{3}\pi \left(\frac{D_p}{2} \right)^3} \quad (2.47)$$

The evolution of droplet size needed in Equation 2.47 is determined by the rate of vaporization. In this work, the Empirical-Beta Vaporization law is implemented with constant values coming from [7].

$$\frac{\partial D_p^2}{\partial t} = -\beta(T_g) \quad (2.48)$$

$$\beta(T_g) = 7600 \left(1 + 7.4 \cdot 10^{-7} (T_g - 300K)_+ \right)^{2.7548} \mu m^2/s \quad (2.49)$$

As will be demonstrated in Chapter 4, the range of pressure magnitude for the flows of interest to the IOP attenuation problem are from 1-10 atm. According to steam tables [42], the water vapor density will vary by an order of magnitude over this pressure range. Consequently, water droplet vaporization will be much more effective to high pressure shocks. Equation 2.50 is the least-squares quadratic fit to the steam table data for water vapor density as a function of the surrounding gas pressure.

$$\rho_{H_2Ov}(P_g/atm) \approx -.0024344 \cdot P_g^2 + .5368 \cdot P_g - .077246 \text{ kg}/m^3 \quad (2.50)$$

The latent heat of vaporization of water at its boiling point $L_{hv} = 2.26$ MJ/kg.

The last term in the $MH(U)$ vector, Q_i is the rate of heat exchange between phases at the interface given in Equation 2.51.

$$Q_i = hS_p(T_g - T_l) \quad (2.51)$$

h is the heat transfer coefficient. For water droplets of diameter D_p , $h = \frac{Nu\lambda}{D_p}$ where Nu is the Nusselts Number and $\lambda = 0.6$ W/mK, is the thermal conductivity of water.

2.2.6 Well-Posedness

The Jacobian matrix in Equation 2.33 is symmetrizable if, in addition to the restriction in the 1D Euler System, the volume fraction of each phase remain non-zero [31]. Since our model dictates that the same equations be solved in each cell, this restriction is not a problem.

The eigenvalues of \tilde{A} above are $(V_i, u_g, u_g - c_g, u_g + c_g, u_l, u_l - c_l, u_l + c_l)$. From the definition for interface velocity and sound speeds it can be seen that all these eigenvalues are real and distinct if a few conditions hold. If there are regions in our domain where a single phase is completely absent, then the interface velocity will be degenerate to the velocity of the phase 100% present. Therefore, our calculation restricts the volume fraction of either phase to remain above a certain small threshold. As with the single-phase Euler system in one dimension, well-posedness can be shown by the existence of a real, positive definite symmetrizer. It was shown by Texier [43] that a necessary condition on the positive-definiteness of the symmetrizer depends on the positiveness of a certain constitutive variable that should always physically be positive such as density, temperature etc. The multi-phase system has the same requirement. In addition, compressible flow has been shown to change type from hyperbolic to elliptic where the eigenvalues of the system are complex. A famous example is the sonic bubble in aerodynamics [44]. In that case, the flow is irrotational and allows a velocity potential formulation which, in polar coordinates, will change type at the sonic line. Since the flow is steady, a steady sonic bubble develops inside in which the flow is elliptic and hence hyperbolic flux-based conservative numeric methods would fail. Blast waves, on the other hand, are unsteady and not irrotational. Any sonic regions of the flow are dynamic and do not form sonic bubbles.

2.3 Optimal Control of Systems of Partial Differential Equations

Optimal control theory and the Pontryagin Minimum Principle are well-established in mathematical and applied engineering literature [45]-[52].

2.3.1 Derivation of Necessary Conditions of General Optimal System

This section contains a general derivation for all the necessary first-order conditions of optimality when the dynamical constraints are a system of partial differential equations with free or fixed initial and final data, free or fixed spatial boundary data and free final time. In Section 2.4.2 the general conditions are applied to the unsteady Euler Equations in 1D to formulate a shock attenuation problem and to a two-phase flow problem in Section 2.4.3 governed by the model given in Section 2.2.

To start, a hyperbolic system of balance laws under a distributed control action z_i written in a general conservative-flux form using tensors is shown in Equation 2.52.

$$\frac{\partial U_i}{\partial t} + \frac{\partial}{\partial x_k} F_i^k(U) = S_i(U) + z_i \quad (2.52)$$

where $i = 1, \dots, m$ where m is the number of state variables and $k = 1, \dots, n$ where n is the number of spatial dimensions. If the derivatives of the flux vector is taken with respect to the state vector U , a Jacobian matrix A^k for each of the k^{th} spatial dimensions is defined.

$$A_{ij}^k(U) = \frac{\partial}{\partial U_j} F_i^k(U) \quad (2.53)$$

The state dynamics can then be written in matrix Jacobian form. It is important to mention here that writing the PDE system in Jacobian form does not imply that this is the form used to solve the flow. For flows with shock waves, conservative methods are necessary and lend themselves to the conservative-flux form of the equations. However, the adjoint system of equations derived below are derived from the Jacobian form and are always linear in the adjoint variables, making their numerical solution easier.

$$\frac{\partial U_i}{\partial t} + A_{ij}^k(U) \frac{\partial U_j}{\partial x_k} = S_i(U) + z_i \quad (2.54)$$

A non-linear partial differential operator N can be defined so that:

$$N(U, z) = \frac{\partial U_i}{\partial t} + A_{ij}^k(U) \frac{\partial U_j}{\partial x_k} - S_i(U) - z_i = 0 \quad (2.55)$$

After the dynamical system is known, a cost, or objective, functional must be intelligently defined. In the most general framework there can be a cost associated with the initial data I , a cost involving the final data K and a running cost L that accumulates over the time interval of the control problem $[0, T]$. So far, initial and final data can still be free or fixed, no restriction has been made. The cost functionals describe the objective associated with how these parameters are distributed. Let J be the total cost functional.

$$J = I(U(\cdot, 0)) + K(U(\cdot, T)) + \int_0^T L(U, z) dt \quad (2.56)$$

To incorporate the constraint in the minimization, N is multiplied by a generic continuous vector $V(x, t)$ and added to J . The problem then becomes minimizing the augmented cost functional \tilde{J} .

$$\tilde{J} = I(U(\cdot, 0)) + K(U(\cdot, T)) + \int_0^T L(U, z) + (V, N(U, z)) dt \quad (2.57)$$

It is standard to refer to $V_i(x, t)$ as the Lagrange multiplier or adjoint vector. It is a m -dimensional vector since there is an adjoint state for every state variable.

Let (z^*, U^*, V^*, T^*) be the optimal control, state vector, adjoint vector and final time respectively. Let a perturbed control function δz be added to the optimal control solution so that:

$$z = z^* + \epsilon \delta z \quad (2.58)$$

where $\epsilon > 0$ is a small constant. The perturbed optimal control introduces a perturbation to the optimal state and adjoint state:

$$U = U^* + \epsilon \delta U \quad (2.59)$$

$$V = V^* + \epsilon \delta V \quad (2.60)$$

Another way to see δU which will be useful shortly is:

$$\delta U = \frac{d}{d\epsilon} U(z^* + \epsilon \delta z) |_{\epsilon=0} \quad (2.61)$$

It has been pointed out in the literature [53]-[55] that if the state variables have shocks, a perturbation is not small in the neighborhood of the shock and does not have the vanishing properties as $\epsilon \rightarrow 0$. A slight increase in the amplitude behind the shock perturbs the speed shock and therefore also the location of the shock front. This causes small perturbations to induce variations on the order of the jump across the shock. The presented method of solution avoids this issue, as will be demonstrated later. Since only decreasing the amplitude of a shock wave is desired it is apparent that any realistic control action will only slow the shock wave down. The target state $Q(x)$ and final time penalty will be constructed in such a way that all variations of the solution will occur *upstream* of the shock front only. Matching the simulated pressure profile under control action with the target final state near the shock front will occur by allowing the final time to be free. Henceforth, it can be assumed that all variations are taken in smooth regions of the flow and that the solution procedure will not depend on a shock location variable and adjoint state, nor is a more sophisticated variation required.

The first order necessary optimal condition that must be satisfied by perturbed control, state, adjoint state and final time $(\delta z, \delta U, \delta V, \delta t)$ is:

$$\frac{d}{d\epsilon} \tilde{J}(z^* + \epsilon \delta z) |_{\epsilon=0} = 0 \quad (2.62)$$

$$\begin{aligned}
&= \frac{d}{d\epsilon} I(U(z^* + \epsilon \delta z))|_{\epsilon=0} + \frac{d}{d\epsilon} K(U(z^* + \epsilon \delta z))|_{\epsilon=0} \\
&+ \frac{d}{d\epsilon} \int_0^T L(U(z^* + \epsilon \delta z), z^* + \epsilon \delta z)|_{\epsilon=0} + (V^* + \epsilon \delta V, N(U(z^* + \epsilon \delta z), z^* + \epsilon \delta z))|_{\epsilon=0} dt \\
&= \frac{d}{d\epsilon} I(U(z^* + \epsilon \delta z))|_{\epsilon=0} + \frac{d}{d\epsilon} K(U(z^* + \epsilon \delta z))|_{\epsilon=0} \\
&+ \int_0^T \frac{d}{d\epsilon} L(U(z^* + \epsilon \delta z), z^* + \epsilon \delta z)|_{\epsilon=0} + \frac{d}{d\epsilon} (V^* + \epsilon \delta V, N(U(z^* + \epsilon \delta z), z^* + \epsilon \delta z))|_{\epsilon=0} dt \\
&+ (L + (V^*, N(U^*, z^*)))|_{t=T} \delta t = 0 \\
&= \left(\frac{\partial I}{\partial U}, \delta U(x, 0) \right) + \left(\frac{\partial K}{\partial U}, \delta U(x, T) \right) + \int_0^T \left(\frac{\partial L}{\partial U}, \delta U(x, t) \right) \\
&+ \left(\frac{\partial L}{\partial z}, \delta z(x, t) \right) + (V^*, N(U^*, V^*)) + \left(V^* + \epsilon \delta V, \frac{d}{d\epsilon} N(U(z^* + \epsilon \delta z), z^* + \epsilon \delta z) \right)|_{\epsilon=0} dt \\
&+ (L + (V^*, N(U^*, z^*)))|_{t=T} \delta t
\end{aligned}$$

(The second term in the second line is zero since $N = 0$).

$$\begin{aligned}
&= \left(\frac{\partial I}{\partial U}, \delta U(x, 0) \right) + \left(\frac{\partial K}{\partial U}, \delta U(x, T) \right) \\
&+ \int_0^T \left(\frac{\partial L}{\partial U}, \delta U(x, t) \right) + \left(\frac{\partial L}{\partial z}, \delta z(x, t) \right) + \left(V^*, \frac{d}{d\epsilon} N(U(z^* + \epsilon \delta z), z^* + \epsilon \delta z) \right)|_{\epsilon=0} dt \\
&+ (L + (V^*, N(U^*, z^*)))|_{t=T} \delta t = 0
\end{aligned} \tag{2.63}$$

This is a good place to see structure of the equations. In Equation 2.63 it is easier to see the Frechet derivative analogously as a regular chain rule derivative. It is worth noting that in this form the equation is valid for any differential operator N , linear or non-linear, PDE or ODE. Note that the components of the objectives I, K, L are clearly separated and what remains is to carry the perturbation and differentiation with respect to ϵ through on the differential operator and then integrate by parts to get the adjoint partial differential system with boundary condi-

tions. That term in the above equation can *now* be written in the Jacobian matrix form with an assumption that the eigenvalues are real and distinct.

$$\begin{aligned}
& \left(V^*, \frac{d}{d\epsilon} N(U(z^* + \epsilon \delta z), z^* + \epsilon \delta z) \Big|_{\epsilon=0} \right) = \\
& \left(V^*, \frac{d}{d\epsilon} \left[\frac{\partial U(z^* + \epsilon \delta z)}{\partial t} + A(U(z^* + \epsilon \delta z)) \frac{\partial U(z^* + \epsilon \delta z)}{\partial x} - S(U(z^* + \epsilon \delta z)) - (z^* + \epsilon \delta z) \right] \Big|_{\epsilon=0} \right) \\
& = \left(V^*, \frac{\partial \delta U}{\partial t} \right) + \left(V^*, \frac{d}{d\epsilon} A(U(z^* + \epsilon \delta z)) \frac{\partial U(z^* + \epsilon \delta z)}{\partial x} \Big|_{\epsilon=0} \right) - \left(V^*, \frac{\partial S}{\partial U} \delta U \right) - (V^*, \delta z)
\end{aligned} \tag{2.64}$$

The last line shows the differential terms separated and makes use of the definition of δU . The last two terms in Equation 2.64 are simple to handle but the first two require more work. It is now necessary to use tensor notation.

Term 1

$$\begin{aligned}
& \left(V_i^*, \frac{d}{d\epsilon} \frac{\partial U_i(z^* + \epsilon \delta z)}{\partial t} \right) \Big|_{\epsilon=0} \\
& = \left(V_i^*, \frac{\partial}{\partial t} \frac{dU_i(z^* + \epsilon \delta z)}{d\epsilon} \right) \Big|_{\epsilon=0} \\
& = \left(V_i^*, \frac{\partial \delta U_i}{\partial t} \right) \\
& = [V_i^* \delta U_i]_0^T - \left(\frac{\partial V_i^*}{\partial t}, \delta U_i \right)
\end{aligned} \tag{2.65}$$

Term 2

$$\begin{aligned}
& \left(V_i^*, \frac{d}{d\epsilon} A_{ij} (U(z^* + \epsilon \delta z)) \frac{\partial U_j(z^* + \epsilon \delta z)}{\partial x} \right) \Big|_{\epsilon=0} \\
&= \left(V_i^*, \frac{\partial A_{ij}}{\partial U_k} \frac{d}{d\epsilon} U_j(z^* + \epsilon \delta z) \Big|_{\epsilon=0} \frac{\partial U_k}{\partial x} + A_{ij} (U(z^* + \epsilon \delta z)) \frac{\partial}{\partial x} \frac{dU_j}{d\epsilon} (z^* + \epsilon \delta z) \Big|_{\epsilon=0} \right) \\
&= \left(\frac{\partial A_{ij}}{\partial U_k} \frac{\partial U_k}{\partial x} V_i^*, \delta U_j \right) + \left(V_i^*, A_{ij} \frac{\partial \delta U_j}{\partial x} \right) \tag{2.66} \\
&= \left(\frac{\partial A_{ij}}{\partial U_k} \frac{\partial U_k}{\partial x} V_i^*, \delta U_j \right) + \frac{\partial}{\partial x} (A_{ij} V_i^*, \delta U_j) - \left(\frac{\partial A_{ij}}{\partial x} V_i^*, \delta U_j \right) - \left(A_{ij} \frac{\partial V_i^*}{\partial x}, \delta U_j \right) \\
&= \left(\left(\frac{\partial A_{ij}}{\partial U_k} \frac{\partial U_k}{\partial x} - \frac{\partial A_{ij}}{\partial x} \right) V_i^*, \delta U_j \right) + \frac{\partial}{\partial x} (A_{ij} V_i^*, \delta U_j) - \left(A_{ij} \frac{\partial V_i^*}{\partial x}, \delta U_j \right)
\end{aligned}$$

Term 3

$$\left(V_i^*, \frac{d}{d\epsilon} S_i (U(z^* + \epsilon \delta z)) \right) \Big|_{\epsilon=0} = \left(V_i^*, \frac{\partial S_i}{\partial U_j} \delta U_j \right) = \left(\frac{\partial S_i}{\partial U_j} V_i^*, \delta U_j \right) \tag{2.67}$$

The fourth term simply yields an inner product between the adjoint vector and δz . It will make things clearer to see the two boundary terms in isolation from the differential relations $[V^* \delta U]_0^T$ and $\frac{\partial}{\partial x} [(AV^*, \delta U)]$.

After integrating by parts all the terms in the last inner product, Equation 2.63 can be written, for hyperbolic PDEs with source terms, as [56]:

$$\begin{aligned}
& \left(\frac{\partial I}{\partial U}, \delta U(x, 0) \right) + \left(\frac{\partial K}{\partial U}, \delta U(x, T) \right) + [V^* \delta U]_0^T + \int_0^T \left(\frac{\partial L}{\partial U}, \delta U \right) + \left(\frac{\partial L}{\partial z}, \delta z \right) \\
& - \left(\frac{\partial V_i^*}{\partial t}, \delta U \right) + \left(\left(\frac{dA_{ij}}{dU_k} \frac{\partial U_k}{\partial x} - \frac{\partial A_{ij}}{\partial x} \right) V_i^*, \delta U_j \right) - \left(A_{ij} \frac{\partial V_i^*}{\partial x}, \delta U_j \right) - \left(\frac{dS_i}{dU_j} V_i^*, \delta U_j \right) - (V_i^*, \delta z_i) \\
& - \frac{\partial}{\partial x} [(A_{ij} V_i^*, \delta U_j)] \Big|_{x=x_L}^{x=x_R} dt + (L + (V^*, N(U^*, z^*))) \Big|_{t=T} \delta t = 0
\end{aligned} \tag{2.68}$$

Grouping the terms that multiply δU inside the integral gives the adjoint system of PDEs while grouping the terms multiplying δz gives the optimal control condition. Notice the first term in the second line multiplies δU_j not δU_i but since it is summed over in that term, any index suffice

such that it is legal to replace the indices with j so that all terms multiply the same component of δU . Grouping the like variations in δU at the initial and final times gives necessary condition on the optimal adjoint variables.

$$\begin{aligned} & \int_0^T \left(\frac{\partial L}{\partial z} - V^*, \delta z(x, t) \right) + \\ & \left(-\frac{\partial V_j^*}{\partial t} + \left(\frac{\partial A_{ij}}{\partial U_k} \frac{\partial U_k}{\partial x} - \frac{\partial A_{ij}}{\partial x} \right) V_i^* - A_{ij} \frac{\partial V_i^*}{\partial x} - \frac{\partial S_i}{\partial U_j} V_i^* + \frac{\partial L}{\partial U_j}, \delta U_j \right) + \\ & -\frac{\partial}{\partial x} [(A_{ij} V_i^*, \delta U_j)] \Big|_{x=x_L}^{x=x_R} + (L + (V^*, N(U^*, z^*))) \Big|_{t=T} \delta t = 0 \end{aligned} \quad (2.69)$$

$$\left(\frac{\partial I}{\partial U} - V^*(x, 0), \delta U(x, 0) \right) = 0 \quad (2.70)$$

$$\left(\frac{\partial K}{\partial U} + V^*(x, T), \delta U(x, T) \right) = 0 \quad (2.71)$$

Lastly, the final time may be free to vary. If so, a necessary condition for the final time must be constructed, known as the transversality condition. The variation of the state at the final time will have a first order term expanded in space $\delta U(x, T) = \delta U + \frac{\partial U(x, T)}{\partial t} \delta t$. Therefore, there is a change to the final time boundary condition.

$$\left(\delta U(x, T) + \frac{\partial U(x, T)}{\partial t} \delta t, \frac{\partial K}{\partial U} + V^* \right) = \left(\delta U, \frac{\partial K}{\partial U} + V^* \right) + \left(\delta t, \frac{\partial U}{\partial t} \left(\frac{\partial K}{\partial U} + V^* \right) \right) \quad (2.72)$$

The first term recovers the same result as for the fixed final time. The second term remains and is added to another contribution to the variation of the final time from the integrand of the augmented cost functional. This term arises as a result of Leibniz's rule for a derivative of an integral with a moving boundary. When the final time was fixed, the derivative with respect to ϵ could be brought inside the integral with no other consideration. Since the final time (the boundary of the time integral), is free to vary, Leibniz's rule dictates that the derivative can be brought inside the integral with the addition of boundary terms. For a general function of time f over the time dependent interval $[a(t), b(t)]$ this looks like:

$$\frac{d}{dt} \int_{a(t)}^{b(t)} f(t) dt = \int_{a(t)}^{b(t)} \frac{df}{dt} \cdot dt + f(b(t))\dot{b} - f(a(t))\dot{a} \quad (2.73)$$

In this problem, only the final time is free so $\dot{a} = 0$ and the analogous term at $b(t)$ is,

$$(L + (V, N(U, z)))|_{t=T} \delta t \quad (2.74)$$

Combining both terms that multiply δt gives the inner-product:

$$\left(\delta t, (L + (V^*, N(U, z)))|_{t=T} + \frac{\partial K}{\partial U} \frac{\partial U}{\partial t} + \left(V^*, \frac{\partial U}{\partial t} \right) \right) = 0 \quad (2.75)$$

Recall that $N \equiv 0$ meaning that term contributes nothing to the sum at any moment in time. The term involving K can be written as a total derivative in time.

$$\left(\delta t, \left(L + \left(V^*, \frac{\partial U}{\partial t} \right) \right) |_{t=T} + \frac{dK}{dt} \right) = 0 \quad (2.76)$$

The Hamiltonian is defined in general in Equation 2.77.

$$H = L + \left(V, \frac{\partial U}{\partial t} \right) \quad (2.77)$$

Using this definition, the Transversality Condition takes it's familiar form in Equation 2.78.

$$\left(\delta t, H|_{t=T^*} + \frac{dK}{dt} \right) = 0 \quad (2.78)$$

Equations (2.69)-(2.71) and (2.78) gives a set of first-order necessary conditions that an optimal system (z^*, U^*, V^*, T^*) must satisfy if it can be a candidate for a local minimizer of J constrained to $N(U, z)$, the general PDE system under a control action. Initial and boundary conditions are either specified or penalized. Formal sufficient conditions for optimality involve going to second-order however it will be obvious by the sequence of iterations of a solution procedure if J is being locally minimized or not.

2.3.2 Formulation of Single-Phase Optimal Control Shock Attenuation Problem

This single-phase control calculation is meant to give insight into a multi-phase control calculation where the initial water placement determines the degree of shock attenuation. As stated in the Introduction, several interaction mechanisms between the water droplets and the IOP wave are present and not fully understood. The dominant dissipative mechanism for the shocks of interest is the loss of energy of the gas through vaporization of the water droplets [7]. Experimental data from droplet-shock interaction in this regime shows that the other dissipative mechanisms e.g. drag on droplets, sensible heating of droplets etc. are less significant to IOP attenuation. In a multi-phase calculation, the control action would take the form of a liquid mass source and the effect of vaporization will take energy out of the gas phase. To most simply replicate the dominant dissipative mechanism with a single-phase calculation, the control will act as an energy sink distributed in space and time behind the moving shock front. No sinks or sources in the momentum or mass conservation equations is needed for this simplified formulation.

The cost functional in this context must reflect that a decrease in the maximum jump in pressure (the overpressure at the shock front) is most desirable. It should also penalize control action but to a lesser magnitude. Therefore, let J , the cost functional be defined in Equation 2.79.

$$J = \frac{a}{2} \int_0^T \int_{\Omega} z(x, t)^2 dx dt + \frac{b}{2} \int_{\Omega_s} (P(x, T) - Q(x))_+^2 dx \quad (2.79)$$

The final time T , is not fixed, $z(x, t)$ is the control action, $P(x, T)$ is the Pressure at the final time, $Q(x)$ is the desired final pressure and a and b are weighting constants. The larger b is compared to a , the more significant the final time penalty and the less the penalty for using control action. From the form of Equation 2.56, the individual cost functionals can be discerned. There is no free initial data and therefore no need to associate a cost to it, making $I \equiv 0$ for the single-phase formulation. The running cost $L(U, z)$ need only penalize control effort since the final time target state sufficiently describes the degree to which a controlled solution had a desirable outcome.

$$L(U, z) = \frac{a}{2} \int_{\Omega} z(x, t)^2 dx \quad (2.80)$$

$$K(U(\cdot, T)) = \frac{b}{2} \int_{\Omega_s} (P(x, T) - Q(x))_+^2 dx \quad (2.81)$$

The control action will take the form of an internal energy sink distributed in space and time behind the shock front. It only appears on the right hand side of the energy balance equation of the 1D Euler system.

$$U = (\rho(x, t), \rho u(x, t), \rho E(x, t))^T \quad (2.82)$$

$$\frac{\partial}{\partial t} \begin{pmatrix} \rho \\ \rho u \\ \rho E \end{pmatrix} + \frac{\partial}{\partial x} \begin{pmatrix} \rho u \\ \rho u^2 + P \\ u(\rho E + P) \end{pmatrix} = \begin{pmatrix} 0 \\ 0 \\ z(x, t) \end{pmatrix} \quad (2.83)$$

$$\rho E = \rho e + \frac{\rho u^2}{2} \quad (2.84)$$

$$P = \rho e (\gamma - 1) \quad (2.85)$$

Initial conditions are fixed as stationary, ambient air. Stating the density, velocity and pressure determines the internal and total energy and the conservative vector.

$$\begin{aligned}
\rho(x, 0) &= 1 \text{ kg/m}^3 \\
u(x, 0) &= 0 \text{ m/s} \\
P(x, 0) &= 10^5 \text{ Pa} \\
\rho u(x, 0) &= 0 \text{ kg/m}^2 \cdot \text{s} \\
\rho e(x, 0) &= 250000 \text{ J} \\
\rho E(x, 0) &= 250000 \text{ J}
\end{aligned} \tag{2.86}$$

Therefore, the initial variation in the state vector in Equation 2.70 is zero. In addition, there is no need for an initial penalty I in this formulation so the derivative $\frac{\partial I}{\partial U} = 0$ and $V(x, 0)$ is left undetermined.

Remark on applying the inlet boundary condition:

The inlet boundary condition is explicitly given by the IOP simulation data when the flow is supersonic. If the flow is subsonic, non-reflection of the $u - c$ characteristic is imposed [12]. In addition, the Monitor Point data was chosen where the flow was nearest to 1D; however, the 2D data did have transverse motion. The data will still give a plausible 1D blast wave with the inlet boundary condition set in this manner and the goal of the calculation, controlling a range of blast waves, can be achieved. At the outlet boundary the flow remains stationary because the final time will always be such that the shock wave will not have enough time to propagate though the entire domain and reach the outlet.

In order to determine the optimal control $z^*(x, t)$ that minimizes the cost functional J it is necessary to define the Hamiltonian of the system and derive necessary conditions using the Pontryagin Minimum Principle and the calculus of variations. Recalling Equation 2.77, the Hamiltonian for this system is given in Equation 2.87.

$$\begin{aligned}
H(U, V, z, t) &= L(U, z) + \int_{\Omega} V \cdot \frac{\partial U}{\partial t} dx \\
&= \int_{\Omega} \frac{a}{2} z^2 + V_1 \frac{\partial \rho}{\partial t} + V_2 \frac{\partial (\rho u)}{\partial t} + V_3 \frac{\partial (\rho E)}{\partial t} dx
\end{aligned} \tag{2.87}$$

The co-state or adjoint, vector is $(V_1, V_2, V_3)^T$. The flow dynamics will be solved in the conservative form of Equation 2.83, yet it is useful to write the system in the quasi-linear form of Equation 2.88 to derive the adjoint system. The conservative basis Jacobian matrix was given in Equation 2.7. Now the system has a control source vector in the energy balance equation.

$$\frac{\partial U_i}{\partial t} + A_{ij}(U) \frac{\partial U_j}{\partial x} = z_i \delta_{i3} \quad (2.88)$$

To derive necessary conditions as in the general case, the optimal state must be defined $(U^*(x, t), V^*(x, t), z^*(x, t), T^*)$ and the optimal control perturbed such that $z = z^* + \epsilon \delta z$ where $\epsilon > 0$ is a small constant. The variation in the control will cause variational terms in each of the other free variables of the system that must necessarily vanish at an optimal solution. To incorporate the constraints of the 1D Euler system using the Lagrange multiplier method, each conservation law is multiplied by an adjoint variable and added to J , resulting in the augmented cost functional \tilde{J} . Then from expanding \tilde{J} in a Taylor series the first order necessary condition will be:

$$\frac{d}{d\epsilon} \tilde{J}(z^* + \epsilon \delta z) |_{\epsilon=0} = 0 \quad (2.89)$$

Grouping the terms of like variational multipliers gives the optimal system. Integrating by parts until all derivatives are on the adjoint vector yields the following linear system of partial differential equations [11].

$$\frac{\partial V_j}{\partial t} + A_{ij} \frac{\partial V_i}{\partial x} + \left(\frac{\partial A_{ij}}{\partial x} - \frac{dA_{ij}}{dU_k} \cdot \frac{\partial U_k}{\partial x} \right) V_i + \frac{\partial}{\partial x} [(A_{ij} V_i^*, \delta U_j)] |_{\partial\Omega} = \frac{\partial L}{\partial U_i} = 0 \quad (2.90)$$

Non-trivial elements of the matrix $\frac{\partial A_{ij}}{\partial U_k} \cdot \frac{\partial U_k}{\partial x}$ are given in Equations 2.91-2.95.

$$\frac{\partial}{\partial U_k} A_{21} \cdot \frac{\partial U_k}{\partial x} = (\gamma - 3) \left(-\frac{u^2}{\rho} \frac{\partial \rho}{\partial x} + \frac{u}{\rho} \frac{\partial (\rho u)}{\partial x} \right) \quad (2.91)$$

$$\frac{\partial}{\partial U_k} A_{22} \cdot \frac{\partial U_k}{\partial x} = (\gamma - 3) \left(\frac{u}{\rho} \frac{\partial \rho}{\partial x} - \frac{1}{\rho} \frac{\partial (\rho u)}{\partial x} \right) \quad (2.92)$$

$$\frac{\partial}{\partial U_k} A_{31} \cdot \frac{\partial U_k}{\partial x} = \frac{u}{\rho} \left(2\gamma E - 3(\gamma - 1) u^2 \right) \frac{\partial \rho}{\partial x} + \frac{1}{\rho} \left(3(\gamma - 1) u^2 - \gamma E \right) \frac{\partial (\rho u)}{\partial x} - \gamma \frac{u}{\rho} \frac{\partial (\rho E)}{\partial x} \quad (2.93)$$

$$\frac{\partial}{\partial U_k} A_{32} \cdot \frac{\partial U_k}{\partial x} = \frac{1}{\rho} \left(3(\gamma - 1) u^2 - \gamma E \right) \frac{\partial \rho}{\partial x} - 3(\gamma - 1) \frac{u}{\rho} \frac{\partial (\rho u)}{\partial x} + \frac{\gamma}{\rho} \frac{\partial (\rho E)}{\partial x} \quad (2.94)$$

$$\frac{\partial}{\partial U_k} A_{33} \cdot \frac{\partial U_k}{\partial x} = -\frac{\gamma u}{\rho} \frac{\partial \rho}{\partial x} + \frac{\gamma}{\rho} \frac{\partial (\rho u)}{\partial x} \quad (2.95)$$

$\partial\Omega$ denotes the boundary of the spatial domain. The right hand side of Equation 2.90 is zero in this formulation because the running cost does not explicitly depend on the state vector.

Since the final state is not fixed, there is a necessary condition on the adjoint vector at the final time.

$$V_i^*(x, T^*) = \frac{\partial}{\partial U_i} K(U(x, T^*)) \quad (2.96)$$

Therefore, in *this* basis, all 3 derivatives are non-zero in Ω_s .

$$\begin{aligned}
V_1^*(x, T^*) &= b(P(x, T^*) - Q(x))_+ \cdot \frac{\partial P}{\partial \rho}(x, T^*) \\
&= b(P(x, T^*) - Q(x))_+ \cdot \frac{u(x, T^*)^2}{2} (\gamma - 1) \\
V_2^*(x, T^*) &= b(P(x, T^*) - Q(x))_+ \cdot \frac{\partial P}{\partial (\rho u)}(x, T^*) \\
&= -b(P(x, T^*) - Q(x))_+ \cdot u(x, T^*) (\gamma - 1) \\
V_3^*(x, T^*) &= b(P(x, T^*) - Q(x))_+ \cdot \frac{\partial P}{\partial (\rho E)}(x, T^*) \\
&= b(P(x, T^*) - Q(x))_+ \cdot (\gamma - 1)
\end{aligned} \tag{2.97}$$

For a free final time, the necessary condition for the optimal final time T^* is given by the Transversality condition. Define f as a functional to be used in the solution procedure.

$$\begin{aligned}
H(U^*(x, T^*), V^*(x, T^*), z^*(x, T^*), T^*) + \frac{d}{dt}K(U(x, T^*)) &= 0 \\
\int_{\Omega} \frac{a}{2} z(x, T^*)^2 + b(P(x, T^*) - Q(x)) &\left(\begin{array}{c} \frac{\partial P}{\partial \rho}(x, T^*) \frac{\partial \rho}{\partial t}(x, T^*) + \\ \frac{\partial P}{\partial \rho u}(x, T^*) \frac{\partial \rho u}{\partial t}(x, T^*) + \\ \frac{\partial P}{\partial \rho E}(x, T^*) \frac{\partial \rho E}{\partial t}(x, T^*) + \\ \frac{\partial P}{\partial t}(x, T^*) \end{array} \right) dx &= 0 \\
&\equiv f(T^*)
\end{aligned} \tag{2.98}$$

The necessary condition on the optimal control solution comes from maximizing the Hamilto-

nian for an unconstrained control. The unconstrained condition is justified because there is no restriction on control magnitude in regions where control is allowed. The integral is true over any domain Ω and at any moment in time it should be true point-wise for all $t \in [0, T]$.

$$\frac{\partial H}{\partial z}(U^*, V^*, z^*, t) = \int_{\Omega} az^*(x, t) + V_3^*(x, t)dx = 0 \quad (2.99)$$

Equations (2.82)-(2.86),(2.90),(2.97),(2.98) and (2.99) give the complete set of first order necessary conditions for the optimal system.

2.3.3 Formulation of Two-Phase Optimal Control Shock Attenuation Problem

In the two-phase system, the control action takes the form of the free initial data. The first state variable $\alpha_l(x, 0)$, the initial water volume fraction distribution, will solely determine the attenuation at the final time. This is a satisfying formulation as the alternative would involve water injection over time as the control. However, water cannot be significantly injected into a flow over the interaction time scales of a shock wave. The goal of attenuating the jump in gas pressure at the final time is unchanged, so the final time penalty need only adopt the two-phase notation. Equation 2.100 gives the cost functional for the two-phase system.

$$J = \int_{\Omega} \frac{a}{2} (\alpha_l(x, 0))^2 dx + \int_{\Omega_s} \frac{b}{2} (P_g(x, T) - Q(x))_+^2 dx \quad (2.100)$$

Note that there is no running penalty, thus $L \equiv 0$ in this formulation. It is then clear what the initial penalty and final time penalties are, shown in Equations 2.101 and 102 respectively.

$$I(\tilde{U}(\cdot, 0)) = \int_{\Omega} \frac{a}{2} (\alpha_l(x, 0))^2 dx \quad (2.101)$$

$$K(\tilde{U}(\cdot, T)) = \int_{\Omega_s} \frac{b}{2} (P_g(x, T) - Q(x))_+^2 dx \quad (2.102)$$

The multiphase system can be defined in the primitive basis recalled from Equation 2.32.

$$\tilde{U} = (\alpha_g, \rho_g, u_g, P_g, \rho_l, u_l, P_l)^T \quad (2.103)$$

The state dynamics are of the form of Equation 2.34 with the Jacobian matrix defined in Equation 2.33. The adjoint system has the form of Equation 2.69. Note the inclusion of the term $\frac{\partial S_i}{\partial U_j}$ present in the two-phase system but not the single-phase system. This term as well as other non-trivial closed form elements of the matrices of the adjoint system are given in Appendix A and B for brevity. In the primitive basis, the density, velocity and pressure of the gas and liquid have fixed initial conditions which are stationary ambient atmosphere at sea level.

$$\begin{aligned} \rho_g(x, 0) &= 1 \text{ kg/m}^3 & \rho_l(x, 0) &= 10^3 \text{ kg/m}^3 \\ u_g(x, 0) &= 0 \text{ m/s} & u_l(x, 0) &= 0 \text{ m/s} \\ P_g(x, 0) &= 10^5 \text{ Pa} & P_l(x, 0) &= 10^5 \text{ Pa} \end{aligned} \quad (2.104)$$

The first variable, the liquid volume fraction, is not fixed at the initial time and acts as the control. The initial cost functional I is then associated with a penalty to the amount of water used.

Looking back to Equation 2.70 and combining Equation 2.101 and 2.105 gives Equation 2.106.

$$\delta \tilde{U}_i(x, 0) = \begin{cases} 0 & i \neq 1 \\ \neq 0 & i = 1 \end{cases} \quad (2.105)$$

$$\left(\frac{\partial I}{\partial \tilde{U}_i}, \delta \tilde{U}_i(x, 0) \right) = \left(\frac{\partial I}{\partial \alpha_g}, \delta \alpha_g(x, 0) \right) \quad (2.106)$$

After dropping the factor of $\delta \alpha_g(x, 0)$ the first order necessary optimal condition on $V_1^*(x, 0)$ is given in Equation 106.

$$\int_{\Omega} a(1 - \alpha_g(x, 0)) - V_1^*(x, 0) dx = 0 \quad (2.107)$$

Since this is true over a general domain Ω it must be true point-wise.

At the final time T , our cost functional K will penalize the gas pressure profile in space if the

overpressure at the shock front is greater than that of a predefined target state. K is only an explicit function of the fourth state variable \tilde{U}_4 , the gas pressure. The rest of the state variables are free to vary and their variation does not vanish at the final time.

$$\delta\tilde{U}_i(x, T) = \begin{cases} 0 & i \neq 4 \\ \neq 0 & i = 4 \end{cases} \quad (2.108)$$

Using the condition in Equation 2.71 with the definitions in Equations 2.102, 2.108 and 2.109 gives final time necessary condition in Equation 2.110.

$$\left(\frac{\partial K}{\partial \tilde{U}_i}, \delta\tilde{U}_i(x, T) \right) = \left(\frac{\partial K}{\partial P_g}, \delta P_g(x, T) \right) \quad (2.109)$$

Therefore, as before, the final time optimal condition on $V_4^*(x, T)$ becomes Equation 2.110:

$$\left(\frac{\partial K}{\partial P_g} + V_4^*(x, T), \delta\tilde{U}_4(x, T) \right) = 0 \quad (2.110)$$

where $Q(x)$ is the predefined target state and b is a constant. The optimal condition then becomes Equation 2.111:

$$\int_{\Omega} b (P_g(x, T) - Q(x)) + V_4^*(x, T) dx = 0 \quad (2.111)$$

which must also be true point-wise.

The purpose of the calculation is to optimize blast wave attenuation. To that end, let the forcing function or blast wave condition at a stationary point over time be the left boundary condition $u_L(t)$ with a right-ward traveling blast wave. The flow conditions are supersonic and may be considered fixed unless reflected shock waves originating from within the simulation domain must propagate outward in a non-reflection characteristic boundary condition. The spatial boundary term from Equation 2.69 for a linear interval $x \in [x_L, x_R] = \Omega$ is simplified in Equation 2.112.

$$\begin{aligned}
\frac{\partial}{\partial x} \left[(AV^*, \delta\tilde{U}) \right] &= \frac{\partial}{\partial x} \int_{\Omega} AV^* \cdot \delta\tilde{U} dx = \int_{x=x_L}^{x=x_R} \frac{\partial}{\partial x} (AV^* \cdot \delta\tilde{U}) dx = \left[AV^* \cdot \delta\tilde{U} \right]_{x=x_L}^{x=x_R} \\
&= A \left(\tilde{U}_R \right) V_R^* \cdot \delta\tilde{U}_R - A \left(\tilde{U}_L \right) V_L^* \cdot \delta\tilde{U}_L \\
&= A \left(\tilde{U}(x_R, t) \right) V^*(x_R, t) \cdot \delta\tilde{U}(x_R, t) - A \left(\tilde{U}(x_L, t) \right) V^*(x_L, t) \cdot \delta\tilde{U}(x_L, t)
\end{aligned} \tag{2.112}$$

The calculation can be performed in such a way that, after starting with no motion in the initial conditions, the blast wave can be simulated as entering at the left boundary, moving right-ward, and not reaching the right boundary by the final time. In such a simulation there is no change to the state vector at the right boundary for all time.

$$\delta\tilde{U}(x, t) = \begin{cases} 0 & x = x_R \\ 0 & x = x_L \quad \text{supersonic inflow} \\ \neq 0 & x = x_L \quad \text{subsonic inflow} \end{cases} \tag{2.113}$$

From Equation 2.112, the boundary integral from Equation 2.111 reduces to:

$$= A_{i1} V_i \cdot \delta\alpha_g(x_L, t) \tag{2.114}$$

Equation 2.28 gives the necessary condition for the optimal final time T^* .

$$\begin{aligned}
H|_{t=T^*} + \frac{dK}{dt} &= 0 \\
&= L|_{t=T^*} + \left(V^*(x, T^*) \cdot \frac{\partial \tilde{U}^*}{\partial t} \right) + \frac{\partial K}{\partial \tilde{U}} \frac{\partial \tilde{U}}{\partial t} \\
&= \int_{\Omega} V_4^*(x, T^*) \frac{\partial P_g(x, T^*)}{\partial t} + b \left(P_g^*(x, T^*) - Q(x) \right) \frac{\partial P_g(x, T^*)}{\partial t} dx \\
&= 2b \int_{\Omega} \left(P_g^*(x, T^*) - Q(x) \right) \frac{\partial P_g(x, T^*)}{\partial t} dx \\
&= \int_{\Omega} \left(P_g^*(x, T^*) - Q(x) \right) \frac{\partial P_g(x, T^*)}{\partial t} dx
\end{aligned} \tag{2.115}$$

Because we have all the control effort taking place at the initial time, through the initial data, there is no need for control over time. So, $z^*(x, t) = 0$ and since it is fixed, the variation $\delta z_i(x, t)$ vanishes as well.

The final time penalty K can completely communicate the objective of overpressure attenuation without the need for a penalty over space and time L for matching a target over space and time. All of this means that $L(U, z) = 0$ and consequently, the first two inner products inside the time integral in Equation 2.68 are also zero. The complete set of first order necessary conditions for the two-phase optimal system is given by Equations 2.103-2.104, 2.107, 2.111, 2.115 given the state dynamics of Equation 2.34 and corresponding adjoint PDE from Equation 2.69. The closed form matrix elements for the adjoint PDE are stated in Appendices A and B.

THIS PAGE INTENTIONALLY LEFT BLANK

CHAPTER 3:

Numerical Methods

3.1 Computational Fluid Dynamics for Unsteady Compressible Flow

3.1.1 Exact Solution to the Riemann Problem

This section describes a numerical method [40], [57] used for calculating the exact solution to the Riemann Problem (Equation 2.16) for the Unsteady Euler Equations of gas dynamics (Equations 2.1-2.5). The method takes advantage of the knowledge of the wave patterns shown in Figures 2.1 and 2.2. The subscripts L and R refer to the left and right initial data and constant states to the left $\tilde{U}_L = (\rho_L, u_L, p_L)$ and right $\tilde{U}_R = (\rho_R, u_R, p_R)$ of the star region respectively. Originating from $x = 0$ at an initial moment in time, a rarefaction wave moves to the left at speed $u - c$, a contact discontinuity moves to the right at a speed u and a shock wave moves to the right at a speed $u + c$. The speed of sound changes across the star region making it locally determined. The exact solution is constructed by sampling the flow at any moment in time $t > 0$ on a discrete grid and iteratively solving Equation 3.1 using knowledge of the sample points' location in relation to the wave pattern and given the definitions in Equations 3.2-3.4 previously stated in Chapter 2.

$$f(p^*, \tilde{U}_L, \tilde{U}_R) = f_L(p, \tilde{U}_L) + f_R(p, \tilde{U}_R) + \tilde{U}_R - \tilde{U}_L \quad (3.1)$$

$$f_L(p^*, \tilde{U}_L) = \begin{cases} (p - p_L) \left(\frac{A_L}{p + B_L} \right)^{1/2} & p > p_L \text{ shock} \\ \frac{2c_L}{\gamma - 1} \left(\left(\frac{p}{p_L} \right)^{\frac{\gamma-1}{2\gamma}} - 1 \right) & p \leq p_L \text{ rarefaction} \end{cases} \quad (3.2)$$

$$f_R(p^*, \tilde{U}_R) = \begin{cases} (p - p_R) \left(\frac{A_R}{p + B_R} \right)^{1/2} & p > p_R \text{ shock} \\ \frac{2c_R}{\gamma - 1} \left(\left(\frac{p}{p_R} \right)^{\frac{\gamma-1}{2\gamma}} - 1 \right) & p \leq p_R \text{ rarefaction} \end{cases} \quad (3.3)$$

$$\begin{aligned}
A_L &= \frac{2}{(\gamma+1)\rho_L} \\
A_R &= \frac{2}{(\gamma+1)\rho_R} \\
B_L &= \frac{(\gamma-1)}{(\gamma+1)}p_L \\
B_R &= \frac{(\gamma-1)}{(\gamma+1)}p_R
\end{aligned} \tag{3.4}$$

For each discrete sample point, the process starts with an initial guess for the pressure p^* . Next, the value of $f(p^*, \tilde{U}_L, \tilde{U}_R)$ is determined based on the known wave patterns. The velocity u^* is updated according to Equation 3.5 or 3.6 depending on the part of the star region the sampling point is located.

$$u_L^* = u_L - f_L(p^*, U_L) \tag{3.5}$$

$$u_R^* = u_R + f_R(p^*, U_R) \tag{3.6}$$

Next, update ρ^* according to Equation 3.7 or 3.8.

$$\rho_L^* = \rho_L \left(\frac{p^*}{P_L} \right)^{1/\gamma} \tag{3.7}$$

$$\rho_R^* = \rho_R \left(\frac{u_R - S}{u^* - S} \right) \tag{3.8}$$

The shock speed in a stationary frame is denoted as S . This solution method is impractical since many iterations are required to solve for the root of Equation 3.1 for each discrete point in space at each instant in time. The exact solution is shown in red in Figure 3.1.

3.1.2 Godunov Method with an Approximate Riemann Solver

The first-order Godunov Method [58] assumes a piece-wise constant solution in each discrete cell volume. The Riemann Problem is then solved locally between each cell at each moment in time based on the previous piece-wise solution. This approximate scheme does not require

an iterative solution and therefore is much less computationally demanding. With the choice of a conservative method, the errors introduced by the approximate solution behave in a known and acceptable way [59]-[64]. Figure 3.1 compares approximate numerical solutions of the shock tube problem to the exact solution, four-tenths of a millisecond in time after the diaphragm bursts. The finite difference, Modified MacCormick method [65] introduces dispersive error while the conservative Godunov method introduces dissipative error. The dispersive error causes the wrong jump condition and therefore the wrong entropy solution, shock speed and position as shown in Figure 3.1. Similar results exist in the literature [66]. More oscillations in the solution will also cause more problems when equilibrating with another phase. On the other hand, dissipative errors are second order in spatial derivatives of U and therefore, are a viscous-like error. It is well established that in the limit of vanishing viscosity the correct shock solution is achieved. From a physical point of view, a truly inviscid flow is being modeled.

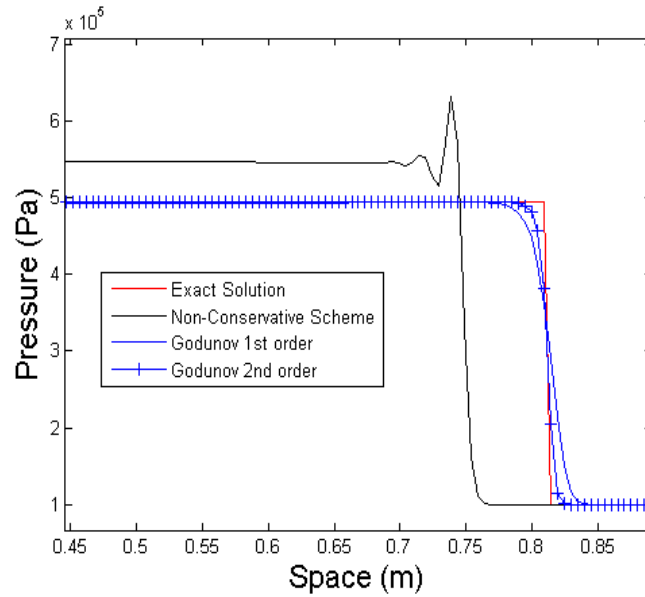


Figure 3.1: Comparison of numerical solutions to the Riemann problem .4 ms after diaphragm burst in shock tube flow. The initial pressure ratio was 10:1 in each case with a discontinuity at $x = .5m$

Let the spatial domain $x \in [x_L, x_R] = \Omega$ be divided into M intervals each equally spaced by $\Delta x = (x_R - x_L) / M$. The locations of the discrete grid points are given in Equation 3.9, for $j=1, \dots, M+1$.

$$x_j = (j - 1)\Delta x \quad (3.9)$$

The solution will be piece-wise constant between half-cells. As a sensible choice for limits of integration, the half-cell locations are define in Equation 3.10, for $j = 1, \dots, M$.

$$x_{j-1/2} = (j - 1/2)\Delta x \quad (3.10)$$

For all cell volumes let the limits of integration be $x_1 = x_{j-1/2}$ and $x_2 = x_{j+1/2}$. Let the time domain $[0, T]$ be divided into N intervals each with size $\Delta t = T/N$. The moments in time are given in Equation 3.11 for $n = 1, \dots, N$.

$$t^n = (n - 1)\Delta t \quad (3.11)$$

For all regions of the discrete space-time domain $[x_{j-1/2}, x_{j+1/2}] \times [t^n, t^{n+1}]$ the conservation law in Equation 2.21 becomes Equation 3.13 without approximation.

$$\int_{x_{j-1/2}}^{x_{j+1/2}} U(x, t^{n+1}) dx = \int_{x_{j-1/2}}^{x_{j+1/2}} U(x, t^n) dx + \int_{t_1}^{t_2} F(U(x_{j-1/2}, t)) dt - \int_{t_1}^{t_2} F(U(x_{j+1/2}, t)) dt \quad (3.12)$$

Discrete approximations to the solution at two discrete moments in time are defined in Equation 3.13 and 3.14.

$$U_i^n \approx \frac{1}{\Delta x} \int_{x_{j-1/2}}^{x_{j+1/2}} \bar{U}(x, t^n) dx \quad (3.13)$$

$$U_i^{n+1} \approx \frac{1}{\Delta x} \int_{x_{j-1/2}}^{x_{j+1/2}} \bar{U}(x, t^{n+1}) dx \quad (3.14)$$

The cell average of the conservative vector is denoted as $\bar{U}(x, t)$. Locally in each cell, U is constant when traveling at the estimated wave speeds. This is a valid assumption as long as

the time step is sufficiently small such that no wave is propagated beyond the cell from where the speed was estimated to avoid wave interaction which causes inaccuracy. This leads to the famous CFL condition given in Equation 3.15.

$$\Delta t \leq \frac{\Delta x}{S} \quad (3.15)$$

This time interval is limited by the maximum wave speed in each cell S . For $t \in [t^n, t^n + \Delta t]$ the discrete inter-cell solution and flux are given in Equations 3.16 and 3.17.

$$U_{j-1/2} = U(x_{j-1/2}, t^n) \quad (3.16)$$

$$F_{j-1/2} = F(U(x_{j-1/2}, t^n)) \quad (3.17)$$

With the discretizations of Equation 3.13, 3.14, 3.16 and 3.17 and the CFL condition on Δt , the integral form of the conservation law in Equation 3.12 gives the numeric form of Godunov's Method in Equation 3.18.

$$U_j^{n+1} = U_j^n - \frac{\Delta t}{\Delta x} (F_{j+1/2} - F_{j-1/2}) \quad (3.18)$$

A suitable, conservative approximation to the inter-cell flux $F_{j+1/2}$ will result exclusively in dissipative, not dispersive, numerical error near the shock front. As described earlier, these attributes are necessary for accurate jump conditions at the shock. In the limit of vanishing viscosity they converge to the correct weak solution. The Rusanov approximation used for the inter-cell flux [40], [54] is given in Equation 3.19.

$$F_{j+1/2} = \frac{1}{2} (F(U_j) + F(U_{j+1})) - S_j (U_{j+1} - U_j) \quad (3.19)$$

The maximum wave speed in the j^{th} cell is S_j . For a shock this is given by the Rankine-Hugoniot jump condition in Equation 2.13 of Chapter 2.

3.1.3 Second Order Godunov Method

A conservative second order extension to the Godunov method [67]-[70] was implemented to solve the compressible flow dynamics in 1D under a distributed control action. This method assumes that the solution in each cell is piece-wise linear and projects an intermediate solution on a non-uniform grid based on the maximum characteristic speeds from the interpolated solutions at each cell interface. Figure 3.2 is a diagram of what the uniform and non-uniform grids might look like, based on the wave speed estimates at the inter-cell boundary.

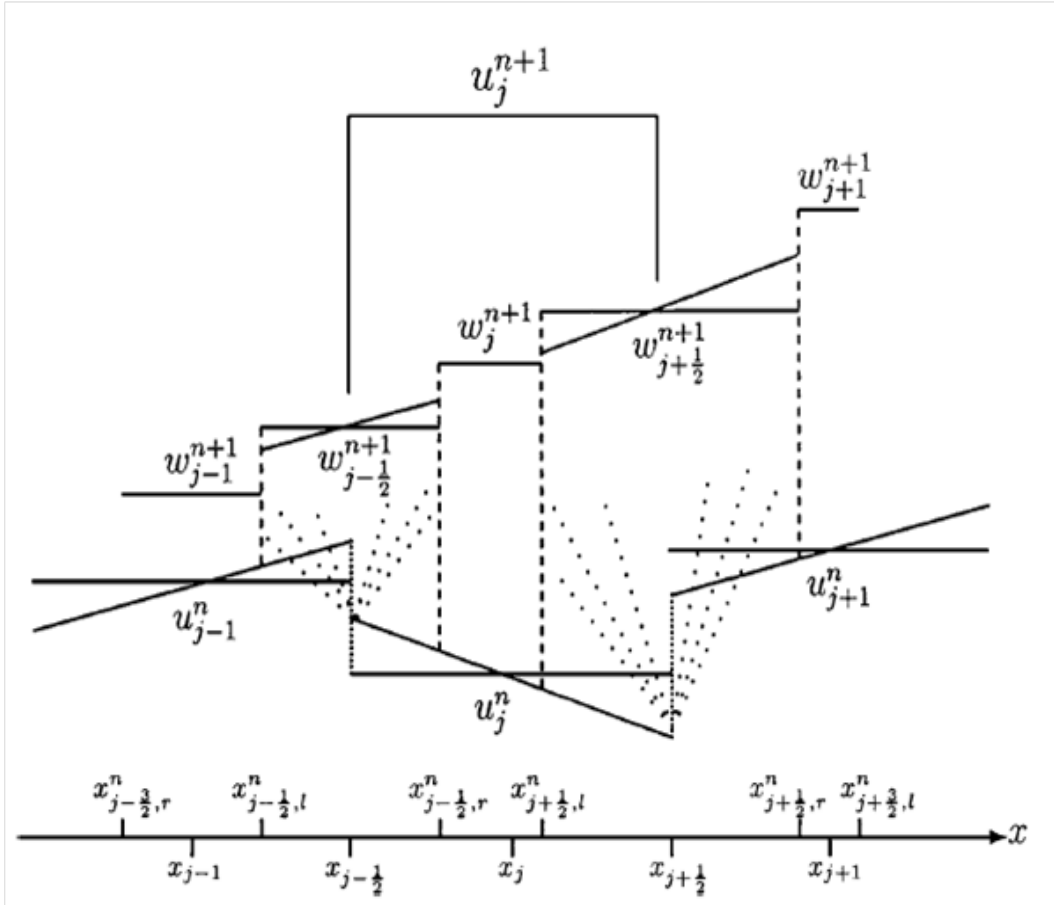


Figure 3.2: Intermediate non-uniform grid, Kurganov and Tadmor [67]

The familiar Godunov integration on the uniform grid is then second order accurate because of the intermediate finer grid. This numeric method was chosen because it preserves the conservative property with only dissipative error and can be adapted to the solution of a 1D multiphase calculation as presented in Saurel and Abgrall [31]. The essential numerical steps are summa-

rized here.

At a current time step t^n the solution vector U_j^n is known for all x_j . The local spatial derivative of the solution vector $(U_x)^n$ can be calculated by:

$$(U_x)_j^n = \text{minmod} \left(\frac{U_j^n - U_{j-1}^n}{\Delta x}, \frac{U_{j+1}^n - U_j^n}{\Delta x} \right) \quad (3.20)$$

The minmod function provides an upwind/downwind switch based on the wave direction of motion.

$$\text{minmod}(a, b) = \frac{1}{2} (\text{sign}(a) + \text{sign}(b)) \cdot \min(|a|, |b|) \quad (3.21)$$

The strategy is to first create a finer, intermediate grid to calculate the solution $w_j^{n+1/2}, w_{j+1/2}^{n+1/2}$ at a half time step forward in time with a conservative Godunov method. The second stage is to calculate the solution U_j^{n+1} at the next time step on the coarser, uniform grid with a conservative Godunov method. The result is that spatial resolution at the shock front more accurately captures the shock front discontinuity while maintaining a conservative second order dissipative error shape. Other methods can introduce dispersion, losing the conservative property and consequently will have oscillations near the shock front which give the wrong jump conditions.

The upper bound on the maximum wave speed at the inter cell boundary as estimated with a first order Taylor expansion of u_j^n .

$$a_{j+1/2}^n = \max \left(\text{eig} \left(A \left(U_{j+1/2}^- \right) \right), \text{eig} \left(A \left(U_{j+1/2}^+ \right) \right) \right) \quad (3.22)$$

$$U_{j+1/2}^+ = U_{j+1}^n - \frac{\Delta x}{2} (U_x)_{j+1}^n \quad (3.23)$$

$$U_{j+1/2}^- = U_{j+1}^n + \frac{\Delta x}{2} (U_x)_j^n \quad (3.24)$$

The superscripts $^+$ and $^-$ refer to the solution to the right and left of the inter-cell discontinuity. The eigenvalues of A are the eigenvalues of $\frac{\partial F}{\partial U}$, the characteristic wave speed es-

timated at the inter-cell boundaries. For the single-phase Euler system the eigenvalues are $(u_g, u_g + c_g, u_g - c_g)$ and for the two-phase system are $(V_i, u_g, u_g - c_g, u_g + c_g, u_l, u_l - c_l, u_l + c_l)$.

The finer, non-uniform intermediate grid is defined by using the bound on the maximum wave speed at each inter cell boundary.

$$x_{j+1/2,l}^n = x_{j+1/2}^n - a_{j+1/2}^n \cdot \Delta t \quad (3.25)$$

$$x_{j+1/2,r}^n = x_{j+1/2}^n + a_{j+1/2}^n \cdot \Delta t \quad (3.26)$$

The solution on the non-uniform grid is given in Equations 3.27 and 3.28.

$$\begin{aligned} w_{j+1/2}^n = & \frac{U_j^n + U_{j+1}^n}{2} + \frac{\Delta x - a_{j+1/2}^n \Delta t}{4} \left((U_x)_j^n (U_x)_{j+1}^n \right) \\ & - \frac{1}{2a_{j+1/2}^n} \left[F(U_{j+1/2,r}^{n+1/2}) - F(U_{j+1/2,l}^{n+1/2}) \right] \end{aligned} \quad (3.27)$$

$$\begin{aligned} w_j^n = & U_j^n + \frac{\Delta t}{2} (a_{j-1/2}^n - a_{j+1/2}^n) (U_x)_j^n \\ & - \frac{\Delta t / \Delta x}{1 - \Delta t / \Delta x (a_{j-1/2}^n + a_{j+1/2}^n)} \left[F(U_{j+1/2,l}^{n+1/2}) - F(U_{j+1/2,r}^{n+1/2}) \right] \end{aligned} \quad (3.28)$$

Quantities on the uniform grid at the inter-cell boundaries are approximated at the current time step in Equation 3.29 and 3.30 and at the half-time step in Equations 3.31 and 3.32.

$$U_{j+1/2,l}^n = U_j^n + \Delta x (U_x)_j^n \left(\frac{1}{2} - \frac{\Delta t}{\Delta x} a_{j+1/2}^n \right) \quad (3.29)$$

$$U_{j+1/2,r}^n = U_{j+1}^n + \Delta x (U_x)_{j+1}^n \left(\frac{1}{2} - \frac{\Delta t}{\Delta x} a_{j+1/2}^n \right) \quad (3.30)$$

$$U_{j+1/2,l}^{n+1/2} = U_{j+1/2,l}^n - \frac{\Delta t}{2} F(U_{j+1/2,l}^n)_x \quad (3.31)$$

$$U_{j+1/2,r}^{n+1/2} = U_{j+1/2,r}^n - \frac{\Delta t}{2} F \left(U_{j+1/2,r}^n \right)_x \quad (3.32)$$

The solution is progressed to t^{n+1} on uniform grid with a conservative second order update as shown in Equation 3.33 and using the definition in Equation 3.34.

$$U_j^{n+1} = \frac{\Delta t}{\Delta x} a_{j-1/2}^n w_{j-1/2}^{n+1} + \left(1 - \frac{\Delta t}{\Delta x} \left(a_{j-1/2}^n + a_{j+1/2}^n \right) \right) w_j^{n+1} + \frac{\Delta t}{\Delta x} a_{j+1/2}^n w_{j+1/2}^{n+1} + \frac{\Delta x}{2} \left(\left(\frac{\Delta t}{\Delta x} a_{j-1/2}^n \right)^2 (U_x)_{j-1/2}^{n+1} - \left(\frac{\Delta t}{\Delta x} a_{j+1/2}^n \right)^2 (U_x)_{j+1/2}^{n+1} \right) \quad (3.33)$$

$$(U_x)_{j+1/2}^{n+1} = \frac{2}{\Delta x} \minmod \left(\frac{w_{j+1}^{n+1} - w_{j+1/2}^{n+1}}{1 + \frac{\Delta t}{\Delta x} \left(a_{j+1/2}^n - a_{j+3/2}^n \right)}, \frac{w_{j+1/2}^{n+1} - w_j^{n+1}}{1 + \frac{\Delta t}{\Delta x} \left(a_{j+1/2}^n - a_{j+3/2}^n \right)} \right) \quad (3.34)$$

3.2 Method of Solution for Two-Phase, Gas-Liquid Coupling

The two-phase balance equations from Equations 2.22-2.24, the point-wise relations given in Equations 2.25-2.28, the interface quantities defined in Equations 2.29-2.31 and source terms defined in Equations 2.35 of Chapter 2 are the basis for the overarching numeric method used to couple the two-phase system based on the model from Saurel and Abgrall [31]. A survey of the literature on numeric methods for two-phase flow [71]-[76] reinforces the advantages of this method and the theory on which it is based.

3.2.1 Hyperbolic Operator

As was stated in Chapter 2, both phases are compressible, which produces seven distinct wave speeds in the system. Equations 2.23-2.24 can then be factorized into a hyperbolic PDE with a source term $H(U)$ from the motion of the interface and three separate ODEs for the separate components of the non-conservative source term $S(U)$ [31].

$$L_h : \frac{\partial U}{\partial t} + F(U)_x = H(U) \frac{\partial \alpha_g}{\partial x} \quad (3.35)$$

$$L_s : \frac{\partial U}{\partial t} = S(U) \quad (3.36)$$

$$L_s \equiv L_{MH} \cdot L_{VR} \cdot L_{PR} \quad (3.37)$$

When the first-order Godunov scheme is used, factorization of the two-phase model occurs according to Equation 3.39.

$$U^{n+1} = L_s^{\Delta t} L_h^{\Delta t} U^n \quad (3.38)$$

When the second-order Godunov scheme is used, factorization of the two-phase model occurs according to Equation 3.40 [76].

$$U^{n+1} = L_s^{\Delta t/2} L_h^{\Delta t} L_s^{\Delta t/2} U^n \quad (3.39)$$

The ability of an approximate numeric method to capture the shock discontinuity is based on the approximate Riemann fluxes at the inter-cell boundary. The method gives a few choices for conservative approximate Riemann fluxes. Equation 3.41 is the analogous Godunov update in Equation 3.18 for the two-phase system with a first-order Rusanov flux used to update the mass, momentum and energy of the gas and liquid phases.

$$U_i^{n+1} = U_i^n - \frac{\Delta t}{\Delta x} (F_{i+1/2}^n - F_{i-1/2}^n) + \Delta t H(U_i^n) \frac{\partial \alpha_{g,i}}{\partial x} \quad (3.40)$$

$$F_{i+1/2} = F(U_i, U_{i+1}) = \frac{1}{2} (F_i + F_{i+1} - S(U_{i+1} - U_i)) \quad (3.41)$$

$$\frac{\partial \alpha_{g,i}}{\partial x} = \frac{\alpha_{g,i+1} - \alpha_{g,i-1}}{2 \cdot \Delta x} \quad (3.42)$$

$$\alpha_{g,i}^{n+1} = \alpha_{g,i}^n - \frac{\Delta t}{2 \cdot \Delta x} [V_{i,i}^n (\alpha_{g,i+1}^n - \alpha_{g,i}^n) + S_{i-1/2} (\alpha_{g,i}^n - \alpha_{g,i-1}^n)] \quad (3.43)$$

The Godunov method for the two-phase system in Equation 3.41 can be extended to second order in an analogous way as that described in Section 3.1.3.

3.2.2 Source Term Operators

Next comes handling of the source terms. They can be factored into three separate terms based on timescale or phenomenon and solved sequentially as three separate ODEs after the hyperbolic Godunov solution. First the pressure relaxation operator in Equation 3.38 is isolated and the solution is given in Equation 3.44 where U^n is the solution vector after the Godunov integration.

$$U^{PR} = U^n + L_{PR}(U^n) \quad (3.44)$$

This ODE simplifies to Equation 2.41 and 2.42 which are recalled below.

$$(\alpha_g \rho_g E_g)^{PR} - (\alpha_g \rho_g E_g)^0 = \int_{\alpha_g^0}^{\alpha_g^{PR}} P_i d\alpha_g \quad (3.45)$$

$$(\alpha_l \rho_l E_l)^{PR} - (\alpha_l \rho_l E_l)^0 = - \int_{\alpha_g^0}^{\alpha_g^{PR}} P_i d\alpha_g \quad (3.46)$$

Internal energy is adjusting in each phase due to the work done by interfacial pressure. The goal is to calculate α_g^{PR} such that the pressures are equilibrated $P_g = P_l$ for all x_i while also satisfying the integral constraints in Equations 3.45 and 3.46. A solution procedure used in [31] is summarized here.

1. Make an initial guess for α_g^{PR} based on the difference $P_g - P_l$
2. Compute $(\alpha_g, \rho_g, E_g)^{PR}$ and $(\alpha_l, \rho_l, E_l)^{PR}$ from the integrals in Equations 3.46 and 3.47
3. During relaxation, total mass (α_g, ρ_g) is constant so a new iterate of ρ_g can be computed and then E_g and e_g as well. The procedure for liquid is identical.
4. Calculate P_g and P_l from the equations of state
5. Repeat until equilibrium condition $P_g = P_l$ is reached for all x_i

The velocity relaxation, or drag, operator taking the form of Equation 3.47 is next solved numerically.

$$U^{VR} = U^{PR} + L_{VR}(U^{PR}) \quad (3.47)$$

The drag force is based on the empirical drag law for spherical objects as given in Equation 2.43 and shown in discrete form in Equation 3.48.

$$F_d(x_i, t^n) = C_d \rho_g(x_i, t^n) D_p^2(x_i, t^n) \alpha_l(x_i, t^n) (u_g(x_i, t^n) - u_l(x_i, t^n))^2 \quad (3.48)$$

With the drag force on the droplet known, the solution to the ODE is straightforward, as shown in Equation 3.49.

$$\begin{aligned} u_g(x_i, t^{n+1}) &= u_g(x_i, t^n) + \frac{\Delta t}{\alpha_g(x_i, t^n) \rho_g(x_i, t^n)} F_d(x_i, t^n) \\ u_l(x_i, t^{n+1}) &= u_l(x_i, t^n) - \frac{\Delta t}{\alpha_l(x_i, t^n) \rho_l(x_i, t^n)} F_d(x_i, t^n) \\ E_g(x_i, t^{n+1}) &= E_g(x_i, t^n) + \frac{\Delta t}{\alpha_g(x_i, t^n) \rho_g(x_i, t^n)} F_d(x_i, t^n) V_i(x_i, t^n) \\ E_l(x_i, t^{n+1}) &= E_l(x_i, t^n) - \frac{\Delta t}{\alpha_l(x_i, t^n) \rho_l(x_i, t^n)} F_d(x_i, t^n) V_i(x_i, t^n) \\ e_g(x_i, t^{n+1}) &= e_g(x_i, t^n) + \frac{1}{2} u_g(x_i, t^{n+1})^2 \\ e_l(x_i, t^{n+1}) &= e_l(x_i, t^n) - \frac{1}{2} u_l(x_i, t^{n+1})^2 \end{aligned} \quad (3.49)$$

The third and final source vector left is due to the mass and heat exchange of the phases due to vaporization and interface heat transfer.

$$U^{n+1} = U^{MH} = U^{VR} + L_{MH}(U^{VR}) \quad (3.50)$$

Vaporization dynamics of the droplets is given by the Empirical-Beta Vaporization Law with experimental constants given [7]. The present calculation assumes that droplets are mono-dispersed and spherical. Their initial size is denoted $D_p^0(x_i, 0)$. When surrounded by hot gas, the droplets will start to vaporize and their diameter will evolve according to Equations 3.51 and 3.52.

$$\frac{\partial D_p^2}{\partial t}(x_i, t^{n+1}) = -\beta(T_g(x_i, t^n)) \quad (3.51)$$

$$\beta(T_g(x_i, t^n)) = 7600 \left(1 + 7.4 \cdot 10^{-7} (T_g(x_i, t^n) - 300K)_+\right)^{2.7548} \mu m^2/s \quad (3.52)$$

Once the new size of the droplets is known, the added amount of gas volume fraction is known.

$$\alpha_g^{n+1} = \alpha_g^n + \frac{4}{3}\pi \left(\frac{D_p^{n+1}{}^3}{2} - \frac{D_p^n{}^3}{2} \right) N_p^n \quad (3.53)$$

The critical quantity for sinking energy from the gas via vaporization is \dot{m} which is given in discrete form below based on Equation 2.44.

$$\dot{m}(x_i, t^{n+1}) = \rho_{H_2Ov}(P_g(x_i, t^{n+1})/atm) \left(\alpha_g(x_i, t^{n+1}) - \alpha_g(x_i, t^n) \right) \quad (3.54)$$

The density of water vapor changes an order of magnitude in the pressure range of 1-10 atm. It is calculated based on a quadratic fit to steam table data [42].

$$\rho_{H_2Ov}(P_g/atm)(x_i, t^{n+1}) = -.0024344 \cdot \frac{P_g(x_i, t^{n+1})^2}{atm} + .5368 \cdot \frac{P_g(x_i, t^{n+1})}{atm} - .077246 \quad kg/m^3 \quad (3.55)$$

With the additional mass of water vapor in the gas phase, the gas density will increase according to Equation 3.56 while the density of liquid water does not change.

$$\rho_g^{n+1} = (\alpha_g^n \rho_g^n + \dot{m}) / \alpha_g^{n+1} \quad (3.56)$$

The time integration can now be performed, completing the numerical solution of the source vector $S(U)$ at each time step.

$$\begin{aligned}
(\alpha_g \rho_g)^{MH} &= \alpha_g^{n+1} \rho_g^{n+1} + \dot{m} \\
(\alpha_g \rho_g u_g)^{MH} &= \alpha_g^{n+1} \rho_g^{n+1} u_g^{VR} + \dot{m} V_i \\
(\alpha_g \rho_g E_g)^{MH} &= \alpha_g^{n+1} \rho_g^{n+1} E_g^{VR} + \dot{m} (L_{hv} + E_i) + \Delta t Q_i \\
(\alpha_l \rho_l)^{MH} &= \alpha_l^{n+1} \rho_l^{n+1} - \dot{m} \\
(\alpha_l \rho_l u_l)^{MH} &= \alpha_l^{n+1} \rho_l^n u_l^{VR} - \dot{m} V_i \\
(\alpha_l \rho_l E_l)^{MH} &= \alpha_l^{n+1} \rho_l^n E_l^{VR} - \dot{m} (L_{hv} + E_i) - \Delta t Q_i
\end{aligned} \tag{3.57}$$

3.3 Solution Procedure for Optimal Control System

The method for obtaining the discretized flow field, single- and two-phase, was described in Sections 1 and 2 of this Chapter respectively. To proceed with numerical conditions based on the optimal control system, it is assumed that an entire flow field $U_k(x_i, t^n)$ is known for all spatial indices i , temporal indices n and variable indices k . The vast majority of the additional computational complexity required to satisfy all conditions of the optimal system is solving the adjoint PDE. Since the method is nearly identical for both the single- and two-phase calculations it will be described first.

A survey of the literature on numerical methods for optimal control [77]-[89] gave insight on how to construct an adjoint-based method of solution. However, there were no methods specifically for distributed control with free initial and final data and final time for unsteady shock attenuation.

3.3.1 Discrete Form of Adjoint System

The continuous form of the adjoint PDE system is shown as the pairing with δU_j in Equation 2.69. The system is linear in the adjoint variables. The time derivative of the entire adjoint vector for all space at a discrete time t^n is shown in column-upon-column form in Equation

3.58. Let m be the number of spatial grid points and k be the number of adjoint variables. Then the adjoint vector V at a discrete moment in time will be of size km by 1 and the matrices in Equation 2.69 will be of size km by km . A single component of the adjoint vector, eg. $V_1(x, t)$, will be size m by 1 at each time step.

$$\frac{\partial V_k^l}{\partial t} \leftrightarrow \frac{\partial}{\partial t} \left(\begin{array}{c} \left(\begin{array}{c} V_1(x_1, t^n) \\ V_1(x_2, t^n) \\ \vdots \\ V_1(x_m, t^n) \end{array} \right) \\ \left(\begin{array}{c} V_2(x_1, t^n) \\ V_2(x_2, t^n) \\ \vdots \\ V_2(x_m, t^n) \end{array} \right) \\ \vdots \\ \left(\begin{array}{c} V_k(x_1, t^n) \\ V_k(x_2, t^n) \\ \vdots \\ V_k(x_m, t^n) \end{array} \right) \end{array} \right) \quad (3.58)$$

All of the matrices in Equation 2.69 have a block diagonal structure. The Jacobian matrix for all of space at t^n is shown in Equation 3.59.

$$A_{k\nu}(U^n) \leftrightarrow$$

$$\left(\begin{pmatrix} A_{11}(x_1, t^n) & & \\ & \ddots & \\ & & A_{11}(x_m, t^n) \end{pmatrix} \cdots \begin{pmatrix} A_{1k}(x_1, t^n) & & \\ & \ddots & \\ & & A_{1k}(x_m, t^n) \end{pmatrix} \right) \cdots \left(\begin{pmatrix} A_{k1}(x_1, t^n) & & \\ & \ddots & \\ & & A_{k1}(x_m, t^n) \end{pmatrix} \cdots \begin{pmatrix} A_{kk}(x_1, t^n) & & \\ & \ddots & \\ & & A_{kk}(x_m, t^n) \end{pmatrix} \right) \quad (3.59)$$

The adjoint PDE is given in discrete form with an explicit integration in Equations 3.60 and 3.61.

$$\frac{1}{\Delta t} I (V_k^{n-1} - V_k^n) + R(U^n) V_i^n = 0 \quad (3.60)$$

$$R(U) = A \cdot DU + \frac{\partial A}{\partial x} - \frac{\partial A}{\partial U} \cdot \frac{\partial U}{\partial x} + \frac{\partial S}{\partial U} \quad (3.61)$$

The matrix D is made up of discrete spatial derivative block matrices, central differencing in the domain interior, upwind differencing at the outlet and downwind at the inlet. A single block is shown in Equation 3.62.

$$D_{M \times M} = \frac{1}{2\Delta x} \begin{pmatrix} -2 & 2 & & \\ -1 & 0 & 1 & \\ & \ddots & \ddots & \ddots \\ & & -1 & 0 & 1 \\ & & & 2 & -2 \end{pmatrix} \quad (3.62)$$

Each time step of the adjoint solution has four parts. Before time integration, the matrix R must be assembled. Some of the matrices which make up R are known in closed form and require no

discretized derivative. The 3-component system requires assembling A and $\frac{\partial A}{\partial U}$ from the known state data. The 7-component system requires, in addition, assembling $\frac{\partial S}{\partial U}$ which has terms with mixed closed form and discrete derivatives. The second part of the solution requires assembling the matrix and vectors that have discrete derivatives $\frac{\partial A}{\partial x}$, $\frac{\partial V}{\partial x}$ and $\frac{\partial U}{\partial x}$. These two parts can be done in parallel. The third part, calculating R , requires sharing memory between processes and does not lend itself well to parallelization. With careful direction of memory, there is more potential in the assembly of R for speed optimization than will be shown in the results in Section 4.4. The final part of the adjoint time step is the time integration which boils down to matrix addition and matrix-vector multiplication for the explicit scheme. These operations are known to be adaptable to parallelization in a straightforward way.

For adjoint calculations of a scalar PDE with a discontinuity, it has been shown [91] that a relaxed system with second order dissipation will recover the non-linear PDE in the limit of vanishing viscosity. A small numerical viscosity can stabilize the adjoint solution. These ideas have been extended to fluid dynamics systems [92] and are implemented in the current work, in a manner which maintains consistency, for both the single- and two-phase numerical adjoint solutions.

3.3.2 Formulation and Solution of Single-Phase Control Problem

The goal of the calculation is to minimize the finite approximation to the cost functional J while also converging to a solution that satisfies all of the necessary conditions of the optimal system. The cost functional from Equation 2.79 is given in discrete form in Equation 3.63.

$$J = \sum_{i=1}^M \sum_{n=1}^N \frac{a}{2} z(x_i, t^n)^2 \Delta x \Delta t + \sum_{x_i \in \Omega_s} \frac{b}{2} \max \left(P_g(x_i, t^N) - Q(x_i, 0) \right)^2 \Delta x \quad (3.63)$$

Henceforth, i will replace j as the spatial index. The state vector U is constrained to the Euler System with a distributed control z in the energy balance equation.

$$U = (\rho(x_i, t^n), \rho u(x_i, t^n), \rho E(x_i, t^n))^T \quad (3.64)$$

$$\frac{\partial}{\partial t} \begin{pmatrix} \rho \\ \rho u \\ \rho E \end{pmatrix} + \frac{\partial}{\partial x} \begin{pmatrix} \rho u \\ \rho u^2 + P \\ u(\rho E + P) \end{pmatrix} = \begin{pmatrix} 0 \\ 0 \\ z(x_i, t^n) \end{pmatrix} \quad (3.65)$$

$$\rho E(x_i, t^n) = \rho e(x_i, t^n) + \frac{\rho u^2}{2}(x_i, t^n) \quad (3.66)$$

$$P(x_i, t^n) = \rho e(x_i, t^n) (\gamma - 1) \quad (3.67)$$

Initial Conditions are stationary air at sea-level throughout the domain.

$$\begin{aligned} \rho(x_i, t^0) &= 1 \text{ kg/m}^3 \\ u(x_i, t^0) &= 0 \text{ m/s} \\ P(x_i, t^0) &= 10^5 \text{ Pa} \\ \rho u(x_i, t^0) &= 0 \text{ kg/m}^2 \cdot \text{s} \\ \rho e(x_i, t^0) &= 250000 \text{ J} \\ \rho E(x_i, t^0) &= 250000 \text{ J} \end{aligned} \quad (3.68)$$

The control solution procedure requires a solution of the flow under the influence of the l^{th} control iterate z^l . Therefore, the initial control iterate will be zero $z^0 = 0$. The first iterate of the final time T^0 is chosen so that the shock wave is allowed enough time to almost traverse the domain Ω . In this way, the greatest potential for the effect of control action on pressure attenuation is possible. At the final time T^l the necessary condition on the adjoint vector was given in Equation 2.97 and is shown in discrete form in Equation 3.69 for all $x_i \in \Omega_s$.

$$\begin{aligned}
V_1^l(x_i, T^l) &= b \cdot \max\left(\left(P(x_i, T^l) - Q(x_i)\right), 0\right) \frac{u(x_i, T^l)^2}{2} (\gamma - 1) \\
V_2^l(x_i, T^l) &= -b \cdot \max\left(\left(P(x_i, T^l) - Q(x_i)\right), 0\right) u(x_i, T^l) (\gamma - 1) \\
V_3^l(x_i, T^l) &= b \cdot \max\left(\left(P(x_i, T^l) - Q(x_i)\right), 0\right) (\gamma - 1)
\end{aligned} \tag{3.69}$$

The adjoint PDE is then solved backward in time as described in Section 3.3.1. This gives all of the adjoint variables $V_k(x_i, t^n)$ over time on the same discrete grid as the flow variables. A new control iterate is obtained from the discrete form of Equation 2.99.

$$\begin{aligned}
\delta z^{l+1}(x_i, t^n) &= -V_3^l(x_i, t^n)/a \\
z^{l+1}(x_i, t^n) &= z^l(x_i, t^n) + \delta z^{l+1}(x_i, t^n)
\end{aligned} \tag{3.70}$$

Physical control constraints are then imposed. Since the calculation concerns shock attenuation, extracting energy from the gas using a *sink* is of interest. Consequently, $z^l \leq 0$ for all space and time is enforced. It has been shown that the adjoint variables will travel along the characteristics of the flow in the opposite direction. This means that the calculation will suggest putting control ahead of the shock wave which we are not interested in since droplet-shock interactions only take energy out of the gas *behind* the shock wave. Therefore, Equation 3.72 gives the restrictions on the control.

$$z^{l+1}(x_i, t^n) = \begin{cases} 0 & \text{if } z^{l+1}(x_i, t^n) > 0 \\ 0 & \text{if } x_i > S \cdot t^n \end{cases} \tag{3.71}$$

Lastly, the final time is updated according to Equation 3.72 and 3.73. It is important to mention that changing the final time does not change the number of time steps N . This means that the time step will be slightly different between solution iterates but will still obey the CFL condition. This also means that control strengths defined on the time discretization of a previous iterate will be shifted when applied to the current flow solution. Overall convergence of the algorithm

ensures that these differences are not detrimental and, as the final time converges, so will these discrepancies.

$$f(T^l) = \sum_{i=1}^m \frac{a}{2} z(x_i, t^N)^2 \Delta x + b(P_g(x_i, t^N) - Q(x_i)) \left((\gamma - 1) \cdot \left[\frac{u_g(x_i, t^N)^2}{2} \frac{\rho_g(x_i, t^N) - \rho_g(x_i, t^{N-1})}{\Delta t} + u_g(x_i, t^N) \frac{\rho_g u_g(x_i, t^N) - \rho_g u_g(x_i, t^{N-1})}{\Delta t} + \frac{\rho_g E_g(x_i, t^N) - \rho_g E_g(x_i, t^{N-1})}{\Delta t} \right] + \frac{P_g(x_i, t^N) - P_g(x_i, t^{N-1})}{\Delta t} \right) \Delta x \quad (3.72)$$

$$T^{l+1} = T^l - \frac{f(T^l)}{\frac{df}{dt}(T^l)} \quad (3.73)$$

As long as each iterate of the final time T^{l+1} is not too far from the optimal value T^* , the variable will converge in the optimal control solution procedure and the properties in Equation 3.74 will be true. The definition of $\frac{df}{dt}$ and its discretization are given in Appendix C.

$$\begin{aligned} \lim_{l \rightarrow \infty} T^{l+1} &= T^* \\ \lim_{l \rightarrow \infty} f(T^{l+1}) &= f(T^*) = 0 \end{aligned} \quad (3.74)$$

The discrete form of the functional f from Equation 2.98 is given in Equation 3.72, using the definition of the derivatives of pressure from Equation 2.97. The overall algorithm which is used to satisfy all of the above necessary optimal conditions is shown in block-diagram form in Figure 3.3

Blast wave simulation data at a fixed point in space will be provided as an inlet boundary condition. If the state of the flow is supersonic, the condition will be explicitly applied. If the flow is subsonic, a non-reflecting boundary condition of the outgoing $u - c$ characteristic wave will be enforced [93], [94].

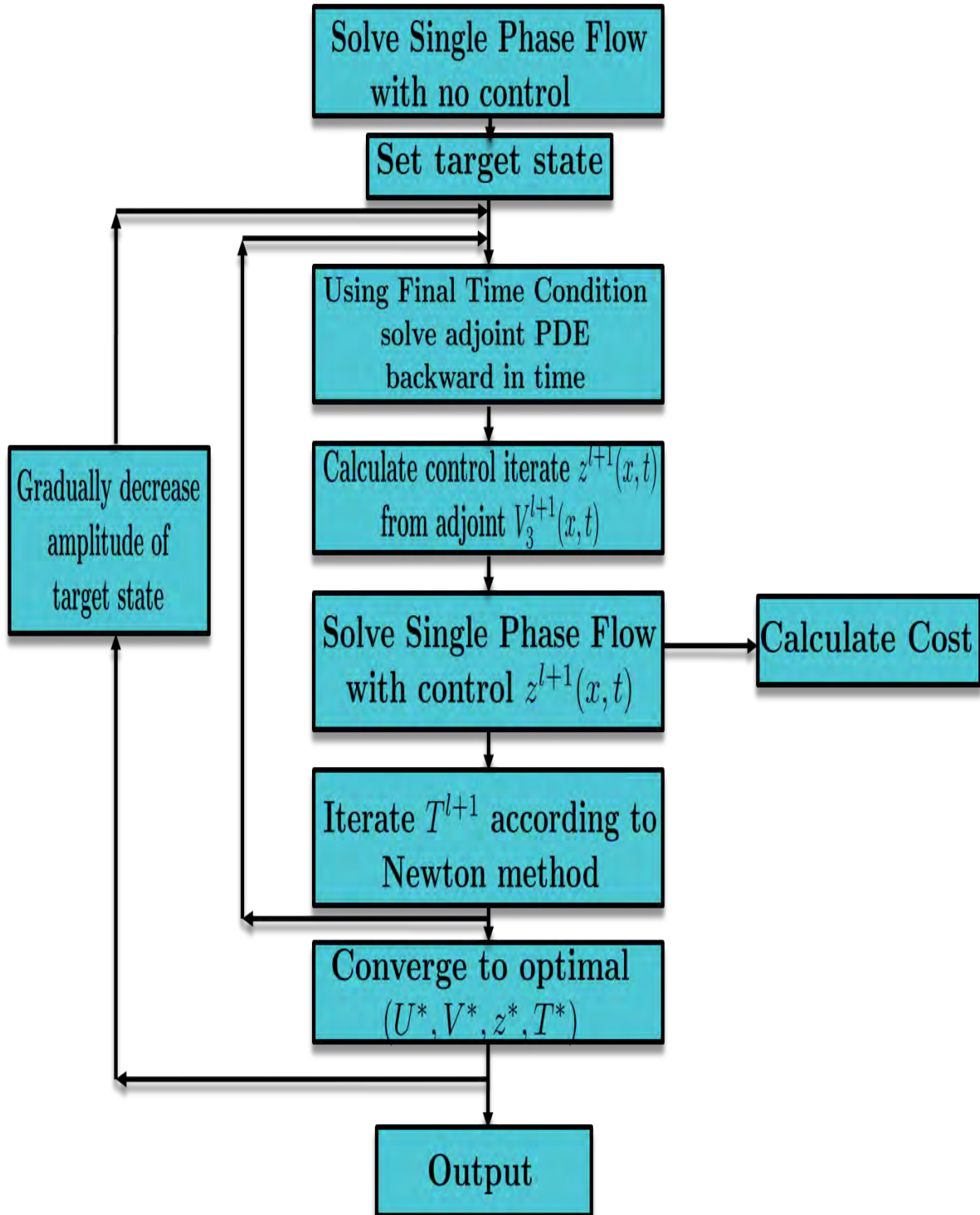


Figure 3.3: Block diagram of solution procedure for single-phase control calculation

3.3.3 Formulation and Solution of Two-Phase Control Problem

The solution procedure for the two-phase control problem is very similar to that of the single-phase control problem. The major distinction is that an adjoint PDE must be solved backward in time to fix an initial condition on a free state variable rather than to calculate a distributed control over time. The cost functional J , given in Equation 2.100 and shown in discrete form in Equation 3.76, will be minimized while all constraints of the two-phase model are obeyed.

$$J = \sum_{i=1}^M \frac{a}{2} \alpha_l^2(x_i, t^0) \Delta x + \sum_{x_i \in \Omega_s} \frac{b}{2} \max(P_g(x_i, t^N) - Q(x_i), 0)^2 \Delta x \quad (3.75)$$

There is no running penalty necessary since the cost associated with control action is penalized at the initial time and the cost associated with missing the target pressure profile need only be assessed at the final time. Recall the state vector in primitive form, $\tilde{U} = (\alpha_g, \rho_g, u_g, P_g, \rho_l, u_l, P_l)^T$ and the constraint on the free initial data $\alpha_g + \alpha_l = 1$ and $0 < \alpha_l < 1$, throughout the simulation domain Ω . The rest of the state variables have fixed initial conditions that are given in Equation 2.104. The dynamical constraints of the two-phase system are solved in their conservative form as in Equation 2.24, but since it is convenient to define the target state in terms of the pressure, and the Jacobian has already been provided [31], the resulting necessary conditions are simplified. The adjoint PDE is derived from the Jacobian form in the primitive basis shown in Equation 2.51. The non-trivial elements of the matrices are given in Appendices A and B.

Analogous to Equation 3.69 the necessary condition on the adjoint vector at the final time is given for all $x_i \in \Omega_s$.

$$V_k^l(x_i, T^l) = \begin{cases} b \cdot \max(P(x_i, T^l) - Q(x_i), 0) & k = 4 \\ 0 & k \neq 4 \end{cases} \quad (3.76)$$

With the final time condition, the adjoint PDE can be solved backward in time to arrive at a value for $V_1^l(x_i, 0)$. From the necessary condition given in Equation 2.107, the volume fraction of liquid at each point in space will be iterated, within the constraints, via a Newton method shown in Equation 3.77.

$$\begin{aligned}\alpha_g^{l+1}(x_i, t^0) &= \alpha_g^l(x_i, t^0) - \frac{a(1 - \alpha_g^l(x_i, t^0)) - V_1^l(x_i, t^0)}{-a} \\ \alpha_i^{l+1} &= 1 - \alpha_g^{l+1}\end{aligned}\tag{3.77}$$

To solve for the optimal final time, the Transversality Condition for the two-phase system, given in Equation 2.115, is define as a continuous function $f(T)$ with the final time as the independent variable. Then $f(T^*) = 0$ at the optimal final time T^* . As in the single-phase case, T^* can be solved iteratively with the Newton method from Equation 3.72 using the discretization of f in Equation 3.78.

$$f(T^l) = \sum_{i=1}^m (P_g(x_i, t^N) - Q(x_i)) \frac{P_g(x_i, t^N) - P_g(x_i, t^{N-1})}{\Delta t} \Delta x \tag{3.78}$$

The definition of $\frac{df}{dt}$ and its discretization are also given in Appendix C. The overall algorithm which is used to satisfy all of the above necessary optimal conditions is shown in block-diagram form in Figure 3.4.

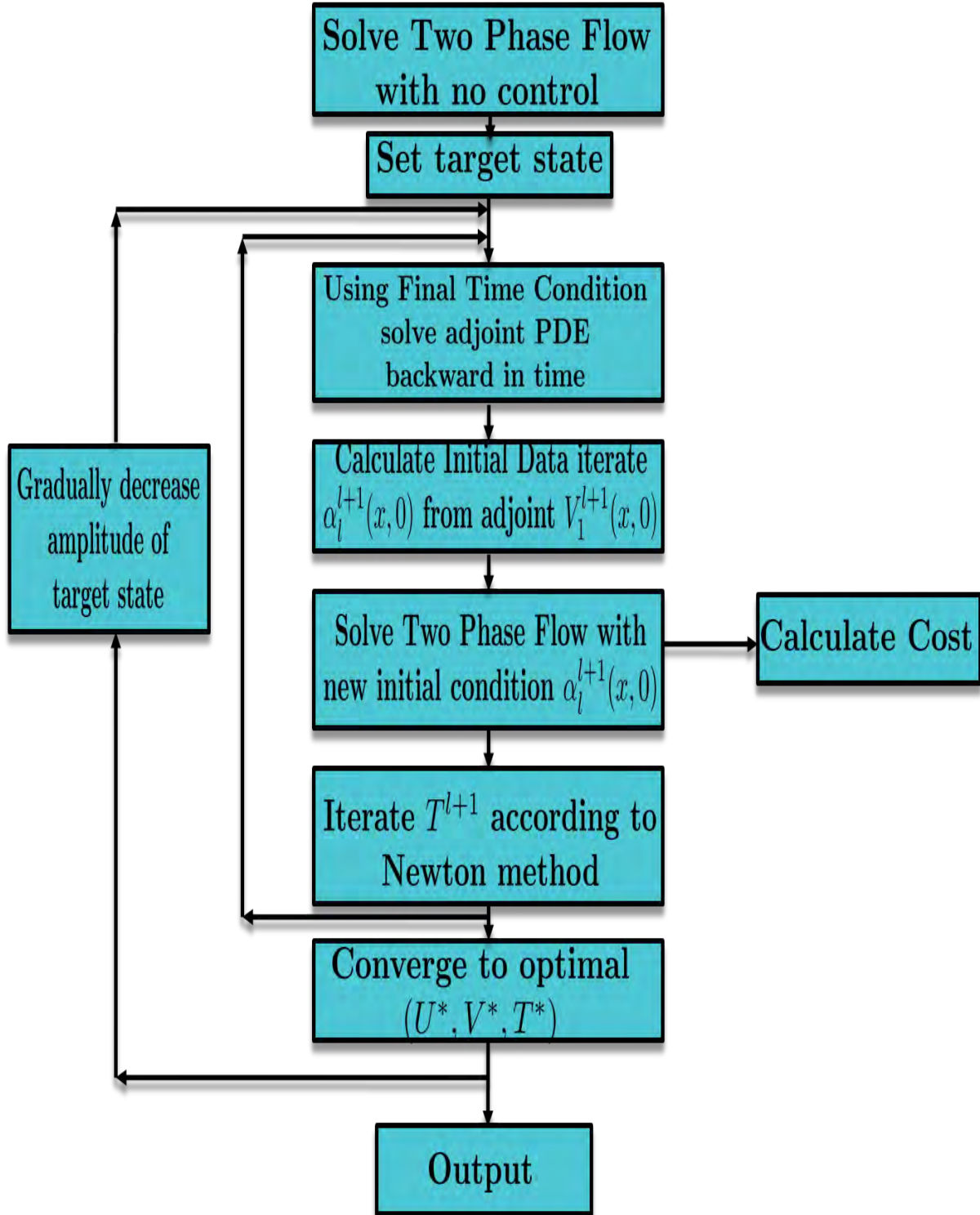


Figure 3.4: Block diagram of solution procedure for two-phase control calculation

THIS PAGE INTENTIONALLY LEFT BLANK

CHAPTER 4:

Results and Discussion

4.1 IOP Simulations in 2D using FASTRAN

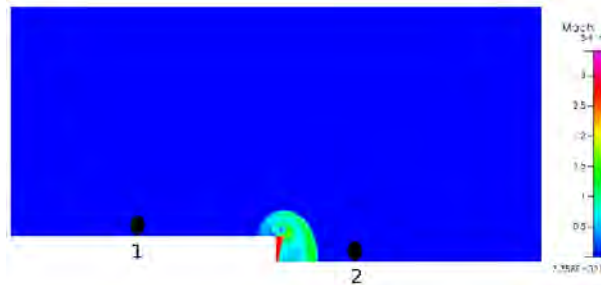


Figure 4.1: Simulated Shuttle IOP: Mach number at 1.2 ms

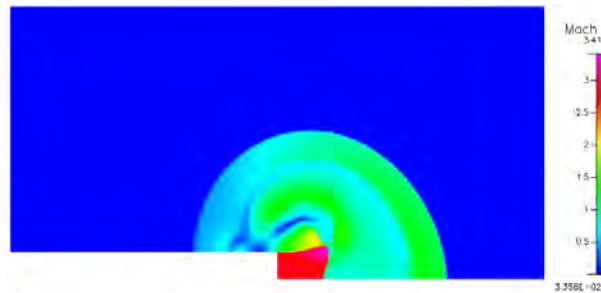


Figure 4.2: Simulated Shuttle IOP: Mach number at 4 ms

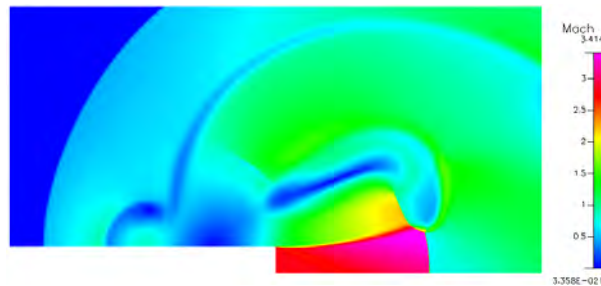


Figure 4.3: Simulated Shuttle IOP: Mach number at 10 ms

Data on the Shuttle's grain and chamber pressure [95] was given as input to Cequel, [96] a code for steady state rocket property calculations. The output gives the temperature and gas velocity

at the nozzle exit plane for a given pressure ratio. Initially, ambient conditions inside the domain are present. The ignition sequence was simulated in 2D using the ESI-Fastran Solver [97].



Figure 4.4: Simulated Shuttle IOP: pressure at 1.2 ms

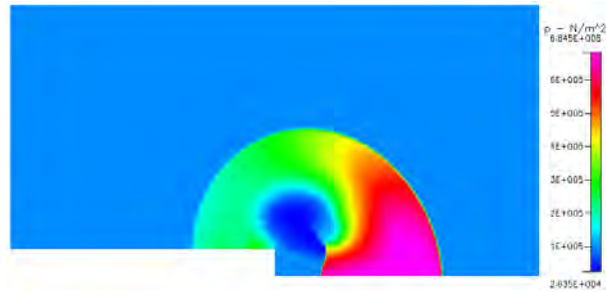


Figure 4.5: Simulated Shuttle IOP: pressure at 4 ms

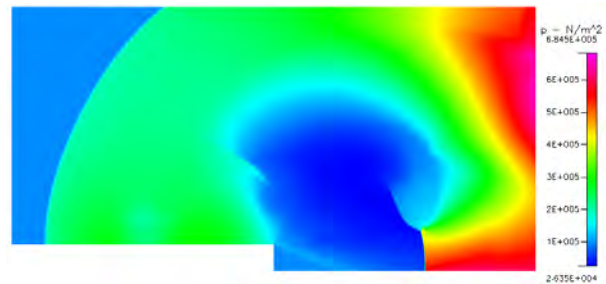


Figure 4.6: Simulated Shuttle IOP: pressure at 10 ms

Constant mass-flow boundary conditions equivalent to the steady state exit plane of the rocket nozzle on the shuttle were used in the bottom center of the domain on the right face of the step as shown in Figure 4.1. Mach number is depicted in three snapshots in Figures 4.1, 4.2 and 4.3 and pressure in Figures 4.4, 4.5, and 4.6. The last frame is roughly 10 *ms* after ignition. The bottom left edge of the domain represents the rocket body while the bottom right edge is the

centerline of the normal to the nozzle exit plane and a symmetry boundary. All other edges are non-reflecting boundaries.

Flow conditions over time were recorded at two locations marked in Figure 4.1. Point 1 is near the rocket body 2.5 meters above the nozzle and Point 2 is 1.5 meters along the symmetry boundary and the plane normal to the nozzle exit. The conditions at the recorded locations are used as the boundary conditions in both the single- and two-phase control calculations.

Figure 4.7 shows the flow conditions over time at Monitor Point 1 near the rocket body and Figure 4.8 shows the flow conditions over time for Monitor Point 2 directly downstream of the nozzle.

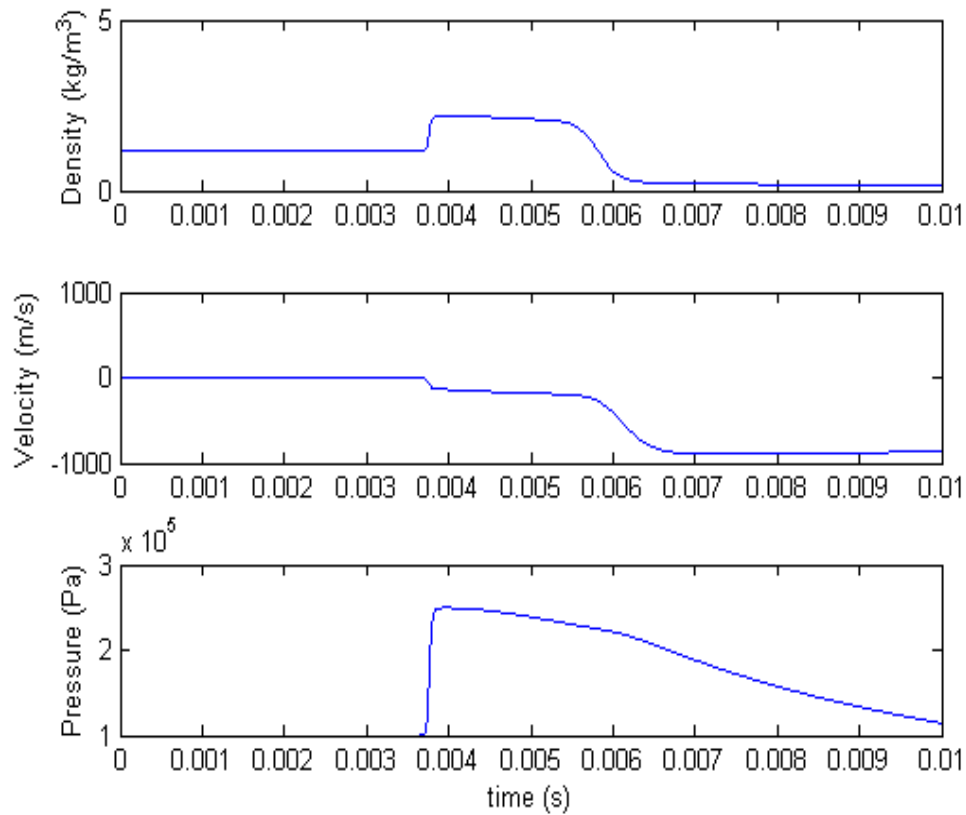


Figure 4.7: Flow conditions over time for Monitor Point 1

It is worth mentioning that the two-dimensional flow cannot be truly replicated by an inlet boundary condition to a single-dimensional calculation. Neglecting motion in the transverse di-

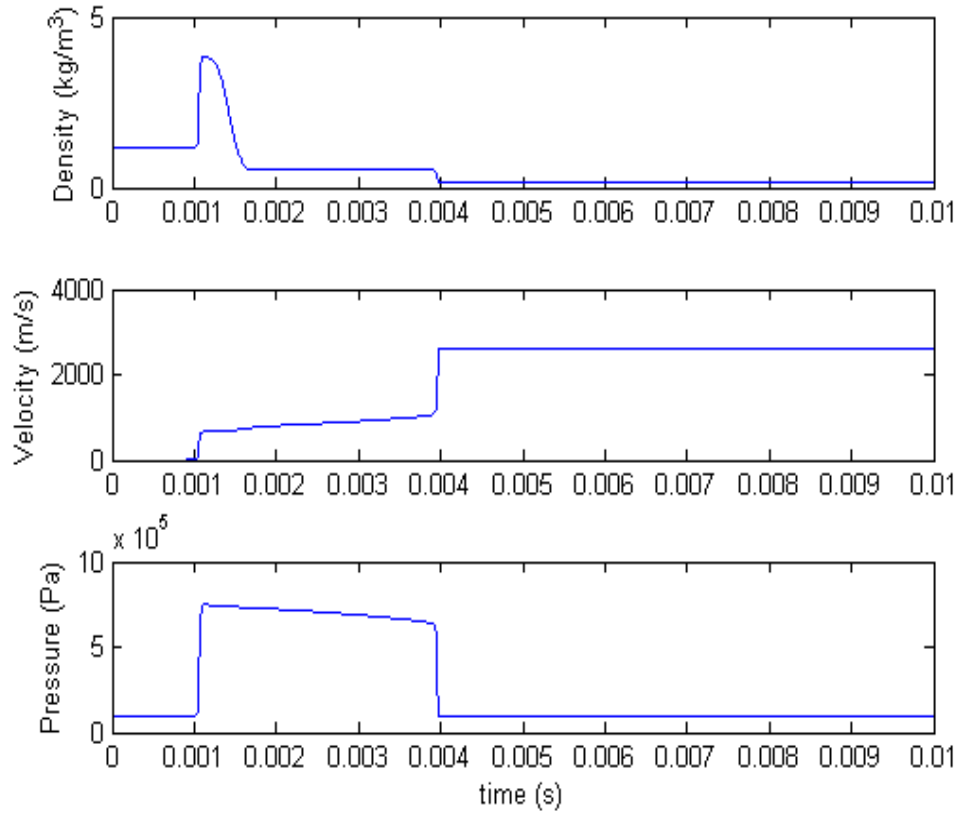


Figure 4.8: Flow conditions over time for Monitor Point 2

rection while taking (ρ, u, P) explicitly means that the resulting driver gas has a lower temperature. This is not discouraging since intuition would suggest that hotter gas has more potential to vaporize water droplets and hence by the nature of the control action, there is more potential for effectiveness. The goal is to be able to handle a range of blast waves that will plausibly be seen in an IOP environment.

4.2 Single-Phase Control Calculation Results

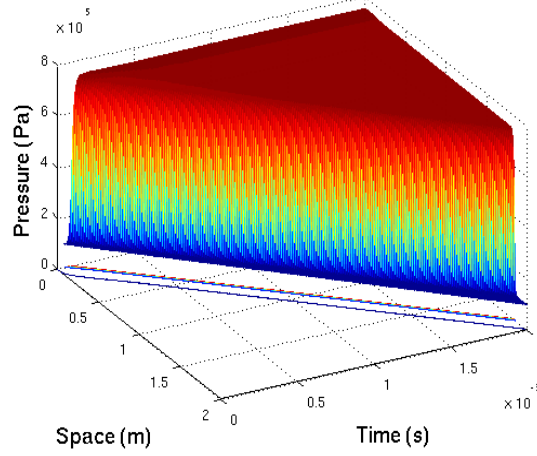


Figure 4.9: Monitor Point 2, Pressure profile at final time, no control used.

These results were published by the author [98]. The solution procedure in Figure 3.3 assumes a given target state $Q(x)$ at the final time T^* . To illustrate trends in the optimal control solution, prescribing a consistent and meaningful target state or sequence of target states is a necessity. Figure 4.9 shows the uncontrolled pressure profile over time. An example of a target state, shown in red in Figure 4.10, has 85% of the amplitude of the final pressure profile when no control is used, OP_0 , shown in blue. This attenuated pressure profile replaces the uncontrolled pressure profile from just behind the shock front to 30 cm from the inlet boundary. The target is then linearly increased to the magnitude of the uncontrolled pressure profile over 10cm. Upstream of the shock, the target state is such that only pressures greater than the target pressure are penalized. This will define Ω_s in the final time penalty. The nonlinear nature of shock waves means that not all target states may be possible for the given initial conditions and boundary conditions. In addition, the purpose of the calculation is to calculate control solutions which decrease overpressure and therefore the cost functional should not penalize pressures below the target pressure. Furthermore, error near the shock front is not directly penalized but is still minimized via the iterative update to the final time. This avoids taking a variation of the state variables near discontinuities, which will violate the assumption of a small variation. In each of the given examples the weighting constants a and b are 10^{-6} and 10^4 respectively. Since b is much larger than a , minimizing J is dominated by minimizing the final time penalty. The value for b is such that the magnitude of the third adjoint variable $V_3(x, t)$, and thus the control action

$z(x, t)$, are sufficient to cause noticeable attenuation to the blast wave.

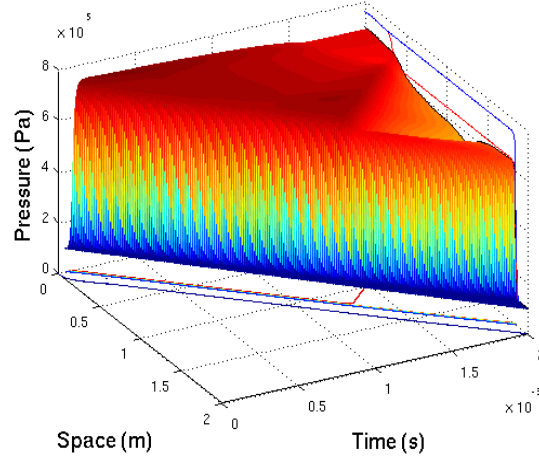


Figure 4.10: Monitor Point 2, Optimal pressure profile at final time, target state $Q(x) \sim 85\% OP_0$

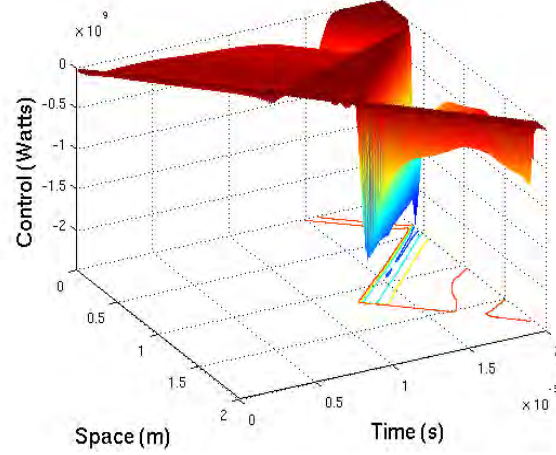


Figure 4.11: Monitor Point 2, Optimal distributed control, $Q(x) \sim 85\% OP_0$

The desired state cannot be directly set as described but must be gradually scaled down to the desired overpressure to assure convergence of the algorithm. It was found that when starting with an overpressure of 8:1 from Monitor Point 2 data, setting a target state with 85% of the uncontrolled overpressure, as in Figures 4.10, was the most attenuation to the shock that could be desired and still maintain convergence of the the algorithm. The reason for this can be understood in the nature of the optimal system. The optimal conditions are all coupled and

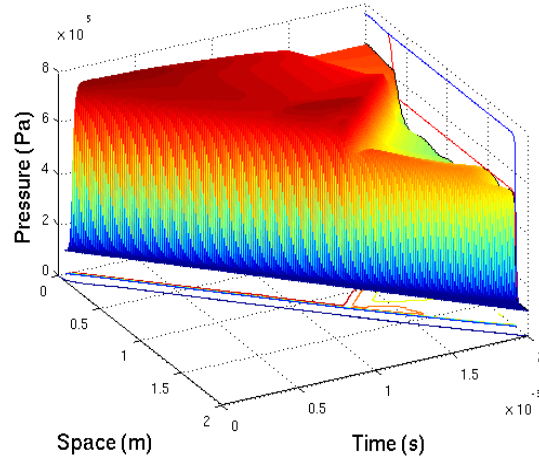


Figure 4.12: Monitor Point 2, Optimal pressure at final time, $Q(x) \sim 70\% OP_0$

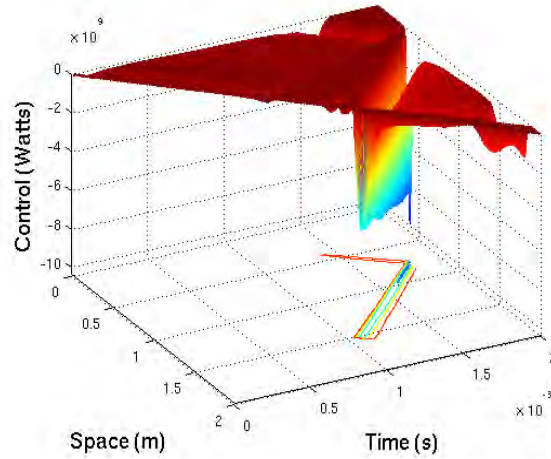


Figure 4.13: Monitor Point 2, Optimal distributed control, $Q(x) \sim 70\% OP_0$

inter-dependent such that a calculated blast wave under no control action is in no way close to the optimal pressure profile of a blast wave under considerable damping control action so as to render a blast wave that matches the target state with a significantly diminished overpressure. When the final time solution is not nearly optimal, then first-order corrections to these terms are not enough to exploit in an iterative sense toward finding an optimal control satisfying all necessary conditions.

Figure 4.11. is the corresponding distributed optimal control solution. Figures 4.12 and 4.13

are the optimal pressure and control solutions respectively for a target state that has 70% of the uncontrolled overpressure. Figures 4.14 and 4.15 are the optimal pressure and control solutions respectively for a target state that has 50% of the uncontrolled overpressure.

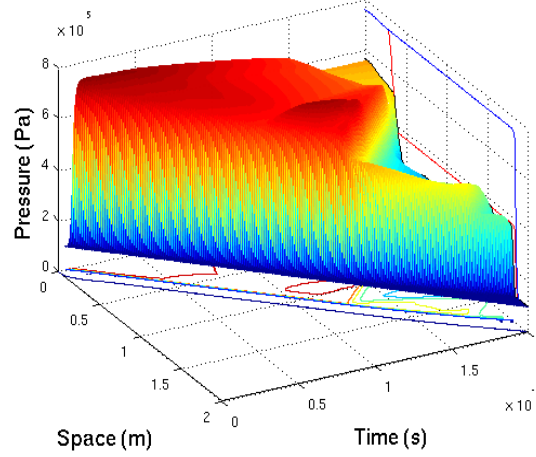


Figure 4.14: Monitor Point 2, Optimal pressure at final time, $Q(x) \sim 50\% \text{ } OP_0$

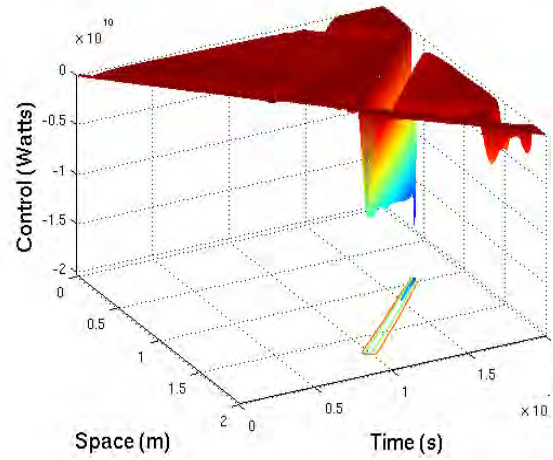


Figure 4.15: Monitor Point 2, Optimal distributed control, $Q(x) \sim 50\% \text{ } OP_0$

The top plot in Figure 4.16 is the logarithm of the cost functional J over solution iterations. The jumps in J every 25th iteration indicate that the target state $Q(x)$ has been redefined with a lower overpressure. The bottom plot in Figure 4.16 shows the corresponding final time T^* iterates with $T^0 = 2 \text{ ms}$.

A negative control in the energy equation can be thought of as an internal energy sink. Temperature is directly related to internal energy, so the control action cools the gas. A cooler gas has a lower speed of sound. Consequently, it will take longer for the shock front in the wave interacting with control to reach the same point in space that the shock without control reached. Additionally, from a hyperbolic wave theory point-of-view, a non-linear wave travels slower if it has less amplitude. The control action's purpose is to attenuate amplitude and this necessarily slows the wave down. The Transversality Condition is very sensitive to error at the shock front since this is where the time rate of change of the pressure is greatest. It would be a difficult matter to get significant attenuation in a converged solution with a fixed final time for this reason.

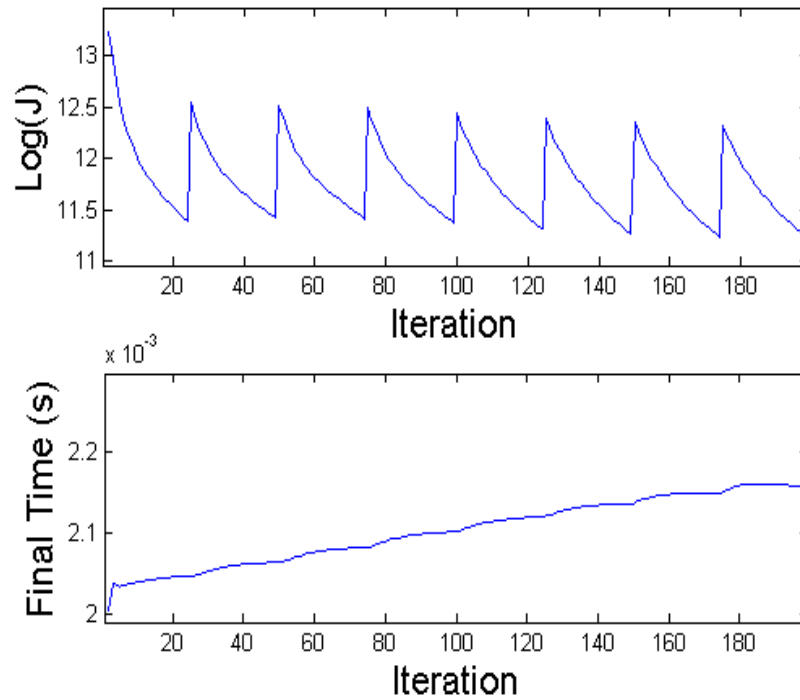


Figure 4.16: Monitor Point 2, Cost functional (top) and final time (bottom) vs. iteration, $Q(x) \sim 50\% OP_0$

In each example, a physical restriction on the control is imposed such that energy can only be taken out of the gas *behind* the shock wave. This more accurately portrays how discrete droplet sprays will sink energy from the gas via vaporization. The plots shown in Figures 4.17 and 4.18 are distributions of the energy equivalent vaporized water mass to the optimal control solutions.

By dimensional analysis, inspection of the energy balance equation indicates that the units of $z^*(x, t)$ are Watts. Integrating the control solution from $[0, T^*]$ gives an energy distribution in space. This energy can be directly equated to an amount of water mass that must be vaporized using the latent heat of vaporization of water $L_{hv} = -2.26 \cdot 10^6 \text{ J/kg}$ at 100° C . Equation 4.1 relates the optimal control solution, distributed in space and time, to an equivalent distribution of water mass vaporized over the same time interval.

$$m_{H_2Ov}(x) = \frac{1}{L_{hv}} \int_0^{T^*} z^*(x, t) dt \quad (4.1)$$

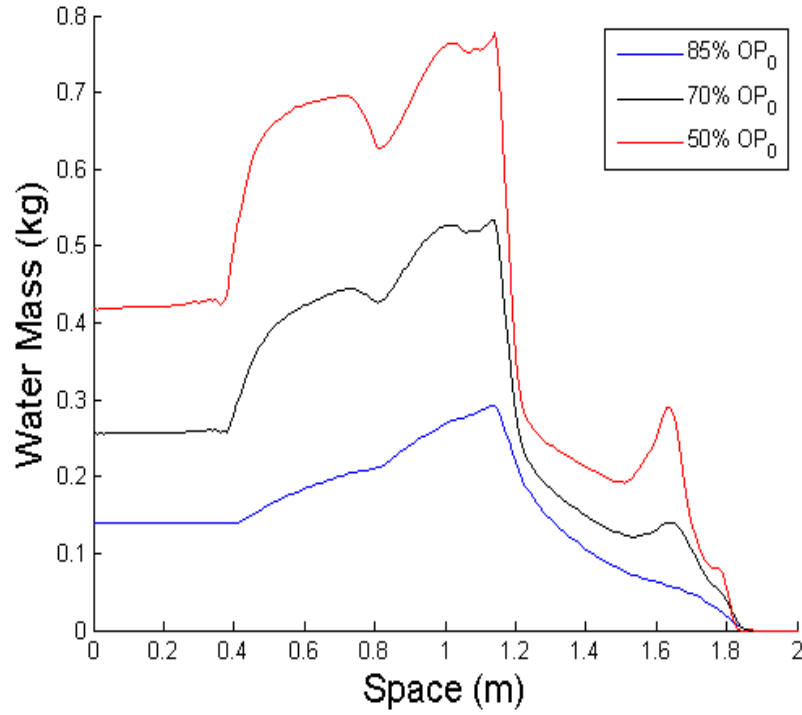


Figure 4.17: Monitor Point 2, $m_{H_2Ovape}(x)$, Energy equivalent distribution of water mass vaporized

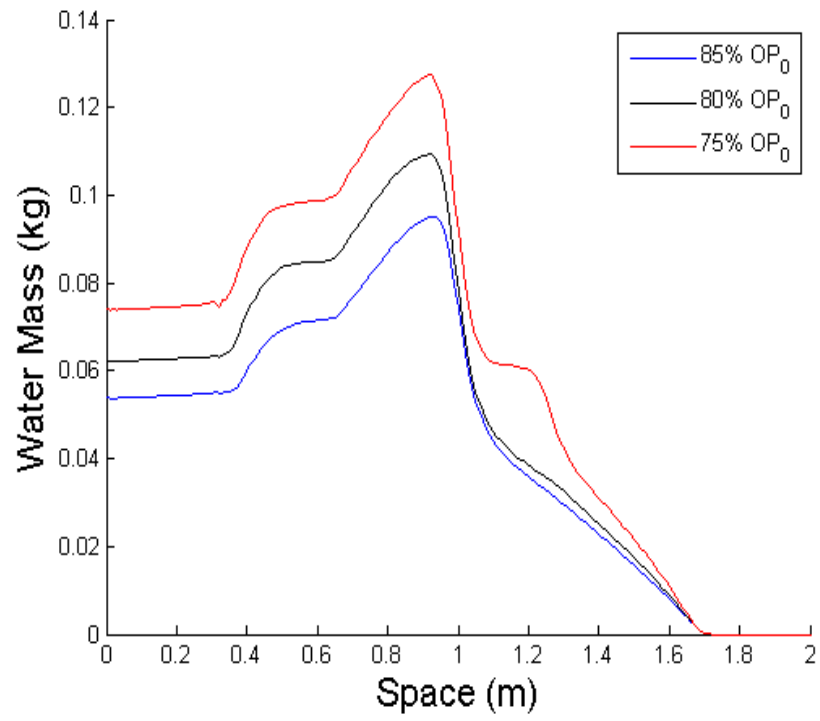


Figure 4.18: Monitor Point 1, $m_{H_2O_{vape}}(x)$, Energy equivalent distribution of water mass vaporized

Figures 4.17 and 4.18 show how the equivalent vaporized water mass distribution increases with increasing shock front attenuation. It can clearly be seen that more water is required to attenuate the stronger shock front using Monitor Point 2 data from directly in front of the rocket nozzle than from the weaker shock, Monitor Point 1 data, taken near the rocket body. Water takes time to vaporize and therefore cannot sink energy from the gas instantaneously and arbitrarily close to the shock front. In practice, water will take energy out of the gas at least a meter behind the shock front. That less energetic gas will then drive the shock with less energy and the pressure profile will flatten out to a diminished overpressure. With more detailed physically-based restrictions on the control action, this single-phase shock wave control formulation can be made to better replicate a two-phase shock-droplet interaction control calculation without the considerable added complexity of a two-phase compressible flow model. Regardless, trends in the data seem heuristically correct and therefore empirical scaling laws in magnitude and location may be sufficient.

4.3 Two-Phase Calculation Results

The results for the two-phase control problem were obtained with the algorithm shown in Figure 3.4. Figure 4.19 shows the optimal initial condition for the free water volume fraction variable. The curves give the optimal water volume fraction distribution for a given target state. The legend tells what percentage of the absolute overpressure of the uncontrolled blast wave was used to define the target state. In this case there is no artificial upper constraint on the maximum value of the volume fraction, aside from the physical limit of 1.

The limit of controllability over two meters is close to the target state 76% OP_0 . For each optimal initial water distribution, the resulting pressure profiles at the optimal final time T^* are shown in Figure 4.20.

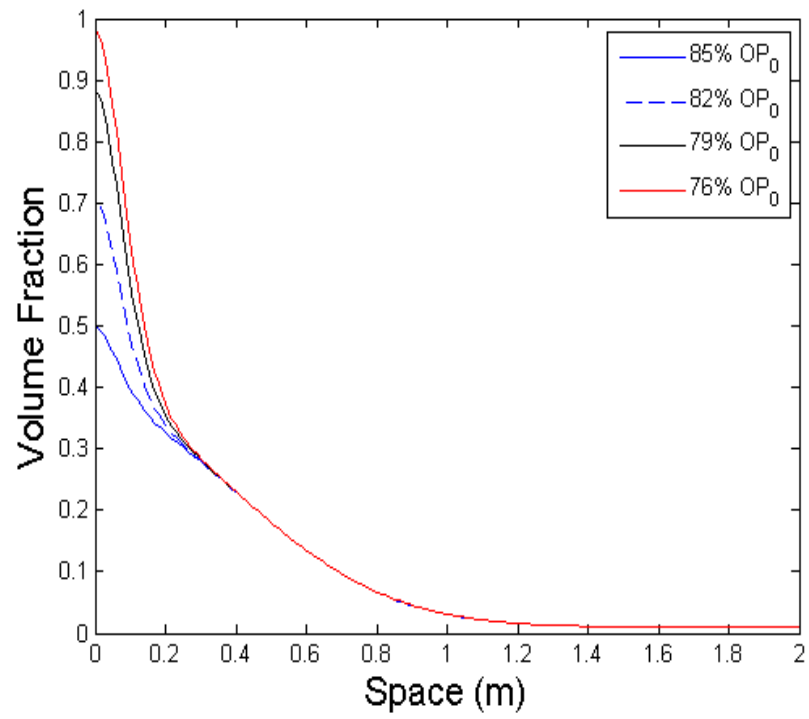


Figure 4.19: Optimal water volume fraction distributions $\alpha_l^*(x, 0)$, unconstrained at initial moment in time

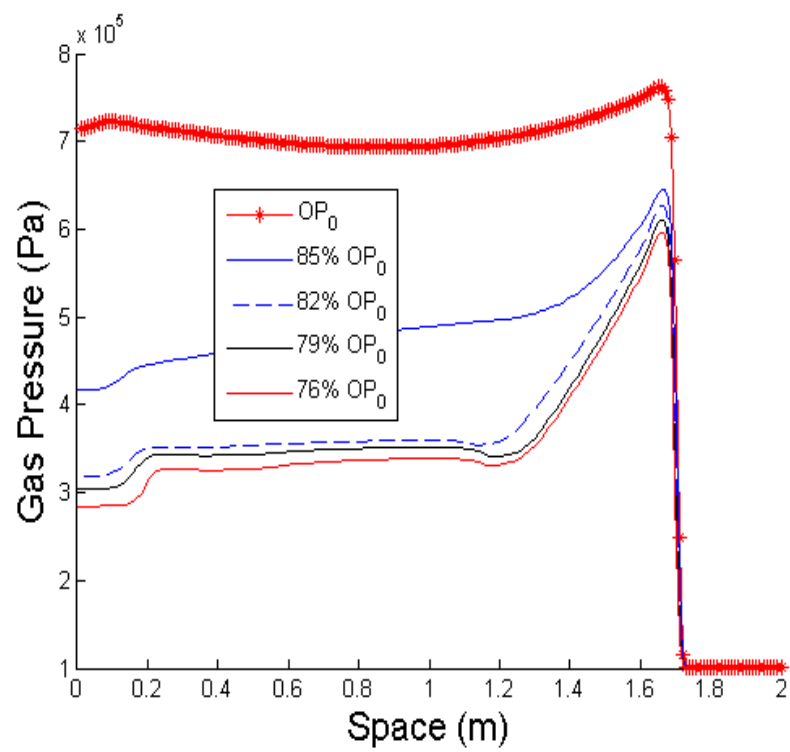


Figure 4.20: Optimal final time pressure profiles resulting from initial data in Figure 4.19

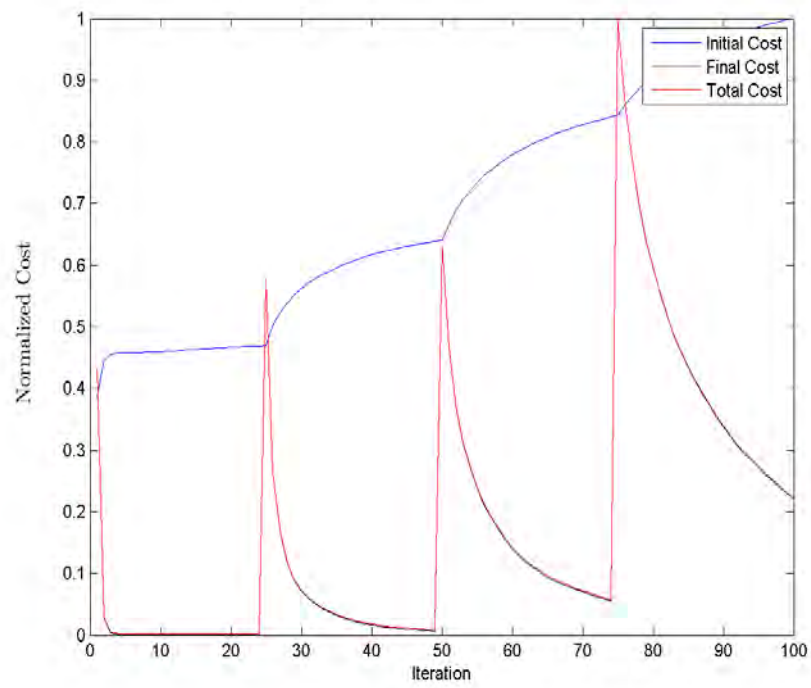


Figure 4.21: Cost functional J in red and initial penalty I over iterations of solution procedure in Figure 3.4

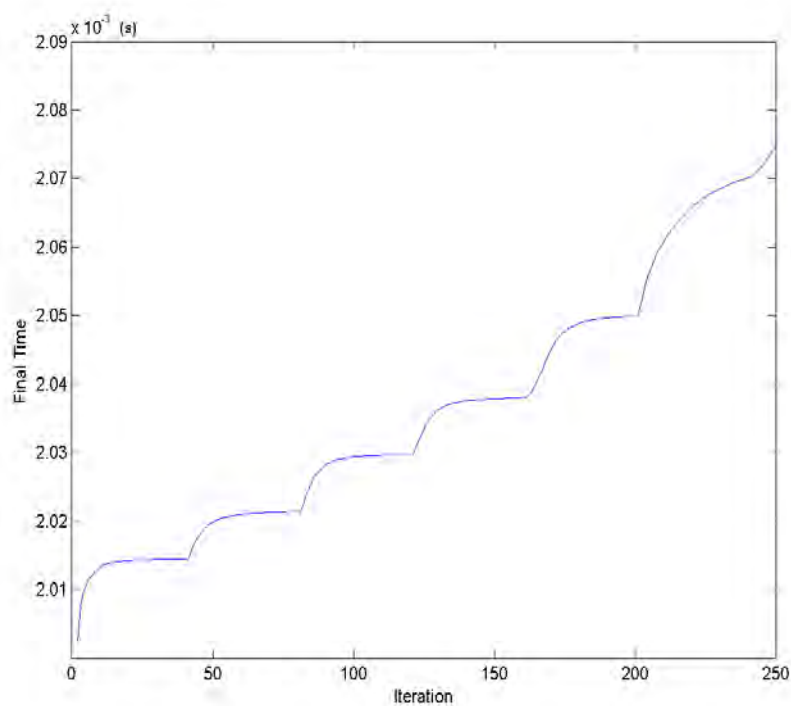


Figure 4.22: Final time, in seconds, vs iteration number for the unconstrained case. The regions of greatest slope are after iterations where the target state has been changed. The slope tending toward zero means that the solution is converging.

The convergence of the algorithm is shown in Figure 4.21. Every 25 iterations, the target state's amplitude is ramped down so that optimal solutions that yield ever increasing attenuation levels can be determined in a single execution of code. The history of the final time variable over the iterative solution procedure is shown in Figure 4.22.

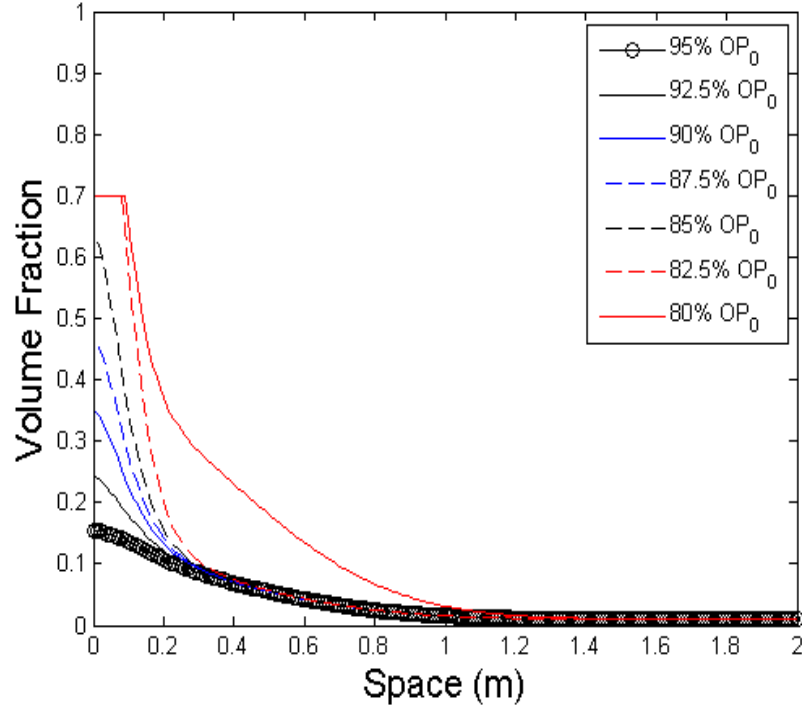


Figure 4.23: Optimal initial water volume fraction distributions, $\alpha_l(x, 0) \leq .7$

Another case was run with an upper bound on the volume fraction of water at 70%. The calculated optimal water distributions are shown in Figure 4.22 with the resulting pressure profiles shown in Figure 4.23.

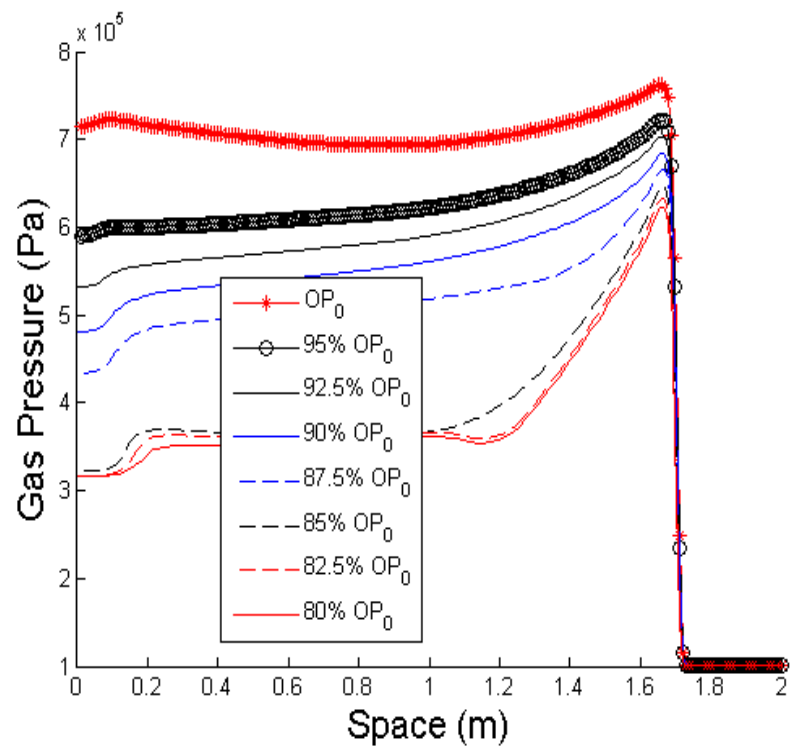


Figure 4.24: The optimal pressure profiles at the final time resulting from the control initial data in Figure 4.23

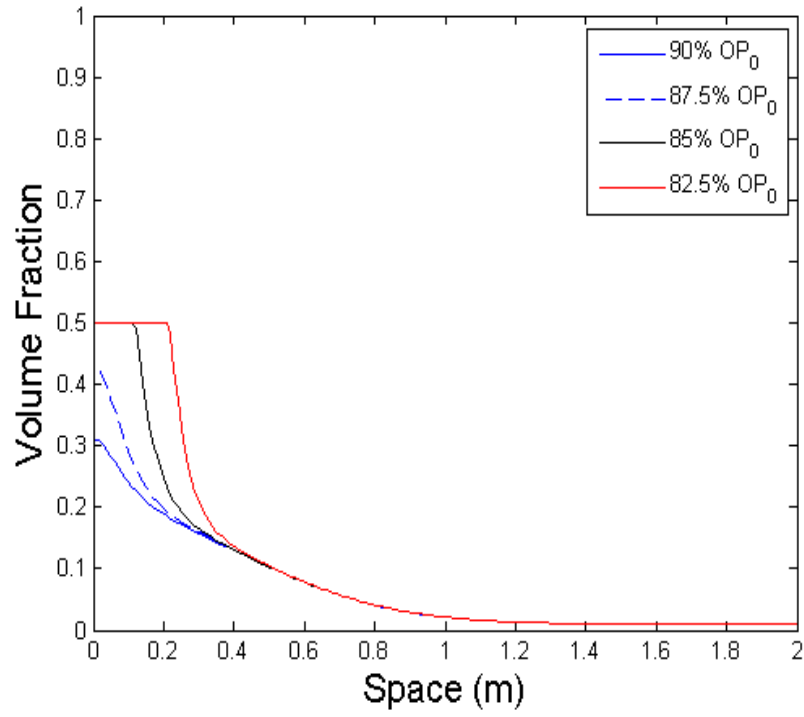


Figure 4.25: Optimal initial water volume fraction distributions, $\alpha_l(x, 0) \leq .5$

A final case was run, this time with an upper bound on the volume fraction of water at 50%. The calculated optimal water distributions are shown in Figure 4.25 with the resulting pressure profiles shown in Figure 4.26.

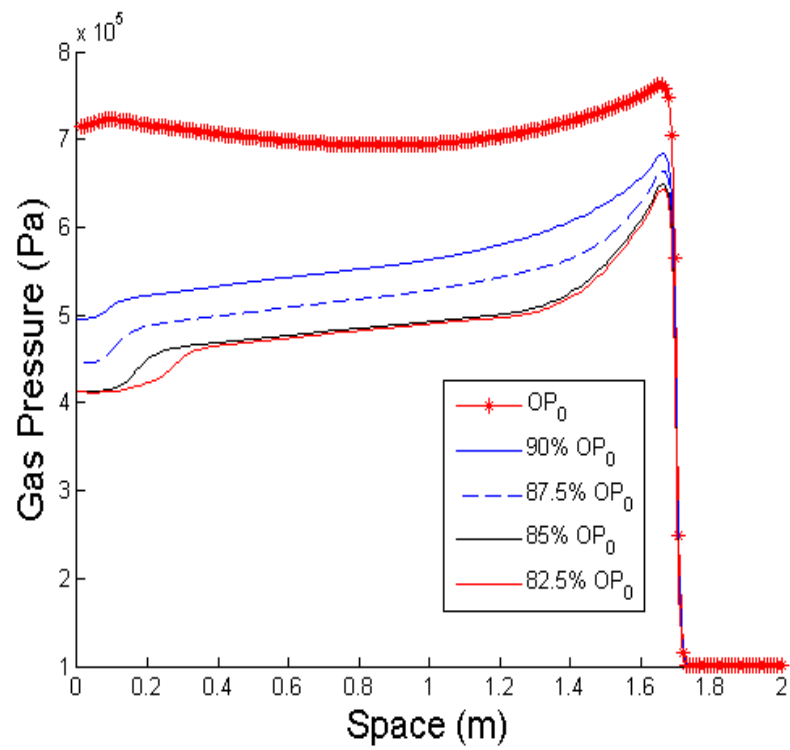


Figure 4.26: Optimal final time pressure profiles resulting from initial data in Figure 4.25

A few more isolated results were obtained in the interest of categorizing the significance of model parameters. Figure 4.27 shows the effect of droplet size on overpressure attenuation. Each pressure profile is plotted after two milliseconds of shock propagation from the left boundary toward the right. For a constant amount of water mass, more surface area of the droplets are exposed to the flow when the droplets are smaller. This is verified in Equation 4.2 for mono-dispersed droplets with diameter D_p .

$$\begin{aligned}
 S_p &= 4\pi \left(\frac{D_p}{2} \right)^2 \cdot N_p \\
 N_p &= \alpha_l \frac{\Delta x^3}{\frac{4}{3}\pi \left(\frac{D_p}{2} \right)^3} \\
 \Rightarrow S_p &\sim \frac{1}{D_p}
 \end{aligned} \tag{4.2}$$

This result agrees with empirical results that more exposed droplet surface area, the greater the overpressure attenuation [12]. Since surface area is maximized with infinitely small droplets, initial droplet size isn't an optimizeable parameter. Droplets with a diameter $D_p = 25\mu m$ were used in all of the preceding results since that size is small enough to have a significant effect over two meters, is a reasonable size based on injector atomizer specifications and prevents the droplets from being completely vaporized within the simulation time T^* . Avoiding complete vaporization is desirable since a non-zero volume fraction of either phase is a prerequisite to the model being used [31].

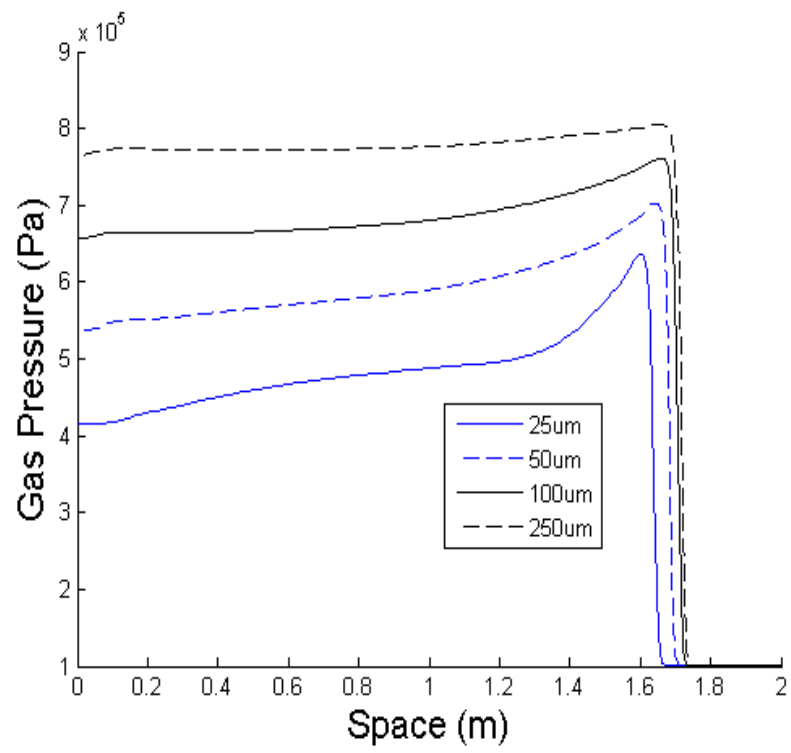


Figure 4.27: Effect of variable droplet size

Water vapor density was shown to have a drastic effect on results for optimal water distributions. According to the steam table data [42], water vapor density increases by an order of magnitude from ambient pressure to the 8 atm level behind the shock front. Therefore, if water vaporizes under high pressures, much more mass changes phase and consequently, the dissipative effect of vaporization is much more significant. The results in Figure 4.28 show that more than twice as much water is needed to get 5% attenuation in pressure depending on what the gas pressure surrounding the droplets when they vaporize.

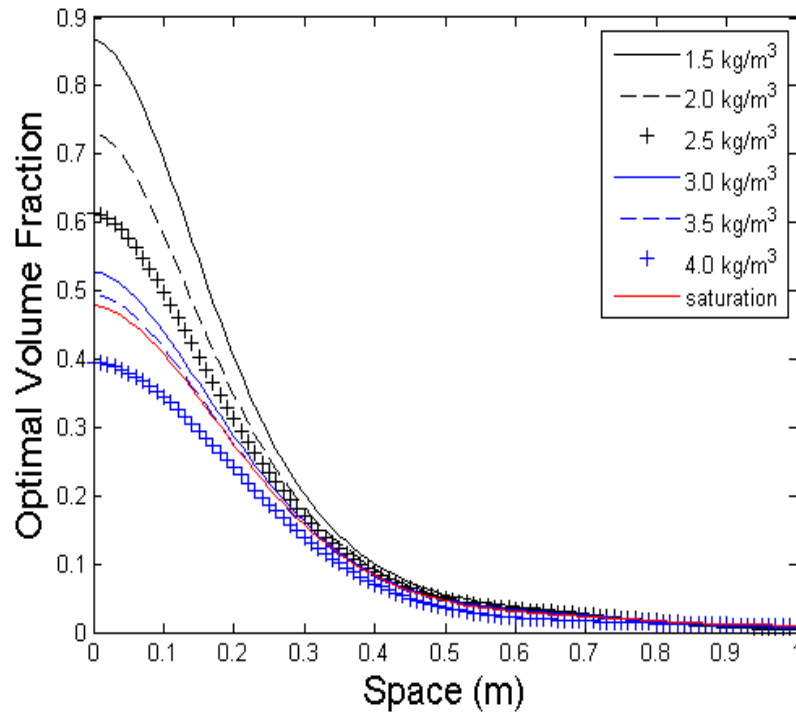


Figure 4.28: Effect of variable water vapor density due to gas pressure

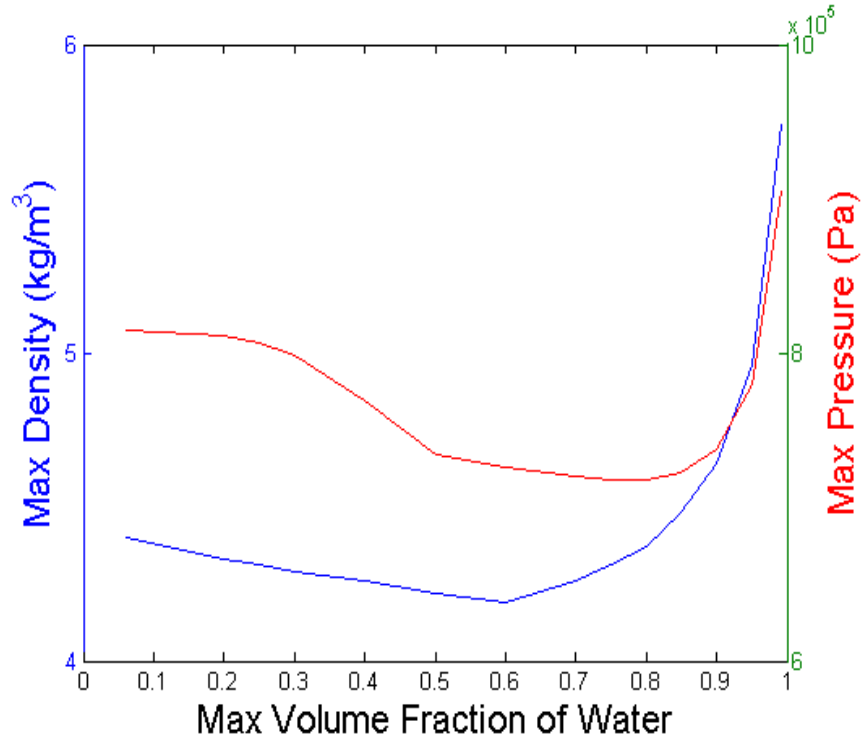


Figure 4.29: Effect of maximum of Gaussian water volume fraction distribution on IOP strength after 1 ms.

Figure 4.29 shows that for an initial water volume fraction distribution with a Gaussian shape, as the water volume fraction at the inlet approaches 1, the effect of plume confinement [29] takes over and can actually increase the jump in pressure at the shock front. The Gaussian distribution is such that the maximum exists at the inlet boundary and about 1% of the maximum half-way into the domain.

4.4 Serial and Parallel Code Run-Time Optimization

The last section of the results shows the run-time optimization performed within Matlab. For both the single-phase (3 adjoint) and the two-phase (7 adjoint) systems, 5 cases of increasing size were carried out with serial and parallel syntaxes. Jacket [99] was used to run the 3 adjoint calculation in parallel on Nvidia GPUs. Results for the time duration needed to solve the system in $[T^*, 0]$ are shown in Figure 4.30 and those of the 7 adjoint system are shown in Figure 4.31.

- Case 1: $m = 100$, timesteps = 1000 $\Rightarrow 10^5$ discrete points in space-time
Case 2: $m = 200$, timesteps = 2000 $\Rightarrow 4 \cdot 10^5$ discrete points in space-time
Case 3: $m = 300$, timesteps = 3000 $\Rightarrow 9 \cdot 10^5$ discrete points in space-time
Case 4: $m = 400$, timesteps = 4000 $\Rightarrow 1.6 \cdot 10^6$ discrete points in space-time
Case 5: $m = 500$, timesteps = 5000 $\Rightarrow 2.5 \cdot 10^6$ discrete points in space-time

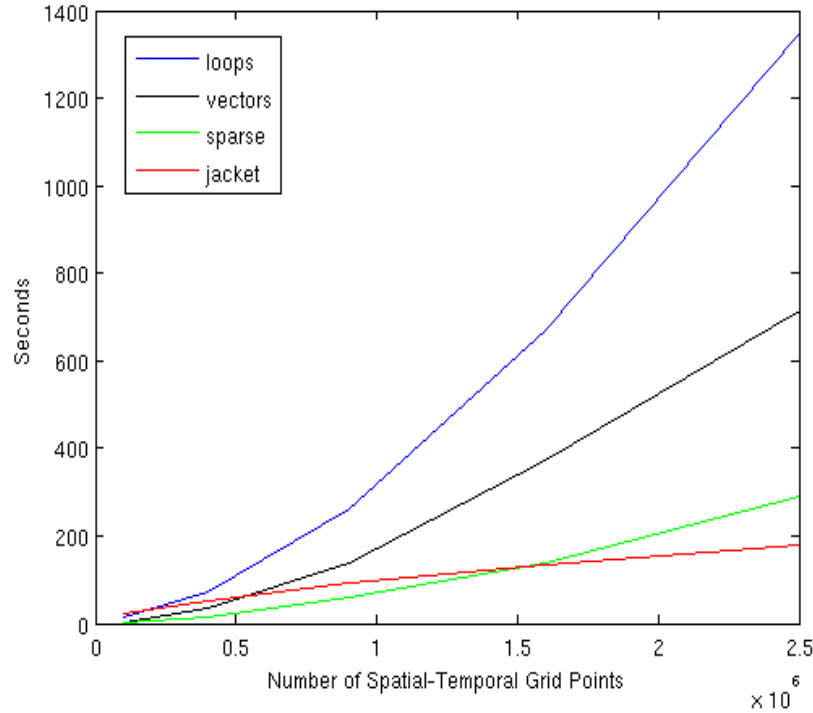


Figure 4.30: Time duration for solving the 3-component adjoint system of the Euler equations over the time interval $[T^*, 0]$

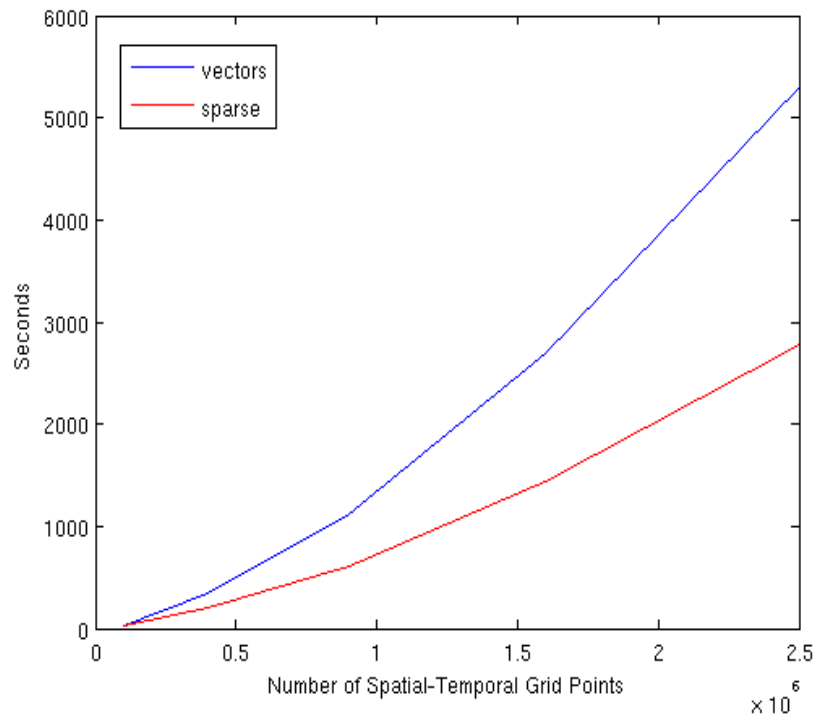


Figure 4.31: Time duration for solving 7-component adjoint system of two-phase model over the time interval $[T^*, 0]$

CHAPTER 5:

Conclusions

A new iterative solution procedure was developed, which can calculate optimal distributed control solutions for systems of quasi-linear hyperbolic partial differential equations with free initial and final data and final time. This procedure has been successfully applied to single- and two-phase compressible gas dynamics in one dimension with the goal of diminishing overpressure at the shock front of a blast wave generated by an ignition overpressure. Examples of optimal attenuation to blast waves typically encountered in the launch environment of the Shuttle's SRBs during an ignition are given. The single-phase control solutions can be seen as a spatial distribution of energy equivalent vaporized water mass required to achieve a given level of overpressure reduction. Results for these mass distributions are shown for inlet boundary conditions like those given in the monitor point data.

The same methodology for solving the control system is implemented on a two-phase model. The control action takes the form of the free initial data describing a distribution of water droplets. Optimal water volume fractions are calculated for increasing levels of attenuation. Cases where the maximum volume fraction of water is restricted to 50% and 70% are also presented.

The results give several key insights relevant to implementing water injection systems for blast wave attenuation. Smaller droplets will vaporize quicker since the total surface area exposed to the flow is larger [12], resulting in cooler gas driving a shock with an attenuated jump at the shock front. This would suggest that large regions of space completely filled with water are sub-optimal for blast attenuation since connected streams or ligaments of water expose less surface area to the gas.

The degree of attenuation depends largely on the rate of mass changing phase from liquid water to gaseous water vapor due to forced vaporization \dot{m} , which is equal to the product of the water vapor density and the rate of change of the volume occupied by the water droplets. In the high pressure and high temperature region behind the shock front, water vapor density is high and the rate of vaporization is high as well which both contribute to a large value for \dot{m} . As the control takes effect, the pressure and temperature of the gas both decrease meaning that the effects are

being felt by the shock front at a slower rate. These results show that, in general, stronger shocks can be attenuated more rapidly than weaker shocks via water droplet vaporization.

Similar to work that has identified plume confinement as being disadvantageous to blast attenuation [29], the results also show that when a shock propagates through a water volume fraction very close to 1 over a sufficient interval in space, so much liquid water is converted to gaseous water vapor that the increase in gas density becomes more significant to the pressure than the cooling of the gas due to vaporization. This shows that for a given interval of space there is a limit to the controllability. In a two meter domain, 76% OP_0 was the target with the lowest overpressure for which the solution still converged. The case with the volume fraction of water restricted to a maximum of $\alpha_l < 70\%$ converged with the lowest target overpressure of 80% OP_0 . With the water restricted to below $\alpha_l < 50\%$ by volume, the most attenuation achievable with a two meter domain is 82.5% OP_0 .

The code developed by the author is still in the prototype stage, however, the run-time optimization results show that certain parts of the code have been optimized within Matlab scripting. Implementation of the two-phase calculation on parallel GPUs using Jacket or through other GPU platforms would make the code a feasible tool to use in IOP and other two-phase unsteady shock wave attenuation calculations. The framework of the control formulation and method of solution will remain unchanged while allowing for added degrees of freedom like poly-dispersed droplets, droplet breakup, surface tension and multiple dimensions.

REFERENCES

- [1] E. J. Walsh, and P. M. Hart, "Flight-Measured Lift-off Ignition Overpressure, A Correlation with Sub-scale Model Tests," Martin Marietta Aerospace, AIAA-81-2458, Las Vegas, N.V., November 11-13, 1981.
- [2] D. Alvord, "Ares 1-X Ignition Overpressure T+30 Day Analysis and Results," Jacobs ESTS Group, ESTSG-FY10-00793, Kennedy Space Center, FL, January 2010.
- [3] S. Lai, and F. S. Laspesa, Ignition Overpressure Measured on STS Lift-Off and Correlation with Subscale Model Tests," *JANNAF, 13th Plume Technology Meeting*, 1982.
- [4] H. Hirahara, and M. Kawahashi, "Optical Measurement of Velocity and Drag Coefficient of Droplets Accelerated by Shock Waves," *Experiments in Fluids*, Vol. 38, 2005, pp. 258-268.
- [5] H. D. Willauer, R. Ananth, J. P. Farley, G. Back, M. Kennedy, J. O'Connor, and V. M. Gameiro, "Blast Mitigation Using Water Mist: Test Series II," NRL/MR/6180-09-9182, March 12, 2009.
- [6] G. O. Thomas, "On the Conditions Required for Explosion Mitigation by Water Sprays," *Transactions of the Institution of Chemical Engineers*, Vol. 78, Part B, September 2000, pp. 339-354.
- [7] D. Schwer, and K. Kailasanath, "Blast Mitigation by Water Mist (2), Shock Wave Mitigation using Glass Particles and Water Droplets," NRL Memorandum Report 6410-03-8658, January 21, 2003.
- [8] R. Ananth, H. D. Ladouceur, H. D. Willauer, J. P. Farley, and F. W. Williams, "Effect of Water Mist on a Confined Blast," *Suppression and Detection Research and Applications Technical Working Conference (SUPDET)*, Orlando, FL., March 11-13, 2008.
- [9] T. C. Hanson, D. F. Davidson, and R. K. Hanson, "Shock-Induced Behavior in Micron-Sized Water Aerosols," *Physics of Fluids*, Vol. 19, 2007, pp. 056104-1-056104-7.

- [10] F. Peters, and B. Paikert, "Measurement and Interpretation of Growth and Evaporation of Monodispersed Droplets in a Shock Tube," *International Journal of Heat and Mass Transfer*, Vol. 37, No. 2, May 1993, pp. 293-302.
- [11] H. W. Goosens, J. W. Cleijne, H. J. Smolders, and M. E. H. van Dongen, "Shock Wave Induced Evaporation of Water Droplets in a Gas-Droplet Mixture," *Experiments in Fluids*, Vol. 6, 1988, pp. 561-568.
- [12] G. Jourdan, L. Biamino, C. Mariani, C. Blanchot, E. Daniel, J. Massoni, L. Houas, R. Tosello, and D. Praguine, "Attenuation of a Shock Wave Passing Through a Cloud of Water Droplets" *Shock Waves*, Vol. 20, Number 4, 2010, pp. 285-296.
- [13] J. Monaghan, G. A. Hill, and W. G. Soucey, "Formulae for Mass Median and Mass Mean Drop Diameters," *DRES Suffield Memorandum*, PCN 13E10, September 1981.
- [14] W. H. Chou, L. P. Hsiang, and G. M. Faeth, "Temporal Properties of Drop Breakup in the Shear Regime," *International Journal of Multiphase Flow*, Vol. 23, No. 4, 1997, pp. 651-669.
- [15] L. P. Hsiang, and G. M. Faeth, "Drop Deformation and Breakup Due to Shock Wave and Steady Disturbances," *International Journal of Multiphase Flow*, Vol. 21, No. 4, 1995, pp. 545-560.
- [16] V. Semiao, P. Andrade, and M. da Graca Carvalho, "Spray Characterization: Numerical Prediction of Sauter Mean Diameter and Droplet Size Distribution," *Fuel*, Vol. 75, No. 15, 1996, pp. 1707-1714.
- [17] R. Tolman, "The Effect of Droplet Size on Surface Tension," *The Journal of Chemical Physics*, Vol. 17, No. 3, March 1949, pp. 333-337.
- [18] W. G. Reinecke, and G. D. Waldman, "A Study of Drop Breakup Behind Strong Shocks with Applications to Flight," *AVCO Report*, AD-871218, May 1970.
- [19] C. Crowe, M. Sommerfeld, and Y. Tsuji, "Multiphase Flows with Droplets and Particles," CRC Press, New York, 1998.
- [20] X. Rogue, G. Rodriguez, J. F. Haas, and R. Saurel, "Experimental and Numerical Investigation of the Shock-Induced Fluidization of Particle Beds," *Shock Waves*, Vol. 8, 1998, pp. 29-45.

- [21] J. Woo Jr., J. H. Jones, and S. H. Guest, "A Study of Effects of Water Addition on Supersonic Gas Streams," *JANNAF, 13th Plume Technology Meeting*, 1982.
- [22] H. Ikawa, and F. S. Laspesa, "Space Shuttle SRM Ignition Overpressure Prediction Methodology," *JANNAF, 13th Plume Technology Meeting*, 1982.
- [23] C. Kiris, W. Chan, D. Kwak, and J. A. Housman, "Time-Accurate Computational Analysis of the Flame Trench," *The Fifth International Conference on Computational Fluid Dynamics*, Seoul, Korea, July 7-11, 2008.
- [24] C. Kiris, J. Housman, D. Schauerhamer, M. Gusman, W. Chan, and D. Kwak, "Time-Accurate Computational Analysis of the Flame Trench Applications," 21st International Conference on Parallel Computational Fluid Dynamics, Moffett Field, CA, USA, May 18-22, 2009.
- [25] J. A. Housman, C. Kiris, and D. Kwak, "Time-Accurate Computational Analysis of a Dual-time Stepping Method for Simulating Ignition Overpressure Waves," *ICCFD6*, St. Petersburg, Russia, July 12-16, 2010.
- [26] C. Kiris, J. A. Housman, and D. Kwak, "Space-Time Convergence Analysis of a Ignition Overpressure in the Flame Trench," *CFD Review 2010*, World Scientific, 2010.
- [27] H. Ikawa, and F. S. Laspersa, "Analytical Understanding of WTR Ignition/Duct Overpressure Induced by Space Shuttle Solid Rocket Motor Ignition Transient," *AIAA/SAE/ASME 19th Joint Propulsion Conference*, Seattle, WA, June 27-29, 1983.
- [28] J. Troyes, I. Dubois, V. Borie, and A. Boischot, "Multi-phase Reactive Numerical Simulations of a Model Solid Rocket Motor Exhaust Jet," *42nd AIAA/ASME/SAI/ASEE Joint Propulsion Conference and Exhibit*, Sacramento, CA, July 9-12, 2006.
- [29] F. Canabal III, "Suppression of the Ignition Overpressure Generated by Launch Vehicles," Ph.D. Dissertation, Mechanical and Aerospace Engineering Department, University of Alabama, Huntsville, 2004.
- [30] F. Canabal III, and A. Frendi, "Study of the Ignition Overpressure Suppression Technique by Water Addition," *Journal of Spacecraft and Rockets*, Vol. 43, No. 4, 2006, pp. 853-865.

- [31] R. Saurel, and R. Abgrall, "A Multiphase Godunov Method for Compressible Multifluid and Multiphase Flows," *Journal of Computational Physics*, Vol. 150, 1999, pp. 425-467.
- [32] P. D. Lax, "Hyperbolic Systems of Conservation Laws and the Mathematical Theory of Shock Waves," Courant Institute of Mathematical Sciences, New York, 1972.
- [33] P. D. Lax, "Hyperbolic Partial Differential Equations," Courant Institute of Mathematical Sciences, New York, 2006.
- [34] G. B. Whitham, "Linear and Nonlinear Waves," Wiley, University of California, 1974.
- [35] A. J. Majda, "Compressible Fluid Flow and Systems of Conservation Laws in Several Space Variables," Springer, New York, 1984.
- [36] A. J. Chorin, and J. E. Marsden, "A Mathematical Introduction to Fluid Mechanics, 2nd Ed." Springer-Verlag, New York, 1984.
- [37] J. Glimm, "Solutions in the Large for Nonlinear Hyperbolic Systems of Equations," *Transactions on Pure and Applied Mathematics*, Vol. 18, 1965, pp. 697-715.
- [38] S. Bianchini, and A. Bressan, "Vanishing Viscosity Solutions of Nonlinear Hyperbolic Systems," *Annals of Mathematics*, Vol. 161, 2005, pp. 223-342.
- [39] C. L. Merkle, "Computational Fluid Dynamics of Inviscid and High Reynolds Number Flows," Unpublished Notes.
- [40] E. F. Toro, "Riemann Solvers and Numerical Methods for Fluid Dynamics, A Practical Introduction," Springer, New York, 2009.
- [41] R. Saurel, and R. Abgrall, "A Simple Method for Compressible Multi-fluid Flows," *SIAM Journal of Scientific Computing* Vol. 21, No. 3, 2000, pp. 1115-1145.
- [42] "IAPWS Industrial Formulation 1997 for the Thermodynamic Properties of Water and Steam (IAPWS-IF97)"
- [43] B. Texier, "Lecture 2: Symmetrizable Systems," RMMC Summer School, Laramie, WY, June 2010.
- [44] S. S. Sritharan, "Delta Wings with Shock-Free Cross Flow," *Quarterly of Applied Mathematics*, Vol. 43, No. 3, 1985, pp. 275-286.

- [45] M. D. Gunzburger, "Perspectives in Flow Control and Optimization," SIAM Books, Philadelphia, PA, 2003.
- [46] E. R. Pinch, "Optimal Control and the Calculus of Variations," Oxford University Press Inc., New York, 1993.
- [47] H. P. Geering, "Optimal Control with Engineering Applications," Springer, New York, 2007.
- [48] A. E. Bryson, and Y. C. Ho, "Applied Optimal Control, Optimization, Estimation and Control," Hemisphere Publishing Corporation, New York, 1975.
- [49] J. L. Lions, "Some Aspects of the Optimal Control of Distributed Parameter Systems," SIAM Books, Philadelphia, PA, 1972.
- [50] J. L. Lions, "Optimal Control of Systems Governed by Partial Differential Equations," Springer, New York, 1971.
- [51] D. G. Hull, "Optimal Control Theory for Applications," Springer, New York, 2003.
- [52] S. S. Sritharan, editor. "Optimal Control of Viscous Flow," SIAM Books, Philadelphia, PA, 1998.
- [53] S. Ulbrich, "A Sensitivity and Adjoint Calculus for Discontinuous Solutions of Hyperbolic Conservation Laws with Source Terms," *SIAM Journal of Control and Optimization*, Vol. 41, 2002, pp. 740-783.
- [54] S. Ulbrich, "Adjoint-Based Derivative Computations for the Optimal Control of Discontinuous Solution of Hyperbolic Conservation Laws," *Systems and Control Letters*, Vol. 3, pp. 309-323, 2003.
- [55] A. Bressan, and A. Marson, "A Variational Calculus for Discontinuous Solutions to Conservation Laws," *Communications on Partial Differential Equations*, Vol. 20, pp. 1491-1552, 1995.
- [56] A. Bressan, and A. Marson, "A Maximum Principle for Optimally Controlled Systems of Conservations Laws," *Rendiconti del Seminario Matematico della Universita di Padova*, tome 94, 1995, pp. 79-94.

- [57] NUMERICA: A Library of Source Codes for Teaching, Research and Applications, by E. F. Toro. Numeritek Limited, www.numeritek.com, UK, 1999.
- [58] S. K. Godunov, "A Finite Difference Method for the Numerical Computation of Discontinuous Solutions of the Equations of Fluid Dynamics," *Matematicheskii Sbornik*, Vol. 47, pp. 257-393, 1959.
- [59] P. L. Roe, "Approximate Riemann Solvers, Parameter Vectors, and Difference Schemes," *Journal of Computational Physics*, Vol. 135, 1981, pp. 250-258.
- [60] S. Gottlieb, and C. W. Shu, "Total Variation Diminishing Runge-Kutta Schemes," *Mathematics of Computation*, Vol. 67, No. 221, January 1998, pp. 73-85.
- [61] P. L. Roe, "Characteristic-Based Schemes for the Euler Equations," *Annual Review of Fluid Mechanics*, Vol. 18, 1986, pp. 337-365.
- [62] A. Harten, P. D. Lax, and B. Van Leer, "On Upstream Differencing and Godunov-Type Schemes for Hyperbolic Conservation Laws," *SIAM Review*, Vol, 25, No. 1, January 1983.
- [63] A. Jameson, W. Schmidt, E. Turkel, "Numerical Solution of the Euler Equations by Finite Volume Methods Using Runge-Kutta Time-Stepping Schmes," 14th AIAA Fluid and Plasma Dynamics Conference, Palo Alto, CA, June 23-25, 1981.
- [64] R. J. Leveque, "Numerical Methods for Conservation Laws," Birkhauser, Boston, 1990.
- [65] R. W. MacCormack, "A Numerical Method for Solving the Equations of Compressible Viscous Flow," 19th AIAA Aerospace Sciences Meeting, St. Louis, MO, Jan 12-15, 1981.
- [66] J. P. Cocchi, R. Saurel, and J. C. Loraud, "Some Remarks About the Resolution of High Velocity Flows Near Low Densities," *Shock Waves*, Vol. 8, pp. 119-125, 1998.
- [67] A. Kurganov, and E. Tadmor, "New High-Resolution Central Schemes for Nonlinear Conservation Laws and Convection-Diffusion Equations," *Journal of Computational Physics*, Vol. 160, 2000, pp. 241-282.
- [68] B. Van Leer, "Toward the Ultimate Conservative Difference Scheme (5) A Second-Order Sequel to Godunov's Method," *Journal of Computational Physics*, Vol. 32, July 1979, pp. 101-136.

- [69] S. F. Davis, "Simplified Second-Order Godunov-type Methods," *SIAM Journal of Scientific Statistical Computation*, Vol. 9, No. 3, May 1988, pp. 445-473.
- [70] S. Eidelman, P. Colella, and R. P. Shreeve, "Application of the Godunov Method and Its Second-Order Extension to Cascade Flow Modeling," *AIAA Journal*, Vol. 22, No. 11, 1984, pp. 1609-1615.
- [71] C. H. Chang, S. Sushchikh, L. Nguyen, M. S. Liou, and T. Theofanous, "Hyperbolicity, Discontinuities, and Numerics of the Two-Fluid Model," *5th Joint ASME/JSME Fluids Engineering Summer Conference, 10th International Symposium on Gas-Liquid Two-Phase Flows*, San Diego, CA, July 30-August 2, 2007.
- [72] R. Caiden, R. P. Fedkiw, and C. Anderson, "A Numerical Method for Two-Phase Flow Consisting of Separate Compressible and Incompressible Regions," *Journal of Computational Physics*, Vol. 166, 2001, pp. 1-27.
- [73] D. B. Kothe, and W. J. Rider, "Comments on Modeling Inter-facial Flows with Volume-of-Fluid Methods," Technical Report LA-UR-3384, Los Alamos National Laboratory, 1995.
- [74] C. A. Lowe, "Two-phase Shock-Tube Problems and Numerical Methods of Solution," *Journal of Computational Physics*, Vol. 204, 2005, pp. 598-632.
- [75] R. Abgrall, "How to Prevent Pressure Oscillations in Multicomponent Flow Calculations: A Quasi Conservative Approach," *Journal of Computational Physics*, Vol. 125, 1996, pp.150-160.
- [76] T. I. P. Shih, and W. J. Chyu, "Approximate Factorization with Source Terms," *AIAA Journal Technical Notes*, Vol. 29, No. 10, pp.1759-1760.
- [77] M. B. Giles, and N. A. Pierce, "Adjoint Equations in CFD; Duality, Boundary Conditions and Solution Behavior," AIAA-97-1850, A97-32424, pp. 182-198.
- [78] D. N. Srinath, and S. Mittla, "An Adjoint Method for Shape Optimization in Unsteady Viscous Flows," *Journal of Computational Physics*, Vol. 229, 2010, pp.1994-2008.
- [79] M. B. Giles, and N. A. Pierce, "On the Properties of Solutions of the Adjoint Euler Equations," *Numerical Methods for Fluid Dynamics, ICFD*, Vol. 6, 1998, pp. 116.

- [80] D. I. Papadimitriou, and K. C. Giannakaglou, "A Continuous Adjoint Method with Objective Function Derivatives Based on Boundary Integrals, for Inviscid and Viscous Flows," *Computers and Fluids*, Vol. 36, 2007, pp.325-341.
- [81] S. K. Nadarajah, and A. Jameson, "Optimum Shape Design for Unsteady Flows with Time-Accurate Continuous and Discrete Adjoint Methods," *AIAA Journal*, Vol. 45, No. 7, July 2007, pp. 1478-1490.
- [82] S. Nadarajah, and S. Jameson, "Optimal Control of Unsteady Flows using a Time Accurate Method," 9th *Symposium on Multidisciplinary Analysis Optimization Conference*, Atlanta, GA, September 4-6, 2002.
- [83] R. Giering, and T. Kaminski, "Recipes for Adjoint Code Construction," *ACM Transactions on Mathematical Software*, Vol. 24, No. 4, December 1998, pp. 437-474.
- [84] G. Biros, and O. Ghattas, "Parallel Lagrange-Newton-Krylov-Schur Methods for PDE-Constrained Optimization. Part 2: The Lagrange-Newton Solver and Its Applications to Optimal Control of Steady Viscous Flows," *SIAM Journal of Scientific Computing*, Vol. 27, No. 2, 2005, pp. 714-739.
- [85] E. E. Prudencio, R. Byrd, and X. C. Cai, "Parallel Full Space SQP Lagrange-Newton-Krylov-Schwarz Algorithms for PDE-Constrained Optimization Problems," *SIAM Journal of Scientific Computation* Vol. 27, No. 4, 2006, pp. 1305-1328.
- [86] C. Bushens, and H. Maurer, "SQP-Methods for Solving Optimal Control Problems with Control and State Constraints; Adjoint Variables, Sensitivity Analysis and Real-Time Control," *Journal of Computational and Applied Mathematics*, Vol. 120, 2000, pp. 85-108.
- [87] W. Alt, and K. Malanowski, "The Lagrange-Newton Method for Nonlinear Optimal Control Problems," *Computational Optimization and Applications*, Vol. 2, 1993, pp. 77-100.
- [88] M. Heinkenschloss, "Formulation and Analysis of a Sequential Quadratic Programming Method for the Optimal Dirichlet Boundary Control of Navier-Stokes Flow," *Optimal Control Theory; Algorithms and Applications*, TR97-14, October 7, 1997.
- [89] A. Barclay, P. E. Gill, and J. B. Rosen, "SQP Methods and Their Application to Numerical Optimal Control," Department of Mathematics, University of California, San Diego, La Jolla, CA, 1997.

- [90] J. V. Breakwell, "The Optimization of Trajectories," *SIAM Journal*, Vol. 7, No. 2, June 1959, pp. 215-247.
- [91] M. K. Banda, and M. Herty, "Adjoint IMEX-based Schemes for Control Problems Governed by Hyperbolic Conservation Laws," published online October 14, 2010; *Computational Optimization and Applications*, Springer, DOI: 10.1007/s10589-010-9362-2.
- [92] A. K. Alekseev, and I. M. Navon, "On Adjoint Variables for Discontinuous Flow," *Submitted for publication in Systems and Control Letters*, 2002.
- [93] M. B. Giles, "Non-Reflecting Boundary Conditions for Euler Equation Calculations," AIAA Paper 89-1942-CP 1989.
- [94] D. Givoli, "Non-Reflecting Boundary Conditions," *Journal of Computational Physics*, Vol. 94, 1991, pp.1-29.
- [95] G. Sutton, and O. Biblarz, "Solid Propellant Rocket Fundamentals, Rocket Propulsion Elements, 8th Ed.," John Wiley and Sons. Hoboken, New Jersey, 2010, pp. 437-438.
- [96] Cequel, Chemical Equilibrium in Excel, copyright 2003, Software and Engineering Associates, Inc.
- [97] CFD-FASTRAN User's Manual, version 2002, CFD Research Corporation, Huntsville, AL, 2002.
- [98] N. D. Moshman, "Optimal Control of the Unsteady Euler Equations in 1D with Application to Ignition Overpressure Attenuation in Launch Vehicles," 20th AIAA CFD Conference, Honolulu, HI, June 27-30, 2011.
- [99] Jacket - The GPU Acceleration Engine for Matlab, Acelereyes, www.accelereyes.com, 2011.

THIS PAGE INTENTIONALLY LEFT BLANK

APPENDIX A:

Calculation of the elements of $\frac{\partial A_{ij}}{\partial U_k} \frac{\partial U_k}{\partial x}$ for the two-phase adjoint system

Row 1:

$$\begin{aligned} \frac{\partial}{\partial u_k} A_{11} \cdot \frac{\partial u_k}{\partial x} &= \frac{\partial V_i}{\partial \alpha_g} \frac{\partial \alpha_g}{\partial x} + \frac{\partial V_i}{\partial \rho_g} \frac{\partial \rho_g}{\partial x} + \frac{\partial V_i}{\partial u_g} \frac{\partial u_g}{\partial x} + \frac{\partial V_i}{\partial \rho_l} \frac{\partial \rho_l}{\partial x} + \frac{\partial V_i}{\partial u_l} \frac{\partial u_l}{\partial x} \\ &\equiv \frac{dV_i}{dx} \end{aligned} \quad (\text{A.1})$$

Row 2:

$$\frac{\partial}{\partial u_k} A_{21} \cdot \frac{\partial u_k}{\partial x} = \frac{\rho_g}{\alpha_g} \left(\frac{dV_i}{dx} - \frac{\partial u_g}{\partial x} \right) + \frac{V_i - u_g}{\alpha_g} \left(\frac{\partial \rho_g}{\partial x} - \frac{\rho_g}{\alpha_g} \frac{\partial \alpha_g}{\partial x} \right) \quad (\text{A.2})$$

$$\frac{\partial}{\partial u_k} A_{22} \cdot \frac{\partial u_k}{\partial x} = \frac{\partial u_g}{\partial x} \quad (\text{A.3})$$

$$\frac{\partial}{\partial u_k} A_{23} \cdot \frac{\partial u_k}{\partial x} = \frac{\partial \rho_g}{\partial x} \quad (\text{A.4})$$

Row 3:

$$\frac{\partial}{\partial u_k} A_{31} \cdot \frac{\partial u_k}{\partial x} = \frac{-1}{\alpha_g \rho_g} \left[\frac{dP_i}{dx} - \frac{\partial P_g}{\partial x} + (P_g - P_i) \left(\frac{1}{\alpha_g} \frac{\partial \alpha_g}{\partial x} + \frac{1}{\rho_g} \frac{\partial \rho_g}{\partial x} \right) \right] \quad (\text{A.5})$$

$$\frac{\partial}{\partial u_k} A_{33} \cdot \frac{\partial u_k}{\partial x} = \frac{\partial u_g}{\partial x} \quad (\text{A.6})$$

$$\frac{\partial}{\partial u_k} A_{34} \cdot \frac{\partial u_k}{\partial x} = \frac{-1}{\rho_g^2} \frac{\partial \rho_g}{\partial x} \quad (\text{A.7})$$

Row 4:

$$\frac{\partial}{\partial u_k} A_{41} \cdot \frac{\partial u_k}{\partial x} = \frac{\rho_g c_{gi}^2}{\alpha_g} \left(\frac{dV_i}{dx} - \frac{\partial u_g}{\partial x} - \frac{V_i - u_g}{\alpha_g} \frac{\partial \alpha_g}{\partial x} \right) + \frac{V_i - u_g}{\alpha_g} \left((\gamma - 1) \frac{dP_i}{dx} + \frac{\partial P_g}{\partial x} \right) \quad (\text{A.8})$$

$$\frac{\partial}{\partial u_k} A_{43} \cdot \frac{\partial u_k}{\partial x} = \gamma \frac{\partial P_g}{\partial x} \quad (\text{A.9})$$

$$\frac{\partial}{\partial u_k} A_{44} \cdot \frac{\partial u_k}{\partial x} = \frac{\partial u_g}{\partial x} \quad (\text{A.10})$$

Row 5:

$$\frac{\partial}{\partial u_k} A_{51} \cdot \frac{\partial u_k}{\partial x} = \frac{\rho_l}{1 - \alpha_g} \left(\frac{dV_i}{dx} - \frac{\partial u_l}{\partial x} \right) + \frac{V_i - u_l}{1 - \alpha_g} \left(\frac{\partial \rho_l}{\partial x} + \frac{\rho_l}{1 - \alpha_g} \frac{\partial \alpha_g}{\partial x} \right) \quad (\text{A.11})$$

$$\frac{\partial}{\partial u_k} A_{55} \cdot \frac{\partial u_k}{\partial x} = \frac{\partial u_l}{\partial x} \quad (\text{A.12})$$

$$\frac{\partial}{\partial u_k} A_{56} \cdot \frac{\partial u_k}{\partial x} = \frac{\partial \rho_l}{\partial x} \quad (\text{A.13})$$

Row 6:

$$\frac{\partial}{\partial u_k} A_{61} \cdot \frac{\partial u_k}{\partial x} = \frac{-1}{(1 - \alpha_g) \rho_l} \left[\frac{dP_i}{dx} - \frac{\partial P_l}{\partial x} + (P_l - P_i) \left(\frac{-1}{1 - \alpha_g} \frac{\partial \alpha_g}{\partial x} + \frac{1}{\rho_l} \frac{\partial \rho_l}{\partial x} \right) \right] \quad (\text{A.14})$$

$$\frac{\partial}{\partial u_k} A_{66} \cdot \frac{\partial u_k}{\partial x} = \frac{\partial u_l}{\partial x} \quad (\text{A.15})$$

$$\frac{\partial}{\partial u_k} A_{67} \cdot \frac{\partial u_k}{\partial x} = \frac{-1}{\rho_l^2} \frac{\partial \rho_l}{\partial x} \quad (\text{A.16})$$

Row 7:

$$\frac{\partial}{\partial u_k} A_{71} \cdot \frac{\partial u_k}{\partial x} = \frac{\rho_l c_{li}^2}{1 - \alpha_g} \left(\frac{DV_i}{Dx} - \frac{\partial u_l}{\partial x} + \frac{V_i - u_l}{1 - \alpha_g} \frac{\partial \alpha_g}{\partial x} \right) + \frac{V_i - u_l}{1 - \alpha_g} \left((\gamma_l - 1) \frac{DP_i}{Dx} + \frac{\partial P_l}{\partial x} \right) \quad (\text{A.17})$$

$$\frac{\partial}{\partial u_k} A_{76} \cdot \frac{\partial u_k}{\partial x} = \gamma_l \frac{\partial P_l}{\partial x} \quad (\text{A.18})$$

$$\frac{\partial}{\partial u_k} A_{77} \cdot \frac{\partial u_k}{\partial x} = \frac{\partial u_l}{\partial x} \quad (\text{A.19})$$

THIS PAGE INTENTIONALLY LEFT BLANK

APPENDIX B:

Calculation of the elements of $\frac{\partial S_i}{\partial U_j}$ for the two-phase adjoint system

Solution of the adjoint system of PDEs requires deriving the matrix $\frac{\partial S}{\partial U}$ where $S(U)$ is the source vector for interactions between the two phases.

$$S(U) = \begin{pmatrix} \mu(P_g - P_l) + \Delta\alpha_{gvap} \\ \dot{m} \\ \dot{m}V_i + F_d \\ \dot{m}(L_{hv} + E_i) + Q_i + F_dV_i - \mu P_i(P_g - P_i) \\ -\dot{m} \\ -\dot{m}V_i - F_d \\ -\dot{m}(L_{hv} + E_i) - Q_i - F_dV_i + \mu P_i(P_g - P_i) \end{pmatrix} \quad (\text{B.1})$$

Before calculating derivatives with respect to state variables, it must be made clear which terms are explicit functions of which variables. $\Delta\alpha_{gvap}(U)$, $\dot{m}(U)$, $F_d(U)$, $Q_i(U)$, $V_i(U)$, $P_i(U)$, and $E_i(U)$ yet only E_i is an explicit function of all seven state variables. Therefore, it is worth determining only the derivatives that exist ahead of time to more precisely define the elements of $\frac{\partial S}{\partial U}$.

The easiest term to differentiate is the interface pressure.

$$P_i = \alpha_g P_g + (1 - \alpha_g) P_l \quad (\text{B.2})$$

Therefore, $P_i = P_i(\alpha_g, P_g, P_l)$ and the derivatives are:

$$\frac{\partial P_i}{\partial \alpha_g} = P_g - P_l \quad (\text{B.3})$$

$$\frac{\partial P_i}{\partial P_g} = \alpha_g \quad (\text{B.4})$$

$$\frac{\partial P_i}{\partial P_l} = 1 - \alpha_g \quad (\text{B.5})$$

The interface velocity is a function of a subset of state variables as well: $V_i = V_i(\alpha_g, \rho_g, u_g, \rho_l, u_l)$

The derivatives are:

$$\frac{\partial V_i}{\partial \alpha_g} = \frac{\rho_g u_g - \rho_l u_l}{\alpha_g \rho_g + (1 - \alpha_g) \rho_l} - \frac{\alpha_g \rho_g u_g + (1 - \alpha_g) \rho_l u_l}{(\alpha_g \rho_g + (1 - \alpha_g) \rho_l)^2} \cdot (\rho_g - \rho_l) \quad (\text{B.6})$$

$$\frac{\partial V_i}{\partial \rho_g} = \frac{\alpha_g u_g}{\alpha_g \rho_g + (1 - \alpha_g) \rho_l} - \frac{\alpha_g \rho_g u_g + (1 - \alpha_g) \rho_l u_l}{(\alpha_g \rho_g + (1 - \alpha_g) \rho_l)^2} \cdot \alpha_g \quad (\text{B.7})$$

$$\frac{\partial V_i}{\partial \rho_l} = \frac{(1 - \alpha_g) u_l}{\alpha_g \rho_g + (1 - \alpha_g) \rho_l} - \frac{\alpha_g \rho_g u_g + (1 - \alpha_g) \rho_l u_l}{(\alpha_g \rho_g + (1 - \alpha_g) \rho_l)^2} \cdot (1 - \alpha_g) \quad (\text{B.8})$$

$$\frac{\partial V_i}{\partial u_g} = \frac{\alpha_g \rho_g}{\alpha_g \rho_g + (1 - \alpha_g) \rho_l} \quad (\text{B.9})$$

$$\frac{\partial V_i}{\partial u_l} = \frac{(1 - \alpha_g) \rho_g}{\alpha_g \rho_g + (1 - \alpha_g) \rho_l} \quad (\text{B.10})$$

The drag force $F_d(U) = F_d(\alpha_g, \rho_g, u_g, u_l)$

$$\frac{\partial F_d}{\partial \alpha_g} = -\frac{3}{4} C_d \rho_g D_p^2 (u_g - u_l)^2 \quad (\text{B.11})$$

$$\frac{\partial F_d}{\partial \rho_g} = \frac{3}{4} C_d D_p^2 (1 - \alpha_g) (u_g - u_l)^2 \quad (\text{B.12})$$

$$\frac{\partial F_d}{\partial u_g} = \frac{3}{2} C_d \rho_g D_p^2 (1 - \alpha_g) (u_g - u_l) \quad (\text{B.13})$$

$$\frac{\partial F_d}{\partial u_l} = -\frac{3}{2}C_d\rho_g D_p^2 (1 - \alpha_g) (u_g - u_l) \quad (\text{B.14})$$

The derivatives of \dot{m} and $\Delta\alpha_{gvap}$ are closely related. Recall,

$$\dot{m}(U) = \Delta\alpha_{gvap}(U) \cdot \rho_{H_2O_v}(P_g) \quad (\text{B.15})$$

where $\rho_{H_2O_v}$ is the density of water vapor and is only a function of gas pressure. It's derivative is easily calculated from the quadratic fit to the empirical steam table data given in Equation 2.38.

$$\frac{d\rho_{H_2O_v}}{dP_g/atm} \approx \left(.5368 - .0048688 \cdot \frac{P_g}{atm} \right) kg/m^3 \quad (\text{B.16})$$

It suffices to calculate derivatives of $\Delta\alpha_{gvap}$ with respect to the state variables. The vaporization model is based on the Empirical-Beta Vaporization Law which states:

$$\left(D_p^{n+1}\right)^2 = \left(D_p^n\right)^2 - \Delta t \beta \left(T_g^n\right) \quad (\text{B.17})$$

and

$$\Delta\alpha_{gvap} = \frac{N_p\pi}{6\Delta x^3} \left(\left(D_p^n\right)^3 - \left(\left(D_p^n\right)^2 - \Delta t \beta (\rho_g, P_g) \right)^{3/2} \right) \quad (\text{B.18})$$

$T_g = \frac{P_g}{\rho_g R}$ where R is the specific gas constant for air, so $\Delta\alpha_{gvap}(U) = \Delta\alpha_{gvap}(\rho_g, P_g)$. The derivatives are:

$$\frac{\partial \Delta\alpha_{gvap}}{\partial \rho_g} = \frac{N_p\pi}{6\Delta x^3} \left(\frac{3}{2} \right) \left(\left(D_p^n\right)^2 - \Delta t \beta \right)^{1/2} (\Delta t) \frac{\partial \beta}{\partial \rho_g} \quad (\text{B.19})$$

and similarly,

$$\frac{\partial \Delta \alpha_{gvap}}{\partial P_g} = \frac{N_p \pi}{6 \Delta x^3} \left(\frac{3}{2} \right) \left((D_p^n)^2 - \Delta t \beta \right)^{1/2} (\Delta t) \frac{\partial \beta}{\partial P_g} \quad (\text{B.20})$$

The vaporization term is given by Equation B.21:

$$\beta(\rho_g, P_g) = B_0 \left(1 + B_1 \left(\frac{P_g}{\rho_g R} - T_{min} \right)_+^{B_2} \right) \mu m^2/s \quad (\text{B.21})$$

where the constants are given as $B_0 = 7600$, $B_1 = 7.4 \cdot 10^{-7}$, $B_2 = 2.7548$ and $T_{min} = 300$ degrees Kelvin. Therefore, the derivatives are:

$$\frac{\partial \beta}{\partial \rho_g} = -B_0 B_1 B_2 (T_g - T_{min})_+^{B_2-1} \left(\frac{T_g}{\rho_g} \right) \quad (\text{B.22})$$

$$\frac{\partial \beta}{\partial P_g} = B_0 B_1 B_2 (T_g - T_{min})_+^{B_2-1} \left(\frac{T_g}{P_g} \right) \quad (\text{B.23})$$

The total energy at the interface is simply defined in the conservative basis:

$$E_i = \alpha_g E_g + (1 - \alpha_g) E_l \quad (\text{B.24})$$

But not so easily in the primitive basis. Using the equations of state:

$$E_i = \alpha_g \left(\frac{P_g}{\rho_g (\gamma_g - 1)} - .5 u_g^2 \right) + (1 - \alpha_g) \left(\frac{P_l + \gamma_l \pi_l}{\rho_l (\gamma_l - 1)} - .5 u_l^2 \right) \quad (\text{B.25})$$

In this basis, the interface velocity is a function of all primitive variables and therefore there are seven non-zero derivatives to calculate:

$$\frac{\partial E_i}{\partial \alpha_g} = E_g - E_l \quad (\text{B.26})$$

$$\frac{\partial E_i}{\partial \rho_g} = \frac{-\alpha_g P_g}{\rho_g^2 (\gamma_g - 1)} \quad (\text{B.27})$$

$$\frac{\partial E_i}{\partial \rho_l} = \frac{-(1 - \alpha_g) (P_l - \gamma_l \pi_l)}{\rho_l^2 (\gamma_l - 1)} \quad (\text{B.28})$$

$$\frac{\partial E_i}{\partial u_g} = \alpha_g u_g \quad (\text{B.29})$$

$$\frac{\partial E_i}{\partial u_l} = (1 - \alpha_g) u_l \quad (\text{B.30})$$

$$\frac{\partial E_i}{\partial P_g} = \frac{\alpha_g}{\rho_g (\gamma_g - 1)} \quad (\text{B.31})$$

$$\frac{\partial E_i}{\partial P_l} = \frac{1 - \alpha_g}{\rho_l (\gamma_l - 1)} \quad (\text{B.32})$$

Lastly, the derivatives of the rate of convective heat transfer between the two phases at the interphase $Q_i (U)$ are calculated.

$$\begin{aligned} Q_i (U) &= h \cdot S_p \cdot (T_g - T_l) \\ &= \frac{Nu \cdot \lambda}{D_p} S_p \cdot (T_g - T_l) \\ &= \left(2 + .459 Pr^{1/3} Re^{.55} \right) \frac{\lambda}{D_p} \cdot 4\pi \left(\frac{D_p}{2} \right)^2 \cdot \left(\frac{P_g}{\rho_g R} - \frac{1}{C_{vl}} \left(\frac{P_l + \gamma_l \pi_l}{\rho_l (\gamma_l - 1)} - e_l 0 \right) \right) \\ &= \left(2 + .459 \left(\frac{C_p \mu}{\lambda} \right)^{1/3} \left(\frac{D_p \rho_g (u_g - u_l)}{\mu} \right)^{.55} \right) \lambda \pi D_p \left(\frac{P_g}{\rho_g R} - \frac{1}{C_{vl}} \left(\frac{P_l + \gamma_l \pi_l}{\rho_l (\gamma_l - 1)} - e_l 0 \right) \right) \end{aligned} \quad (\text{B.33})$$

Therefore $Q_i = Q_i (\rho_g, u_g, P_g, \rho_l, P_l)$ and the derivatives are:

$$\frac{\partial Q_i}{\partial \rho_g} = \lambda \pi D_p \left(\frac{dNu}{d\rho_g} (T_g - T_l) - Nu \frac{T_g}{\rho_g} \right) \quad (\text{B.34})$$

$$\frac{\partial Q_i}{\partial u_g} = \lambda \pi D_p \frac{dNu}{du_g} (T_g - T_l) \quad (\text{B.35})$$

$$\frac{\partial Q_i}{\partial P_g} = \lambda \pi D_p Nu \frac{T_g}{P_g} \quad (\text{B.36})$$

$$\frac{\partial Q_i}{\partial \rho_l} = \lambda \pi D_p Nu \frac{T_l}{\rho_l} \quad (\text{B.37})$$

$$\frac{\partial Q_i}{\partial u_l} = \lambda \pi D_p \frac{dNu}{du_l} (T_g - T_l) \quad (\text{B.38})$$

$$\frac{\partial Q_i}{\partial P_l} = \lambda \pi D_p Nu \frac{T_l}{P_l - \gamma_l \pi_l} \quad (\text{B.39})$$

And it can easily be seen that the derivatives of the Nusslets' Number are:

$$\frac{\partial Nu}{\partial \rho_g} = .458 \cdot .55 \cdot Pr^{1/3} Re^{.55-1} \frac{D_p (u_g - u_l)}{\mu} \quad (\text{B.40})$$

$$\frac{\partial Nu}{\partial u_g} = .458 \cdot .55 \cdot Pr^{1/3} Re^{.55-1} \frac{D_p \rho_g}{\mu} \quad (\text{B.41})$$

$$\frac{\partial Nu}{\partial u_l} = -.458 \cdot .55 \cdot Pr^{1/3} Re^{.55-1} \frac{D_p \rho_g}{\mu} \quad (\text{B.42})$$

Now, with all of the derivatives of each individual function of the state vector that compose the source vector, the on-zero elements of the matrix $\frac{\partial S}{\partial U}$ can be calculated.

Row 1:

$$\frac{\partial S_1}{\partial \rho_g} = \frac{N_p \pi}{6 \Delta x^3} \left(\frac{-3}{2} \right) \left((D_p^n)^2 - \Delta t \beta^n \right)^{1/2} \frac{\partial \beta^n}{\partial \rho_g} \quad (\text{B.43})$$

$$\frac{\partial S_1}{\partial P_g} = \mu + \frac{N_p \pi}{6 \Delta x^3} \left(\frac{-3}{2} \right) \left((D_p^n)^2 - \Delta t \beta^n \right)^{1/2} \frac{\partial \beta^n}{\partial P_g} \quad (\text{B.44})$$

$$\frac{\partial S_1}{\partial P_l} = -\mu \quad (\text{B.45})$$

Row 2:

$$\frac{\partial S_2}{\partial \rho_g} = \frac{\partial \dot{m}}{\partial \rho_g} \quad (\text{B.46})$$

$$\frac{\partial S_2}{\partial P_g} = \frac{\partial \dot{m}}{\partial P_g} \quad (\text{B.47})$$

Row 3:

$$\frac{\partial S_3}{\partial \alpha_g} = \dot{m} \frac{\partial V_i}{\partial \alpha_g} + \frac{\partial F_d}{\partial \alpha_g} \quad (\text{B.48})$$

$$\frac{\partial S_3}{\partial \rho_g} = \frac{\partial \dot{m}}{\partial \rho_g} V_i + \dot{m} \frac{\partial V_i}{\partial \rho_g} + \frac{\partial F_d}{\partial \rho_g} \quad (\text{B.49})$$

$$\frac{\partial S_3}{\partial \rho_l} = \dot{m} \frac{\partial V_i}{\partial \rho_l} \quad (\text{B.50})$$

$$\frac{\partial S_3}{\partial u_g} = \dot{m} \frac{\partial V_i}{\partial u_g} + \frac{\partial F_d}{\partial u_g} \quad (\text{B.51})$$

$$\frac{\partial S_3}{\partial u_l} = \dot{m} \frac{\partial V_i}{\partial u_l} + \frac{\partial F_d}{\partial u_l} \quad (\text{B.52})$$

$$\frac{\partial S_3}{\partial P_g} = \frac{\partial \dot{m}}{\partial P_g} V_i \quad (\text{B.53})$$

Row 4:

$$\frac{\partial S_4}{\partial \alpha_g} = \dot{m} \frac{\partial E_i}{\partial \alpha_g} + \frac{\partial F_d}{\partial \alpha_g} V_i + F_d \frac{\partial V_i}{\partial \alpha_g} - \mu (P_g - P_l)^2 \quad (\text{B.54})$$

$$\frac{\partial S_4}{\partial \rho_g} = \frac{\partial \dot{m}}{\partial \rho_g} (L_{hv} + E_i) + \dot{m} \frac{\partial E_i}{\partial \rho_g} + \frac{\partial Q_i}{\partial \rho_g} + \frac{\partial F_d}{\partial \rho_g} V_i + F_d \frac{\partial V_i}{\partial \rho_g} \quad (\text{B.55})$$

$$\frac{\partial S_4}{\partial u_g} = \dot{m} \frac{\partial E_i}{\partial u_g} + \frac{\partial Q_i}{\partial u_g} + \frac{\partial F_d}{\partial u_g} V_i + F_d \frac{\partial V_i}{\partial u_g} \quad (\text{B.56})$$

$$\frac{\partial S_4}{\partial P_g} = \frac{\partial \dot{m}}{\partial P_g} (L_{hv} + E_i) + \dot{m} \frac{\partial E_i}{\partial P_g} + \frac{\partial Q_i}{\partial P_g} - \mu (\alpha_g (P_g - P_l) + P_i) \quad (\text{B.57})$$

$$\frac{\partial S_4}{\partial \rho_l} = \dot{m} \frac{\partial E_i}{\partial \rho_l} + \frac{\partial Q_i}{\partial \rho_l} + F_d \frac{\partial V_i}{\partial \rho_l} \quad (\text{B.58})$$

$$\frac{\partial S_4}{\partial u_l} = \dot{m} \frac{\partial E_i}{\partial u_l} + V_i \frac{\partial F_d}{\partial u_l} + F_d \frac{\partial V_i}{\partial u_l} + \frac{\partial Q_i}{\partial u_l} \quad (\text{B.59})$$

$$\frac{\partial S_4}{\partial P_l} = \dot{m} \frac{\partial E_i}{\partial P_l} + \frac{\partial Q_i}{\partial P_l} - \mu ((1 - \alpha_g) (P_g - P_l) - P_i) \quad (\text{B.60})$$

Rows 5, 6 and 7 are the opposite sign of rows 2, 3 and 4 respectively.

APPENDIX C:

Time Derivatives and Discretization of Transversality Condition for Single- and Two-Phase Control Formulation

For the single-phase problem, the continuous form of the functional f that must equal zero at the optimal final time is given in Equation 2.98. For convenience, the following definition is constructed, suppressing the subscript $_g$ for the gas phase.

$$\frac{dP}{dt} \equiv \left(\begin{array}{c} \frac{\partial P}{\partial \rho} \frac{\partial \rho}{\partial t} + \\ \frac{\partial P}{\partial \rho u} \frac{\partial \rho u}{\partial t} + \\ \frac{\partial P}{\partial \rho E} \frac{\partial \rho E}{\partial t} + \\ \frac{\partial P}{\partial t} \end{array} \right) = (\gamma - 1) \left(\frac{u^2}{2} \frac{\partial \rho}{\partial t} - u_g \frac{\partial \rho u}{\partial t} + \frac{\partial \rho E}{\partial t} \right) + \frac{\partial P}{\partial t} \quad (\text{C.1})$$

The discrete form is shown in Equation C.2.

$$\frac{dP}{dt}_i = (\gamma - 1) \left(\begin{array}{c} \frac{u(x_i, t^N)^2}{2} \frac{\rho(x_i, t^N) - \rho(x_i, t^{N-1})}{\Delta t} - \\ u(x_i, t^N) \frac{\rho u(x_i, t^N) - \rho u(x_i, t^{N-1})}{\Delta t} + \\ \frac{\rho E(x_i, t^N) - \rho E(x_i, t^{N-1})}{\Delta t} \end{array} \right) + \frac{P(x_i, t^N) - P(x_i, t^{N-1})}{\Delta t} \quad (\text{C.2})$$

$$\frac{df}{dt} = \int_{\Omega} \left(a z \frac{\partial z}{\partial t} + b \frac{\partial P}{\partial t} \cdot \frac{dP}{dt} + b(P - Q) \cdot \frac{d^2 P}{dt^2} \right) dx \quad (\text{C.3})$$

The continuous derivative of the term $\frac{d^2 P}{dt^2}$ is given in Equation C.4 and the discrete form in Equation C.5.

$$\frac{d^2 P}{dt^2} = (\gamma - 1) \left(u \frac{\partial u}{\partial t} \frac{\partial \rho}{\partial t} + \frac{u^2}{2} \frac{\partial^2 \rho}{\partial t^2} + \frac{\partial u}{\partial t} \frac{\partial \rho u}{\partial t} + u \frac{\partial^2 \rho u}{\partial t^2} + \frac{\partial^2 \rho E}{\partial t^2} \right) + \frac{\partial^2 P}{\partial t^2} \quad (\text{C.4})$$

$$\frac{d^2 P}{dt^2}_i = (\gamma - 1) \left(\begin{aligned} & u(x_i, t^N) \frac{u(x_i, t^N) - u(x_i, t^{N-1})}{\Delta t} \frac{\rho(x_i, t^N) - \rho(x_i, t^{N-1})}{\Delta t} + \\ & \frac{u^2(x_i, t^N)}{2} \frac{\rho(x_i, t^N) - 2\rho(x_i, t^{N-1}) + \rho(x_i, t^{N-2})}{\Delta t^2} + \\ & \frac{u(x_i, t^N) - u(x_i, t^{N-1})}{\Delta t} \frac{\rho u(x_i, t^N) - \rho u(x_i, t^{N-1})}{\Delta t} + \\ & u(x_i, t^N) \frac{\rho u(x_i, t^N) - 2\rho u(x_i, t^{N-1}) + \rho u(x_i, t^{N-2})}{\Delta t^2} + \\ & \frac{\rho E(x_i, t^N) - 2\rho E(x_i, t^{N-1}) + \rho E(x_i, t^{N-2})}{\Delta t^2} + \\ & \frac{1}{\gamma - 1} \frac{P(x_i, t^N) - 2P(x_i, t^{N-1}) + P(x_i, t^{N-2})}{\Delta t^2} \end{aligned} \right) \quad (\text{C.5})$$

$$\frac{df}{dt} \approx \sum_{i=1}^M \left(\begin{aligned} & a z(x_i, t^N) \frac{z(x_i, t^N) - z(x_i, t^{N-1})}{\Delta t} + b \frac{P(x_i, t^N) - P(x_i, t^{N-1})}{\Delta t} \cdot DP_i + \\ & b \left(P(x_i, t^N) - Q(x_i, t^N) \right) \cdot \frac{d}{dt} DP_i \end{aligned} \right) \Delta x \quad (\text{C.6})$$

For the two-phase problem, the derivative of the continuous form of the Transversality Condition is calculated from Equation 2.115 and shown here in Equation C.7 and it's discrete summation form in Equation C.8.

$$\frac{df}{dt} = \int_{\Omega} \left(\frac{\partial P}{\partial t} \right)^2 + (P - Q) \frac{\partial^2 P}{\partial t^2} dx \quad (\text{C.7})$$

$$\frac{df}{dt} \approx \sum_{i=1}^M \left(\left(\frac{P(x_i, t^N) - P(x_i, t^{N-1})}{\Delta t} \right)^2 + \left(P(x_i, t^N) - Q(x_i) \right) \frac{P(x_i, t^N) - 2P(x_i, t^{N-1}) + P(x_i, t^{N-2})}{\Delta t^2} \right) \Delta x \quad (\text{C.8})$$

THIS PAGE INTENTIONALLY LEFT BLANK

Initial Distribution List

1. Defense Technical Information Center
Ft. Belvoir, Virginia
2. Dudley Knox Library
Naval Postgraduate School
Monterey, California
3. Marine Corps Representative
Naval Postgraduate School
Monterey, California
4. Directory, Training and Education, MCCDC, Code C46
Quantico, Virginia
5. Marine Corps Tactical System Support Activity (Attn: Operations Officer)
Camp Pendleton, California
Officer students in the Operations Research Program are also required to show:
6. Director, Studies and Analysis Division, MCCDC, Code C45
Quantico, Virginia
Officer students in the Space Ops/Space Engineering Program or in the Information Warfare/Information Systems and Operations are also required to show:
7. Head, Information Operations and Space Integration Branch,
PLI/PP&O/HQMC, Washington, DC